UNIVERSITY OF CALIFORNIA, SAN DIEGO

Experimental Studies of Relaxation of Two-Dimensional Turbulence in Magnetized Electron Plasma Columns

A dissertation submitted in partial satisfaction of the

requirements for the degree Doctor of Philosophy

in Physics

by

Xiao-Pei Huang

Committee in charge:

Dr. Charles F. Driscoll, Chairman
Professor Patrick H. Diamond
Professor Morteza Gharib (Cal. Inst. of Tech.)
Professor Thomas M. O'Neil
Professor Clifford M. Surko
Professor Charles W. Van Atta

1993

The dissertation of Xiao-Pei Huang is approved, and it is acceptable in quality and form for publication on microfilm:

Chairman

University of California, San Diego

1993

This dissertation is dedicated to my parents

for encouraging me to pursue higher goals in life.

Contents

List of Figures

List of Tables

Acknowledgements

I am very grateful to have the opportunity to do graduate research under the supervision of Dr. Fred Driscoll and late Dr. John Malmberg. Through numerous examples, Dr. Driscoll showed me how to be a first-rate experimental physicist. Among many of his distinguished qualities, the vision and leadership of Dr. Malmberg had the most profound influence on me. I also had the good fortune to be a student of Dr. Tom O'Neil whose elegant and concise style is the standard I will try to meet. In addition, I would like to thank other members of my doctoral committee for taking time to read my thesis and giving me many valuable suggestions.

It has been such a pleasure interacting with my coworkers at UCSD non-neutral plasma group. Dr. Kevin Fine built a plasma imaging diagnostic that turned out to be very helpful; some theoretical models used in this thesis were calculated by Dr. Ralph Smith; and Dr. Dan Dubin has given me many good advices.

I am deeply indebted to those from whom I have received much help and learned a great deal, especially Drs. Fransçois Anderegg, Bret Beck, Dennis Eggleston, Joel Fajans, Al Hyatt, John Moody, and Eli Sarid; special thanks also go to Dirk Hartmann, Dr. Travis Mitchell, and my fellow graduate students, Ann Cass, Shi-Jie Chen, Brian Cluggish, Steve Crooks, Tom Dyer, Andrei Gruzinov, Marshall Loewenstein, Peter Rooney, Gene Sandler, and Mark Tinkle. Bob Bongard and Jo Ann Christina provided professional helps for this work.

I would like to thank Mr. & Mrs. Lauren & Joan Stayton for their hospitality

and encouragement. I have also enjoyed the friendship of Nan Chen, Peipei Ping and many others. Finally, I want to thank my family for having high expectations for me and providing strong support through the years, and of course, I would not have been able to finish this dissertation without the love and companionship of my dear wife Q. J.

This work was supported financially by Department of Energy grant DE-FG03-85ER53199, National Science Foundation grant PHY91-20240, and Office of Naval Research grant N00014-89-J-1714.

Vita, Publications and Fields of Study

Vita

26 March 1963	Born, Beijing, China
1985	B.S., Beijing University
1985–1986	Teaching Assistant, Department of Physics, University of California, San Diego
1986–1993	Research Assistant, Department of Physics, University of California, San Diego
1987	M.S., University of California, San Diego
1993	Ph.D., University of California, San Diego

Publications

1. X.-P. Huang, C. F. Driscoll, and J. H. Malmberg, "Dynamical and Statistical Measurements on Plasmas Exhibiting Vortex Growth and Decay," Plasma Div., APS, Hollywood, *Bull. Am. Phys. Soc.* **33**, 1898, (1988).

2. J. H. Malmberg, C. F. Driscoll, B. R. Beck, D. L. Eggleston, J. Fajans, K. S. Fine, X.-P. Huang, and A. W. Hyatt, "Experiments with Pure Electron Plasmas," in *Non-Neutral Plasma Physics* (C. W. Roberson and C. F. Driscoll, editors), AIP Conf. Proc. **175**, 34, (AIP, Washington D.C., 1988).

3. X.-P. Huang, C. F. Driscoll, and J. H. Malmberg, "Dynamical and Statistical Measurements on Vortex-Driven Turbulence," Plasma Div., APS, Anaheim, *Bull. Am. Phys. Soc.* **34**, 1931, (1989).

4. C. F. Driscoll, J. H. Malmberg, K. S. Fine, R. A. Smith, X.-P. Huang, and R. W. Gould, "Growth and Decay of Turbulent Vortex Structures in Pure Electron Plasmas," in *Plasma Physics and Controlled Nuclear Fusion Research 1988*, **3**, 507, (IAEA, Vienna, 1989).

5. X.-P. Huang, C. F. Driscoll, and J. H. Malmberg, "Measurements of the Decay of Two-Dimensional Turbulence in Pure Electron Plasmas," Plasma Div., APS, Cincinnati, *Bull. Am. Phys. Soc.* **35**, 2135, (1990).

6. C. F. Driscoll, R. A. Smith, X.-P. Huang, and J. H. Malmberg, "Growth and Decay of Vortex Structures in Pure Electron Plasmas," in *Structures in Confined Plasmas*, Proc. of Workshop of US-Japan Joint Institute for Fusion Theory Program, Report No. NIFS-PROC-2, 69, (National Institute for Fusion Science, Nagoya, 1990).

7. X.-P. Huang, C. F. Driscoll, and J. H. Malmberg, "Experimental Measurements of the Decay of 2D Turbulent Fluctuations Embedded in Sheared Background Flows," Plasma Div., APS, Tampa, *Bull. Am. Phys. Soc.* **36**, 2331, (1991).

8. X.-P. Huang, C. F. Driscoll, and J. H. Malmberg, "Measurements of the Relaxation of 2D Turbulent Fluctuations Embedded in a Sheared Rotational Background," Plasma Div., APS, Seattle, *Bull. Am. Phys. Soc.* **37**, 1415, (1992).

9. X.-P. Huang and C. F. Driscoll, "Relaxation of 2D Turbulence to a Meta-Equilibrium Near the Minimum Enstrophy State," submitted to *Phys. Rev. Lett.*, 1993.

10. X.-P. Huang, C. F. Driscoll, and K. S. Fine, "Observations of Coherent Density Holes in Freely Decaying 2D Turbulence in Magnetized Electron Columns," in preparation, 1993.

Fields of Study

Major Field: Physics

Studies in Plasma Physics
Professors Thomas M. O'Neil, Marshall N. Rosenbluth,
Ronald E. Waltz, Patrick H. Diamond, and Daniel H. E. Dubin

Studies in Classical Mechanics
Professor Thomas M. O'Neil

Studies in Electromagnetism
Professor Donald R. Fredkin

Studies in Quantum Mechanics
Professor Julius Kuti

Studies in Statistical Mechanics
Professor Andrei E. Ruckenstein

Studies in Mathematical Physics
Professor Frank B. Thiess

Studies in Quantum Field Theory
Professor Julius Kuti

Abstract of the Dissertation

Experimental Studies of Relaxation of Two-Dimensional Turbulence in Magnetized Electron Plasma Columns

by

Xiao-Pei Huang

Doctor of Philosophy in Physics

University of California, San Diego, 1993

Dr. Charles F. Driscoll, Chairman

Freely evolving $\mathbf{E} \times \mathbf{B}$ drift turbulence has been studied in magnetized electron columns, which follow the same (r, θ) dynamics as 2D incompressible fluids. Experimentally, plasma columns are confined inside conducting cylinders in a uniform axial magnetic field, and are measured with two density (vorticity) diagnostics: a multi-collector array and a phosphor screen/CCD camera.

An initially hollow column undergoes unstable diocotron mode growth, vortex formation, and convective transport. This results in large-amplitude turbulent fluctuations, and a monotonically decreasing density profile with sheared rotation. In this thesis, quantitative measurements on the decaying 2D turbulence are presented, and detailed comparisons are made to theories of 2D relaxation.

The entire free relaxation process lasts several hundred column bulk rotations, and can be roughly divided into three phases. Phase I is characterized by the rapid filamentation and mixing of turbulent density clumps (electron surpluses) and shallow holes (deficiencies) in the shearing background rotation. Phase II is

dominated by the remaining elongated medium-size holes, which are prograde and thus can survive the background shear. These holes consolidate into azimuthally symmetric configurations through mutual interactions such as occasional merger. In Phase III, these coherent holes slowly drift radially outward and are finally axisymmetrized with respect to the column center, giving the meta-equilibrium state of the 2D relaxation.

The meta-equilibrium column persists for about 10^4 rotations, before eventually decaying away due to 3D dissipation. Between the initial and meta-equilibrium states, the number of electrons (circulation), angular momentum, and energy are well conserved, while the enstrophy and mean-field entropy vary significantly. The measured meta-equilibrium radial profiles exhibit close agreement with the minimum enstrophy vortices predicted by the "selective decay " hypothesis. In contrast, predictions of maximum entropy theories differ substantially from the experimental data. Small-amplitude ($\sim 2\%$) shot-to-shot variations in the meta-equilibrium profiles have also been observed, reflecting the random motions involved in the relaxation.

Chapter 1

Introduction and Overview

1.1 Introduction

Turbulent flows occur in a wide variety of physical systems, ranging from earth's atmosphere to hot fusion plasmas confined in thermonuclear reactors [33, 92]. Although there is no rigorous scientific definition of turbulence, a turbulent flow must exhibit randomness in both space and time, excitations of many degrees of freedom, and extensive mixing of fluid elements. Due to the complexity of the nonlinear interaction, a comprehensive physical picture of turbulence is still elusive, and it remains "the last great unsolved problem of classical physics," as was dubbed by Richard Feynman. Turbulence appears to behave differently from one system to another, depending on the flow dynamics involved, as well as on the initial and boundary conditions. Scientific research has been concentrated on finding universal properties that can provide a clear physical understanding of the observed phenomena [66].

Under certain conditions, a three-dimensional physical system can be modeled by neglecting one of the spatial degrees of freedom. For example, geophysical phenomena such as mesoscale oceanic and atmospheric flows are approximately two-dimensional, due to the effects of earth's rotation and the relatively small vertical extent of the flows [72]. In addition, the macroscopic behavior of strongly magnetized plasmas is often 2D-like, due to the "stiffening" effect of the confining magnetic

field [42]. Other 2D flows include thin liquid films, cryogenic superfluids, and self-gravitating disk galaxies [41].

The 2D dynamics of incompressible fluids has been studied for over a hundred years [41]. In the inviscid limit, a 2D flow is simply the advection of scalar fluid vorticity; for this reason, 2D turbulence exhibits some intriguing features quite different from its 3D counterpart. For example, as the turbulence evolves, the kinetic energy of the flow tends to condense into large 2D vortices, rather than being transferred to small spatial scales. Freely evolving 2D turbulence is of particular interest, since the lack of external forcing eliminates unwanted complications. Recently, insights on free turbulence relaxation have been obtained through extensive analytical and computational studies, partially motivated by the availability of high performance computers. The laboratory experiments are relatively few [93], however, mainly because it is difficult to devise a well-diagnosed experimental system with low dissipation and a high degree of two-dimensionality.

Research on non-neutral plasma physics began in the early 1960s when collective effects were explored in electron beam experiments [15]. In the past twenty years, non-neutral plasmas confined in traps have been intensively studied both experimentally and theoretically. Many properties of magnetically confined pure electron plasmas have been elucidated; and experiments on trapped pure ion, positron, antiproton plasmas are also making rapid progresses. A wide range of applications are possible [77], such as laser-cooled pure ion plasmas for the next generation of ultra-high precision clocks [97].

A magnetically confined pure electron plasma column can be considered as "two-dimensional" when the electron axial bounce motion is much faster than the guiding-center $\mathbf{E} \times \mathbf{B}$ drift in the (r, θ) plane perpendicular to the magnetic field. In this regime, the column 2D dynamics is governed by the Euler equation for 2D

incompressible inviscid fluids, with the electron density being proportional to the scalar vorticity. With low dissipation and accurate diagnostics, these magnetized electron columns provide excellent opportunities to study 2D Euler dynamics and turbulence. Here, the flow vorticity (density) can be directly measured with high speed and precision, allowing detailed quantitative comparisons with theoretical predictions.

In this thesis, I present experimental studies on the turbulent evolution of initially hollow electron columns confined in a Malmberg-Penning trap. After the creation of unstable initial configurations, columns are then completely isolated in the trap, without any forcing or damping from the outside. Therefore, the free evolution studied here is entirely driven by its own intrinsic dynamics. The initial hollow column is unstable to Kelvin-Helmholtz shear instabilities, called diocotron modes in the plasma literature. These instabilities and their saturation dynamics have been studied by Driscoll *et al.* [23, 19], and by other groups [80, 73]. Here, I will concentrate on the late-time relaxation period of the free evolution, emphasizing results obtained from the new CCD camera density diagnostics. The camera enables the identification of coherent density holes as the prominent feature in the relaxation process.

The initial instabilities and turbulence cause large-scale transport, but no plasma loss. Figure 1.1 shows a series of radial density profiles measured by a single mobile probe at various times (taken from [51]). Each small horizontal bar represents density of an individual shot measured at that particular radius, and the solid curve is the average constructed from many shots starting from essentially the same initial conditions. During early times (t = 0, 100 μs, and 150 μs), the hollow column exhibits growing shot-to-shot noise on its radial profile, reflecting the growth of unstable diocotron mode(s). At t = 200 μs, the noise has very large amplitude

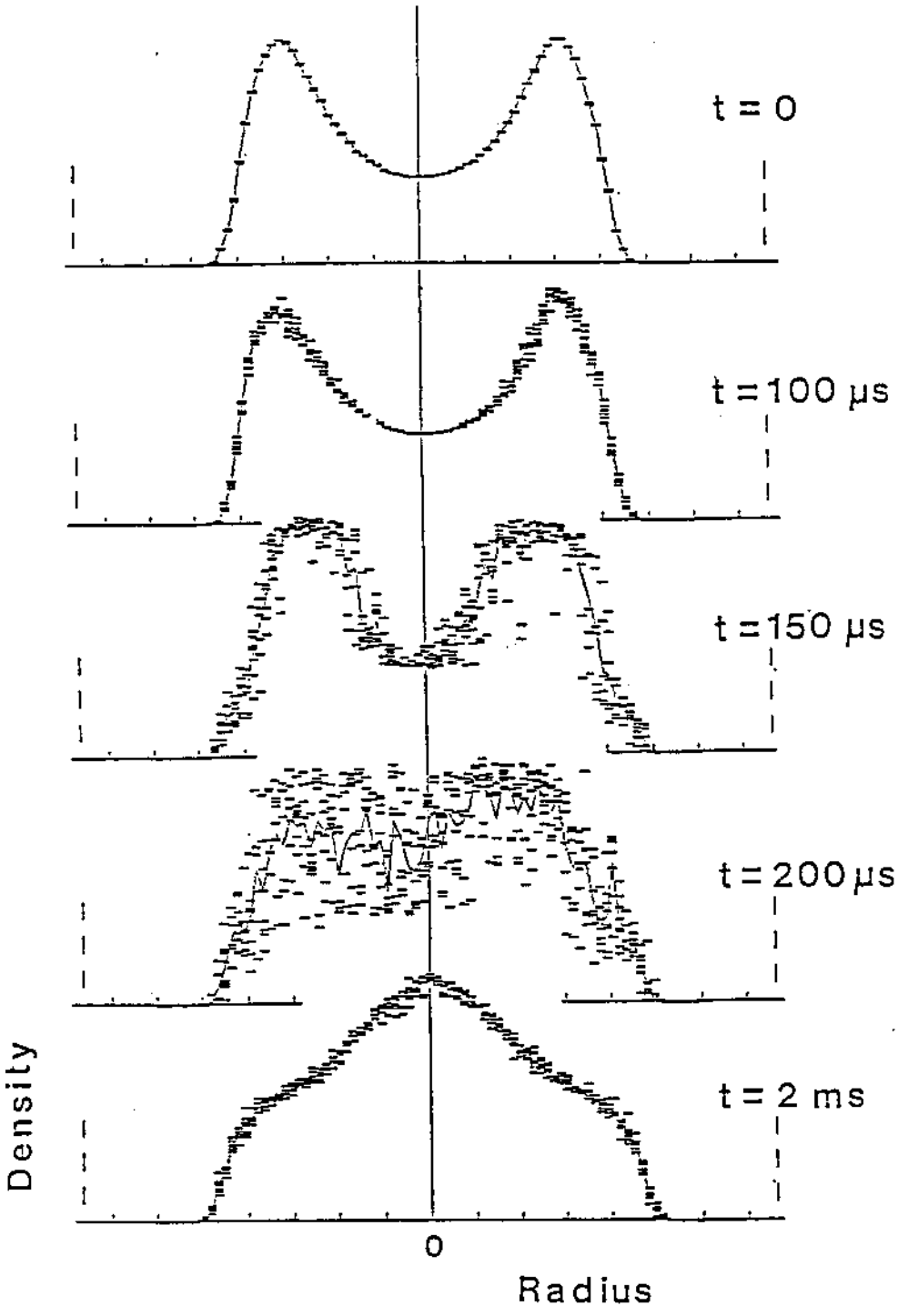

Figure 1.1: Many-shot radial density profiles at various times.

and the average profile is no longer hollow, due to the inward convective transport and turbulent fluctuations. By $t = 2$ ms, the column has relaxed to a monotonically decreasing density profile, with most of the noise decayed away. This thesis examines the free relaxation of this turbulence, i.e., the dynamics between $t = 200\,\mu$s and 2 ms as shown in Figure 1.1. The questions can be summarized as the following:

- How does the turbulence decay away in this system?
- What determines the final relaxed density distribution?

1.2 Overview of Dissertation

In Chapter 2, I discuss the experimental device (named V′) on which this research has been performed. The V′ apparatus was one of the original enlarged cylindrical Penning traps, now called Malmberg-Penning traps, which are utilized to magnetically confine non-neutral plasmas. The apparatus and the measurement diagnostic methods are described in detail. I also review the basic properties of trapped pure electron plasmas, with emphasis on the confinement behavior. Finally, several specific experimental techniques are discussed, which are used to create desired initial plasma conditions.

In Chapter 3, I review the theory of nondissipative two-dimensional $\mathbf{E} \times \mathbf{B}$ drift dynamics in magnetically confined electron columns. The $\mathbf{E} \times \mathbf{B}$ drift equations are the Euler equation for 2D incompressible inviscid (ideal) fluids. The vorticity of the electron flow is seen to be proportional to the electron density, and the total number of electrons is the total circulation of the flow. Further, the electron boundary conditions are equivalent to free-slip fluid boundaries. I also comment on the effect of dissipation and three-dimensionality to the ideal 2D dynamics. Theoretical insights on 2D turbulence phenomena are surveyed, with emphasis on the global conservation laws. Also considered is the Reynolds decomposition formalism that separates

2D turbulence into constituent mean background flow and turbulent fluctuations. Several experimental measurement methods and data processing techniques are described, including the CCD camera imaging of 2D density distribution, and ensemble averaging over many evolutions. The coarse-graining effect of finite-size collectors is analyzed in detail as well.

In Chapter 4, I present experimental measurements on the free relaxation process of 2D $\mathbf{E} \times \mathbf{B}$ drift turbulence in magnetized electron columns. The turbulence arises as a result of shear-flow instabilities on the initially hollow density distribution. These instabilities saturate with the formation of interacting nonlinear vortex structures, and the turbulence then relaxes after the inward convective transport establishes a globally stable, albeit turbulent column. The relaxation leads to a long-lived, quiescent 2D meta-equilibrium, which then decays due to 3D "viscous" particle transport. These features are illustrated by measurements from both single-shot CCD camera images and from ensemble averages using the multi-collector array, such as the fluctuation level and two-point correlations.

I find that the entire relaxation process lasts several hundred column bulk rotations, and can be roughly divided into three phases. Phase I is characterized by the rapid filamentation and mixing of turbulent density clumps (electron surpluses) and shallow holes (deficiencies) in the shearing background rotation. Phase II is dominated by the remaining elongated medium-size holes, which are prograde (rotating in the direction of the shear) and thus can survive in the rotational background, and are settling into symmetric configurations through mutual interactions such as occasional merger. In Phase III, these coherent holes slowly drift radially outward and are finally axisymmetrized with respect to the column center, giving the axisymmetric meta-equilibrium state of the 2D relaxation.

I demonstrate that as a result of the longevity of the deep density holes, the

observed noise decay time is 10–50 times slower than predicted by simple "passive tracer" mixing. The quasi-stability of the individual holes is quantitatively understood by the Moore-Saffman model based on the equilibration of an elliptical vorticity patch in a background flow with uniform shear. The tendency for the holes to settle into symmetric configurations in the column is explained by intuitive stability arguments on the hole-hole and hole-background interactions. The decline of the fluctuation level at late times, which apparently reflects the outward drift and final axisymmetrization of the density holes, can be approximated with an exponential decay. I present experimental measurements showing the dependencies of the fluctuation decay rate on radial position, on column axial length, and on magnetic field are all weak. These scalings are all consistent with 2D $\mathbf{E} \times \mathbf{B}$ drift dynamics.

In Chapter 5, I consider the relaxed meta-equilibrium state of the 2D turbulence, presumably reached through nearly inviscid, nonlinear interactions of the turbulent flow. I show that this 2D meta-equilibrium persists for over 10^4 column bulk rotations, until 3D dissipation drives the system toward its final thermal equilibrium. Quantitative experimental measurements of the meta-equilibrium state are presented, for comparison with theoretical predictions of point vortex and continuous fluid maximum entropy theories, and with minimum enstrophy models. I develop an analytical "restricted" minimum enstrophy model appropriate to the experimental constraints of density being non-negative and monotonic in radius.

I find experimentally that the number of electrons (circulation), angular momentum (angular impulse), and electrostatic energy (kinetic energy) are all well conserved during the evolution from the initial to the meta-equilibrium states. In contrast, less robust invariants, such as the enstrophy and mean-field entropy, vary significantly, apparently due to "viscous" dissipation or measurement coarse-graining of structures at the fine scales generated by the turbulence. I also find that the mea-

sured meta-equilibrium density (vorticity) profiles exhibit close agreement with the predictions of the restricted minimum enstrophy model, while differing substantially from maximum entropy predictions. Small-amplitude ($\sim 2\%$) shot-to-shot variations are observed in the meta-equilibrium profiles, apparently because the relaxation dynamics magnifies the shot-to-shot variations in the initial state. The gradual decay of the meta-equilibrium state caused by the microscopic "viscous" effects and external particle transport is briefly discussed.

In Appendix A, I describe the collector calibration procedure. In Appendices B – D, I present several theoretical and mathematical results that are used in the main text. Finally, frequently used symbols and notations are listed in Appendix E.

Chapter 2

Experimental Setup

2.1 Overview

In this chapter, I discuss the experimental device (named V′) on which this investigation has been performed. The V′ machine was one of the original enlarged cylindrical Penning traps, now called Malmberg-Penning traps, which were developed by Malmberg and his colleagues to study confined non-neutral plasmas [49, 16].

In the last two decades, many properties of pure electron plasmas confined in these traps have been carefully studied and characterized both experimentally and theoretically [51, 69]; furthermore, experimental techniques to manipulate and measure these plasmas have been perfected, paving ways for investigating more complex behaviors in such systems. Here, I do not attempt to cover all the aspects of these experiments; rather I give a brief review of those that are directly related to the theme of this thesis, i.e., experimental studies on the relaxation of two-dimensional $\mathbf{E} \times \mathbf{B}$ drift turbulence.

In Section 2.2, I describe the machine apparatus and the measurement diagnostic methods. Section 2.3 is devoted to a review of basic properties of trapped pure electron plasmas. Finally in Section 2.4, several experimental techniques is discussed, which are used to create desired plasma initial conditions.

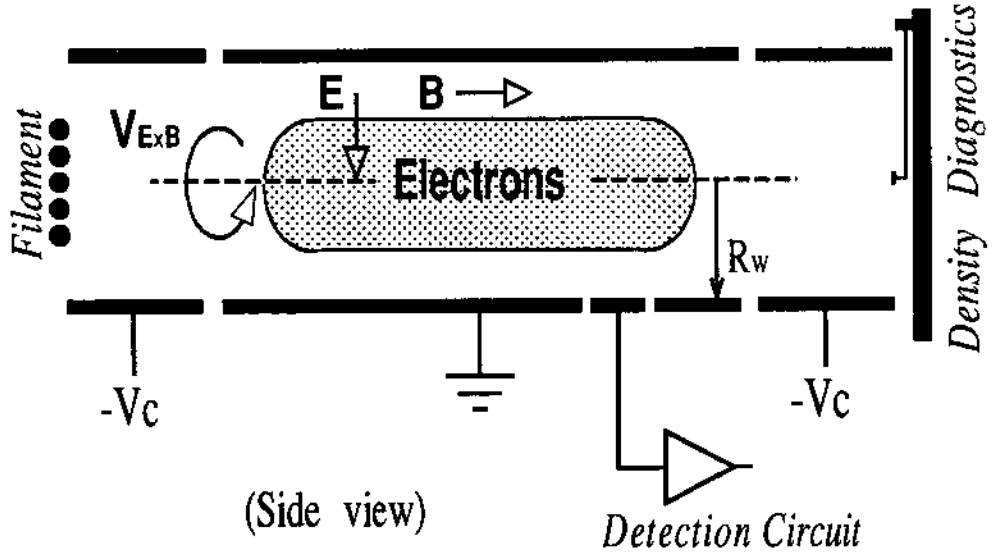

Figure 2.1: Basic configuration of a Malmberg-Penning trap.

2.2 Experimental Apparatus

2.2.1 Malmberg-Penning Traps

Figure 2.1 shows a simplified schematic of the experimental confinement device. A series of concentric conducting cylinders (radius $R_w = 3.05\,\mathrm{cm}$) are enclosed in ultra-high vacuum ($\lesssim 10^{-9}$ torr) and immersed in a uniform background axial magnetic field $\mathbf{B} = B_z\hat{\mathbf{z}}$. These cylindrical electrodes are electrically isolated from each other and can be independently biased from outside the machine. Plasmas are formed from electrons emitted by a negatively biased spiral tungsten filament shown at the left of the illustration. Experiments typically run in cycles of inject-manipulate-hold-dump actions at repetition rates up to 60 Hz, providing possibilities for high-speed data acquisition.

At the beginning of each cycle, the injection cylinder on the left is temporarily grounded, allowing the electrons to enter the confinement cylinder at the center. This

electron cloud is then trapped by biasing the injection cylinder at a large negative confinement voltage $-V_c$, typically around -150V. The dump cylinder on the right is generally biased at the same confinement voltage $-V_c$ during this injection/trapping process, so that the column can not escape axially to the right. The axial confinement of the column is thus assured by the large energy barriers provided by the end cylinders. The unneutralized space charges produce a strong repelling electric field $\mathbf{E}$, generating rotational $\mathbf{E} \times \mathbf{B}$ drift motion in the column [12]. The column is therefore radially confined by the balancing Lorentz $\mathbf{v} \times \mathbf{B}$ force, where $\mathbf{v}$ is the $\mathbf{E} \times \mathbf{B}$ drift velocity [14].

The density and temperature of these electron clouds are such that they are typically in the plasma state, i.e., coherent collective interactions, rather than individual particle effects, dominate the dynamics of the system [12]. Various experimental and theoretical studies have established the unique confinement property of these plasmas, which is reviewed in detail in the next section. These plasmas can typically be confined for a few seconds [50], or about 10^6 $\mathbf{E} \times \mathbf{B}$ bulk rotations, providing ample time to perform a variety of high-quality plasma experiments. For turbulence experiments on initially hollow columns, one generally first obtains quiescent stable plasmas, then creates the unstable hollow initial conditions by ejecting some electrons from the central region of these columns. This technique is described in Section 2.4.

At time t after the creation of hollow initial conditions, the z-averaged electron density can be measured by grounding the dump cylinder, letting the column escape axially onto the positively biased density diagnostics at the right in Figure 2.1. Since this axial "streaming-out" process is typically much faster than any 2D drift motion in the perpendicular (r, θ) plane, the column essentially preserves its 2D structure, allowing accurate 2D density measurements [64]. This dump/diagnose

process is inherently destructive in nature, i.e., one can not follow the temporal evolution of a particular column, since it has to be destroyed in order to carry out the measurement. In this thesis, two kinds of 2D density diagnostics are used: an end-plate multi-collector array and a phosphor screen/CCD (Charge Coupled Device) camera. I discuss these diagnostics in the following sections.

The whole cycle (called a plasma shot) can be repeated time after time, generally with a high degree of reproducibility. For example, the creation of the initial hollow columns has shot-to-shot variations in measured density less than 0.5%. If an evolution does not involve instabilities, one can follow the evolution accurately utilizing the reproducibility of the system. An example is the off-axis dynamical equilibrium state (nonlinear $l = 1$ diocotron mode) investigated by Fine [27]. However, if the evolution under study is intrinsically unstable, such as in chaos or turbulence, statistical approaches must be employed, since one can not reproducibly follow a given evolution for long times. Chapter 3 deals with this issue extensively.

An independent diagnostic method, which is non-destructive in nature, involves measuring image charges induced on wall electrodes at various axial positions of the apparatus [27, 60]. As shown in Figure 2.1, azimuthally partitioned "sector" probes are used to detect and drive waves in the confined electron plasmas. These sectors can also be biased electrostatically to change the boundary conditions at the wall [67]. In addition, the total electric charge within a particular cylinder can be independently determined by measuring the image charges when a column is injected or dumped. This "Gauss' law" method is used to obtain the number of electrons per unit length N_L at the axial midpoint of a column, and can therefore be used to obtain the axial length L_p of the column.

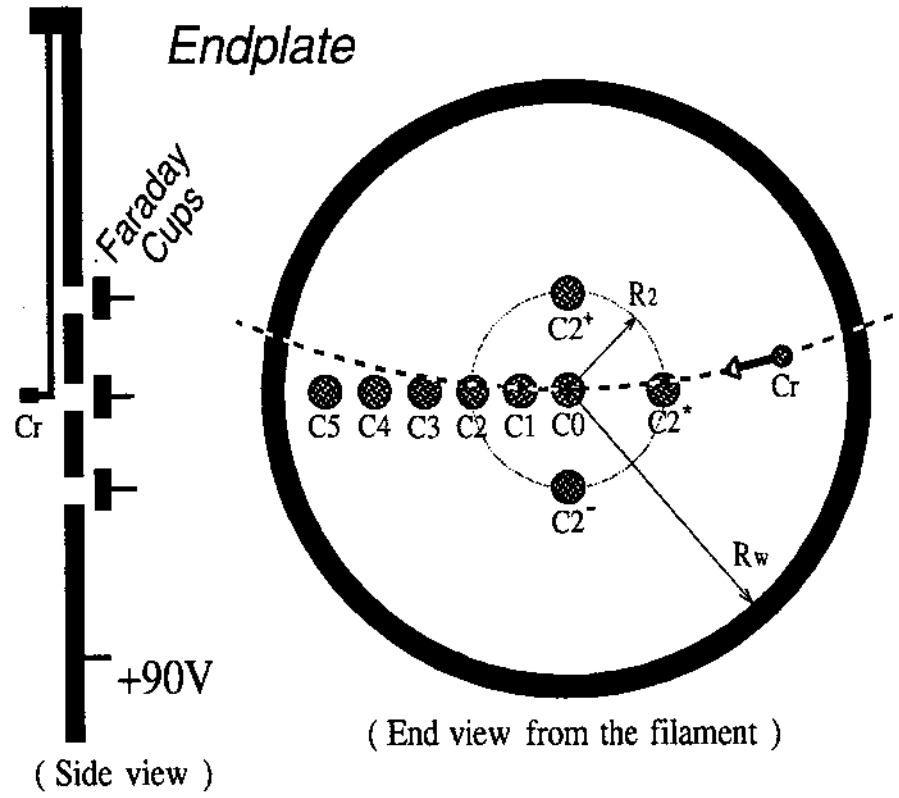

Figure 2.2: Endplate multi-collector array density diagnostic.

2.2.2 Multi-Collector Array Density Diagnostic

One 2D density diagnostic method, which has been the traditional choice, utilizes the endplate multi-collector array shown in Figure 2.2. The conducting endplate, which is biased at +90 V, has nine collimator holes (diameter $2R_{C0}$ = 0.40 cm), with electrically isolated Faraday cups behind each hole. Six collectors, C0 $\rightarrow$ C5, line up along $\theta = 0$ at positions $R_j = 0.54 \times j$ cm; collector C2, $C2^+$, $C2^*$, $C2^-$ are located on a circle of radius $R_2 = 1.08$ cm with 90° azimuthal angular separation. In addition to the fixed collectors, a mobile collector Cr (diameter $2R_{Cr}$ = 0.20 cm) can be positioned at any location along an arc of radius 5.85 cm, which lies

approximately on the $\theta = 0$ line near the cylindrical axis.

This configuration enables one to measure the density at ten different positions at any time during the evolution. The voltage induced by the electrons collected on each collector is then amplified and processed, giving ten independent data channels. The whole measurement process is controlled by a microcomputer, with the density data read and stored electronically for further analyses.

For cross-field $\mathbf{E} \times \mathbf{B}$ drift motions studied here, one can generally neglect 3D density variations such as axial waves and column end shapes [19]. Here, this 2D assumption implies that a trapped electron column is treated as a section of an infinitely long column without any axial variations. The 2D density n can then be calculated from the charge Q_j on collector Cj, the calibrated cross section A_{Cj} (see Appendix A for details), and the column axial length L_p:

$$n(r_j, \theta_j) \equiv \frac{Q_j}{eA_{\mathrm{Cj}}L_p}\,, \tag{2.1}$$

where (r_j, θ_j) is the central position of collector Cj. The axial length L_p is determined through the relation

$$L_p \equiv \frac{N_e}{N_L}\,, \tag{2.2}$$

where N_e is total number of electrons in the trap as measured on the entire endplate, and N_L is the number of electrons per unit length at the axial midpoint of the column determined from the wall image charges as described above.

Alternatively, L_p can be obtained self-consistently by solving the 3D Poisson equation, using the measured electron parallel temperature $T_{\|}$ and radial profile $Q_r(r)$ [27]. Note that this method assumes that the density distribution is axisymmetric, and that electrons on each magnetic field line are in parallel equilibrium. Normally, these two methods yield answers within $\pm 5\%$ of each other, especially in columns with $L_p \gg \lambda_D$, since the Debye length λ_D is a rough measure of the length of the column end region.

Since the collectors have finite sizes, the measured density is necessarily the average value of the real density distribution over the cross sections of the collectors. When the density distribution has only large-scale structures, the collectors should be able to resolve all the features of the distribution. However, in cases where fine-scale structures are present, the averaged density may deviate from the real density at the collector center. In Chapter 3, I will present a detailed evaluation of this coarse-graining effect of the finite-size collectors. The basic conclusion is that a collector of radius R_C can only resolve structures with scale-length $\gtrsim 3R_C$, with any finer distributions being averaged out. Despite its limitations, the multi-collector array density measurement still has the advantages of being easy to calibrate and free from dump-induced distortions, offering a reliable way of measuring the density.

2.2.3 Phosphor Screen/CCD Camera 2D Density Imaging

The multi-collector array gives density readings at only ten positions for each shot, insufficient to construct a snapshot of the 2D density distribution. As part of the testing procedure for a next generation Malmberg-Penning trap, a phosphor screen/CCD camera density diagnostic was installed on the V′ machine, permitting the imaging of the complete $n(r,\theta)$ from a single plasma shot [30].

Figure 2.3 is a simplified schematic of this new diagnostic system. Here, the endplate is replaced with a phosphor screen coated with a thin layer (thickness $\sim 0.15\ \mu$m) of aluminum, with an effective imaging area ~ 1.80 cm in radius. The purpose of the aluminum coating is to block the stray light generated by the filament source at 1800° K. The screen is positioned about 15cm away from the dump cylinder. A series of thin metal plates (accelerating plates), with the first one grounded, are connected in series by 10MΩ resistors, with the last one attached onto the aluminum coating of the screen. The screen is biased at a high positive voltage (normally ~ 15 kV). These plates create a smooth potential gradient, so that exiting electrons

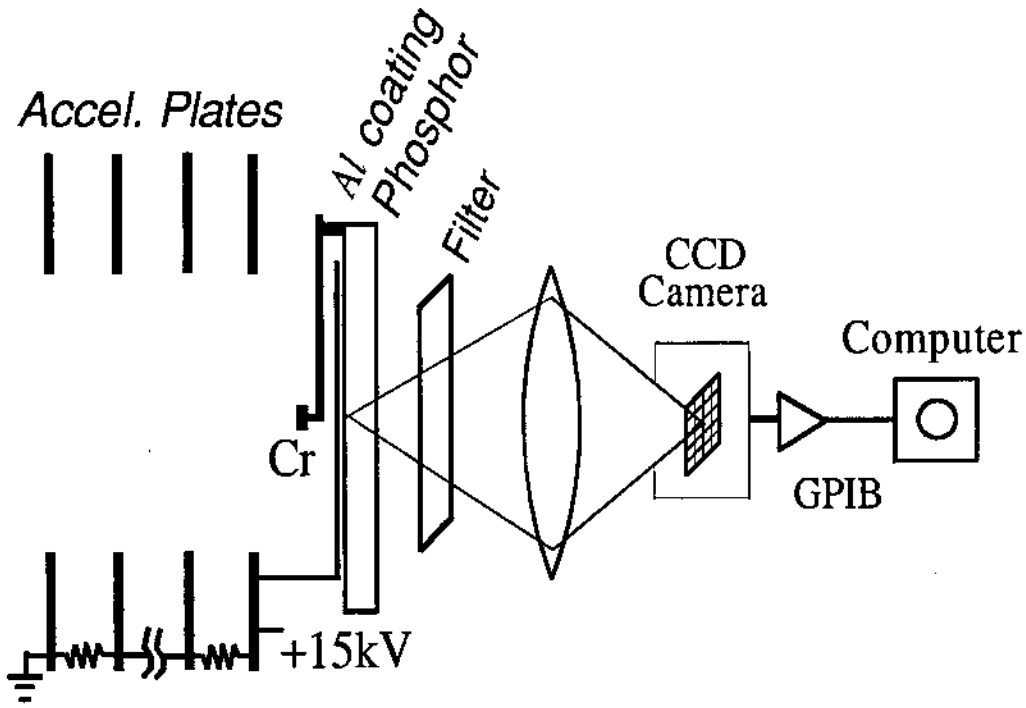

Figure 2.3: Phosphor screen/CCD camera density imaging system.

experience an axial acceleration to 15 keV over the entire 15 cm distance, minimizing the distortions on the 2D density distribution [63, 29].

Tests indicate that the intensity of the fluorescent light generated by the high energy electron impacts is locally proportional to the number of electrons collected per unit area. The 2D light intensity distribution is then imaged, through a transparent view-port, by a CCD camera located outside the vacuum chamber and focused on the phosphor screen. A conventional optical filter further reduces the reddish filament light, without degrading the green-blue phosphor fluorescent light signal. Results show that after aluminum blocking, optical filtering, and numerical subtraction, the "noise" due to the background stray light is typically less than 1% of the light signal induced by the electrons [30].

Presently, the dominant error in measuring $n(r,\theta)$ is a repeatable 15% gain variation over the phosphor screen surface, probably caused by slight differences in the thickness of the aluminum coating. This problem is overcome by a 2D gain calibration procedure. Here, one measures a reproducible axisymmetric electron column with both the calibrated mobile collector Cr, as shown in Figure 2.3, and the phosphor screen/CCD camera. Any variations of the camera image from the measured radial profile are thus assumed to be caused by this error, and can be corrected using a 2D gain function associated with each location (r,θ).

2.3 Basic Properties of Trapped Pure Electron Plasmas

This section is devoted to the description of a few relevant plasma parameters and the fundamental confinement property of trapped pure electron plasmas. The wall radius R_w of the conducting cylinders is 3.05 cm; the axial length of the confinement cylinder(s) can vary from 3.05 cm to 113 cm by using various cylinder configurations [16]. The background axial magnetic field B_z may be set from 50 G up to 700 G, although most of the experiments considered here have $B_z \gtrsim 400$ G. The background neutral pressure is always kept below 1×10^{-9} torr, ensuring that the electron-neutral collision is negligible [50].

While the axial length L_p of a trapped column is set by the length of the confinement cylinder(s), its radius is determined by the applied conditions on the source filament [16]; the half-peak-density radius R_p ranges from 0.5 cm to 2.5 cm, while columns with larger than 2.5cm radius are generally in contact with the cylinder wall. For columns studied in this thesis, the electron density n is generally less than $5 \times 10^7 \mathrm{cm}^{-3}$, and the electron temperature T is typically around 1 eV. The average electron gyroradius R_L is around 50 μm (at $B_z \simeq 500$ G), and the plasma Debye

length λ_D is approximately 2.5 mm (for $n \simeq 1 \times 10^7$ cm^{-3}); both are much smaller than the column dimensions R_p and L_p. This fact indicates that these columns are indeed in the plasma state, and that the electrons are closely tied to the magnetic field lines, except for guiding-center drift motions.

The average electron axial bounce frequency $\gamma_b \simeq 1$ MHz (for $L_p \simeq 20$ cm), which is much faster than the column bulk $\mathbf{E} \times \mathbf{B}$ rotation frequency $\omega/2\pi \simeq 100$kHz, suggesting that the column is basically 2D like [69]. In addition, the electron-electron like particle collision time τ_{ee} is about 10 ms, making the relatively "fast" drift dynamics under consideration essentially collisionless [37].

The electron injection process is now a well controlled experimental operation, enabling one to obtain various quiescent electron plasma columns with a high degree of reproducibility. These plasmas can be manipulated to be on-axis and macroscopically stable, with axisymmetric, monotonically decreasing density profiles. The confinement property of these plasmas has been the subject of extensive studies for many years. Theoretically, if there were no field errors that break the cylindrical symmetry, these columns would be confined indefinitely, due to the conservation of the total canonical angular momentum of the electrons [68, 69]. Consequently, the experimentally observed outward particle transport must be due to microscopic effects caused by the field errors in the trap.

Malmberg and Driscoll investigated the plasma confinement behavior in the V′ machine [50, 21]. They characterized the confinement time, τ_m, as the time it takes for the central density to drop by a factor of two, and measured the dependence of τ_m on the axial length L_p and the magnetic field B_z. The result is summarized in Figure 2.4, where graph (a) shows measured density profiles for a particular column ($L_p = 20$ cm, $B_z = 507$ G) at early times ($t = 5$ ms), and near τ_m ($t = 5$ s), with graph (b) showing τ_m versus the ratio L_p/B_z for many different columns. Over six orders

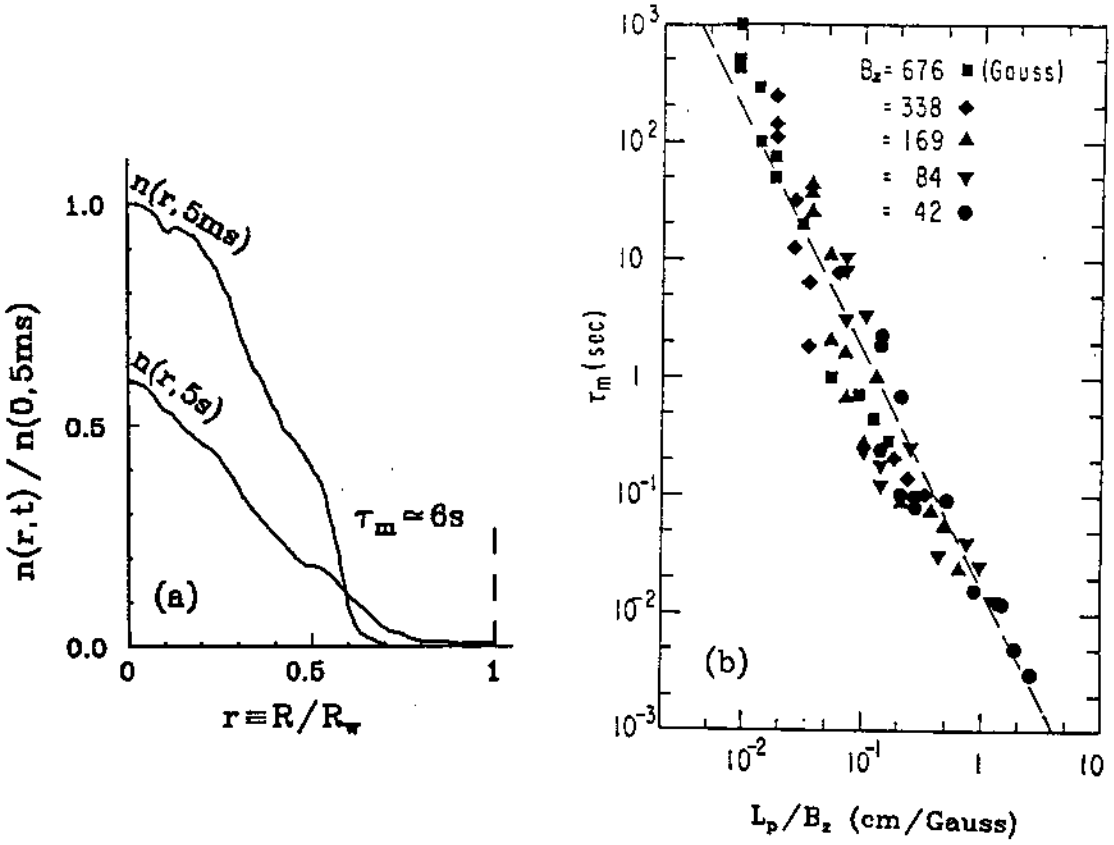

Figure 2.4: $(L_p/B_z)^{-2}$ scaling of confinement time in V'. (a) Density profiles at $t = 5$ ms and $t = 5$ s $\simeq \tau_m$; (b) confinement time τ_m versus L_p/B_z from many experiments.

of magnitude in confinement time τ_m, the data approximately follow the empirical scaling law, as represented by the dashed line in Figure 2.4(b),

$$\tau_m \simeq 10\,\mathrm{s} \times \left(\frac{L_p}{20\,\mathrm{cm}}\right)^{-2} \left(\frac{B_z}{500\,\mathrm{G}}\right)^{2}. \tag{2.3}$$

Therefore, for a 20 cm long column in a 500 G magnetic field, the confinement time τ_m is roughly 10 s. It is clear from Equation (2.3) that shorter columns with stronger magnetic field tend to stay longer in the V' device.

Another apparatus (named EV) was later built with special care to minimize various field errors. The new device shows a twenty-fold improvement in confinement, with the same L_p/B_z dependence [20]. This suggests that the observed transport is

indeed caused by trap imperfections, through an unknown common mechanism of "anomalous" external transport.

A very short column may be confined long enough so that it can first reach its 3D thermal equilibrium through internal (angular momentum conserving) transport [75, 22, 25]. For the 2D $\mathbf{E} \times \mathbf{B}$ drift dynamics, both the internal and external transports are considered as dissipation. The 1–10 second time scale associated with these dissipative effects indicates that they are quite negligible compared to the $\mathbf{E} \times \mathbf{B}$ drift motions on the 1 ms time scale, thus making the 2D fast dynamics effectively inviscid. I will come back to the question of dissipation in Chapter 3.

2.4 Experimental Manipulation of Columns

In this section, two relevant experimental procedures are discussed: a procedure to create unstable hollow columns; and techniques to detect, drive, and feedback control various modes in the trap.

2.4.1 Creation of Hollow Columns

Experiments on 2D $\mathbf{E} \times \mathbf{B}$ drift dynamics typically start with the creation of various stable or unstable initial conditions, which then evolve freely without further intervention from the outside. Many interesting initial distributions have been created from near thermal equilibrium stable columns, among them, the multi-column configurations [60], thin annular distributions [80, 73], and hollow columns [19]. This work is mainly concerned with the evolution of hollow columns, especially the relaxation of turbulence after the initial stabilities.

Figure 2.5 is a schematic illustrating the procedure to create a hollow column. First, an on-axis, quiescent column with monotonically decreasing radial density profile is obtained (top). Second, the negative bias on the filament is converted to positive 20 V, and the confinement voltage $-V_c$ on the injection cylinder is temporar-

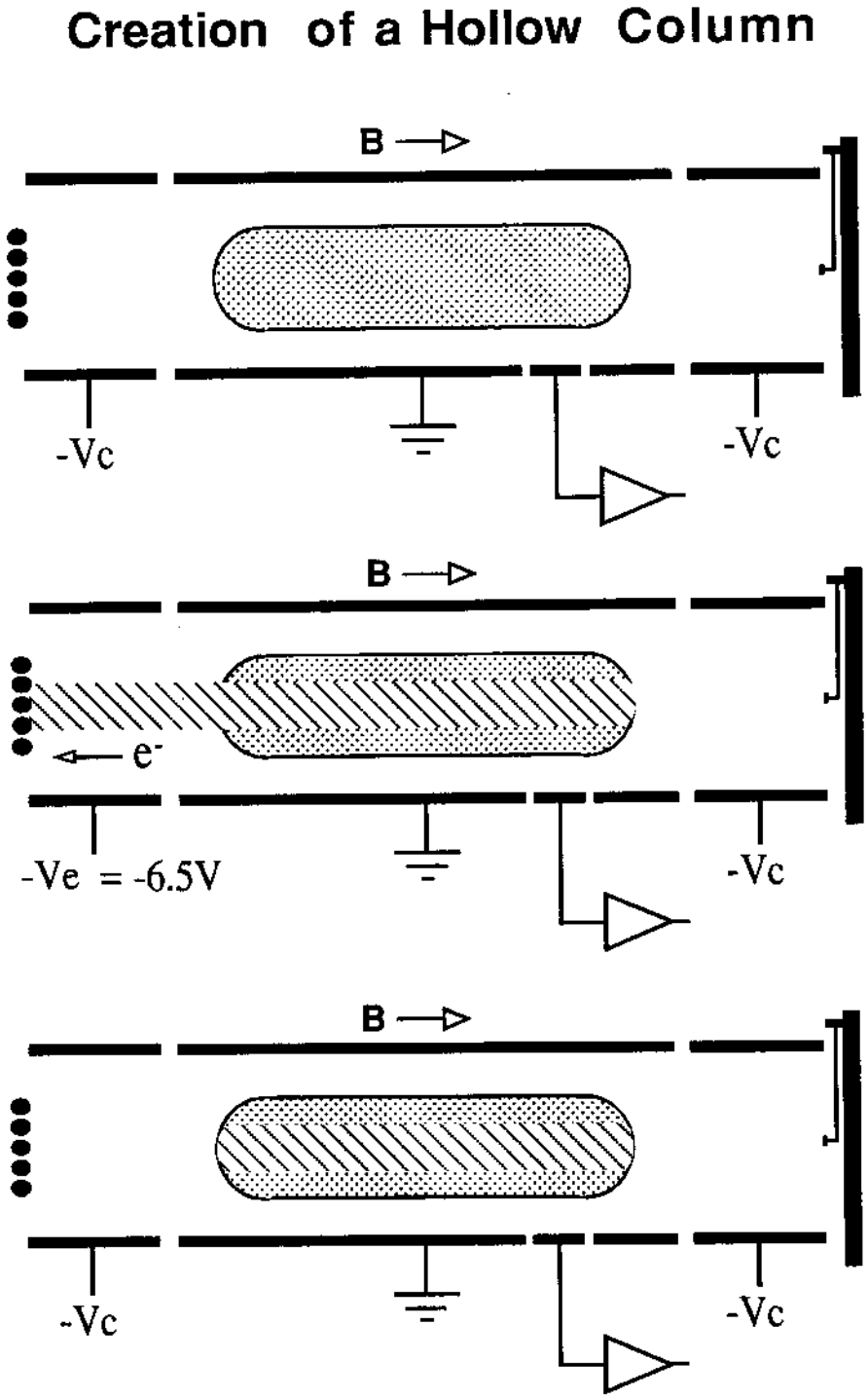

Figure 2.5: Schematic of hollow column creation process.

ily raised to the ejection voltage $-V_e$ (generally between -10 V to -2 V), allowing electrons from the central region of the column to escape axially and be absorbed by the filament (middle). Finally, after about $10\,\mu$s, the injection cylinder is ramped back down to $-V_c$, isolating the column again from the filament (bottom). A hollow column is therefore obtained and starts its free evolution. Note that the closing of the ejection pulse is designated as $t = 0$ for the subsequent evolution.

Shown in Figure 2.6 are the radial profiles of the plasma density and potential before and after the ejection process, which are constructed by using the mobile collector Cr from many reproducible shots. Just before hollowing, the column has peaked density and potential radial distributions, shown as dashed curves in Figure 2.6 (a) and (b) respectively. The ejection voltage is marked as the dot-dashed line in Figure 2.6 (b), with $-V_e \simeq -6.5$ V in this case. After hollowing (solid curves), the density profile is clearly hollow, with the central density dropping by more than a factor of five, and the potential profile is approximately flat near the center, at a level slightly above $-V_e$. This is consistent with the physical picture that all the electrons with total energy higher than eV_e, which is the sum of potential and kinetic energy, have escaped from the column to the filament. Similarly, hollow columns with various "width" and "depth" can be created by using different initial stable columns and ejection voltage $-V_e$.

This ejection process is well controlled and repeatable experimentally. From shot-to-shot, the reproducibility of the pre-ejection column is normally better than 0.2%; after ejection, the hollow profiles typically varies less than 0.5%, apparently mainly due to the reduction in the amplitude of the density itself. This high degree of reproducibility of the unstable initial conditions makes it possible to carry out the ensemble averages discussed in Chapter 3.

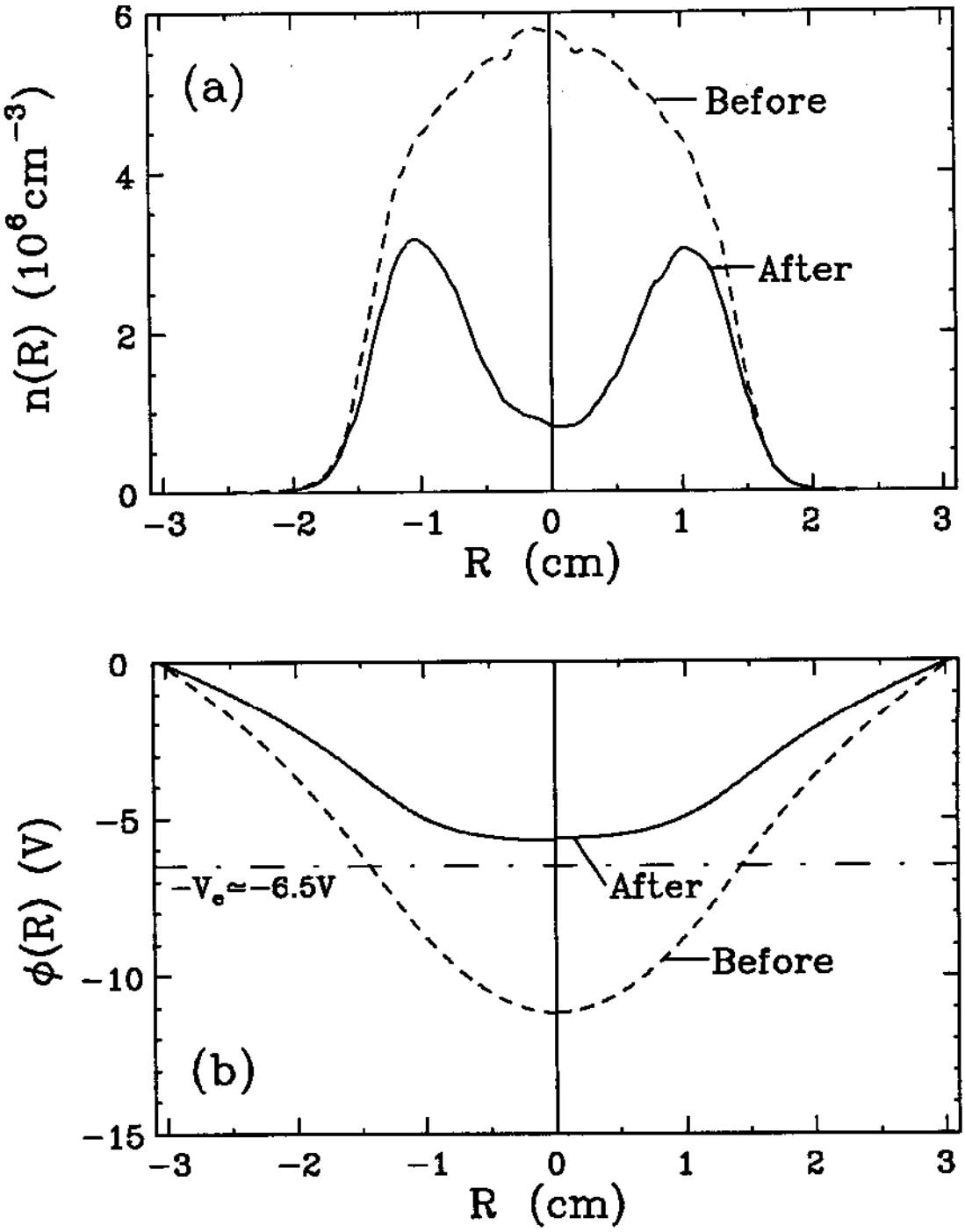

Figure 2.6: Radial profiles of the density and potential before and after hollowing. (a) Density n; (b) potential ϕ, with the ejection potential $-V_e \simeq -6.5$ V shown as the dot-dashed line.

2.4.2 Detection and Control of Modes in Non-Neutral Plasmas

One of the most fundamental properties of plasmas is that they support coherent oscillations, or modes. In particular, many modes in these magnetically confined non-neutral plasmas have been investigated and characterized both experimentally and theoretically [16, 75, 34].

The simple electron plasma modes are the column compression-rarefaction motions along the parallel axis, which were first studied in Malmberg-Penning traps by deGrassie and Malmberg [17]. These plasma mode(s) are normally excited to some extent by the ejection process that creates a hollow column. Generally speaking, the plasma mode frequencies are greater than 5 MHz for the density range I am considering here, much faster than the 2D $\mathbf{E} \times \mathbf{B}$ drift motion; therefore, any axial variations caused by this mode are averaged out over the slow 2D $\mathbf{E} \times \mathbf{B}$ drift time scale. Furthermore, these oscillations are quickly damped after the initial excitation, typically within 500μs, presumably through interaction with the "resonant" electrons which convert the wave energy into particle kinetic energy – a fundamental process called Landau Damping [12]. Consequently, plasma mode(s) does not appear to interfere with the column 2D drift motions in the (r, θ) plane.

Another class of oscillations are the diocotron modes, which are associated with the $\mathbf{E} \times \mathbf{B}$ drift motions in the (r, θ) plane perpendicular to the magnetic field. Each mode is characterized by its azimuthal mode number l, where the mode density perturbation varies as $\exp(il\theta)$. For example, the $l = 1$ diocotron mode for a stable column is simply the column center-of-mass motion when it is shifted off-axis. The column executes a circular orbit around the cylindrical axis, due to interaction with the image charges on the wall. This mode is very stable and observed to last up to 10^5 column bulk rotations [27]. The diocotron modes can be detected using a

sector probe described in Section 2.2. In addition, a feedback circuit can be utilized to amplify the detected mode signal, shift its phase, and then apply the processed signal back on another sector probe, making the mode either grow or damp in its amplitude [27].

Generally speaking, when a hollow column is created, the diocotron modes are also being excited. While the amplitude of $l \geq 2$ modes are normally small, the robust $l = 1$ mode can have a moderate amplitude, corresponding to a center-of-mass displacement of approximately 1 mm. Interestingly, I find that the amplitude of this $l = 1$ stable mode remains roughly constant during the turbulent evolution of hollow columns I have studied, even though there exists no rigorous theoretical proof that it is a constant of motion. If this mode is not damped, the measured late-time fluctuations will be dominated by this coherent center-of-mass orbital motion, masking the interesting dynamical effects. This complication can be eliminated by carefully growing the $l = 1$ mode with the right amplitude and phase prior to the ejection, so that the center of mass of the hollow column begins and always remains on axis throughout the free evolution. A negative feedback circuit can also be turned on, to ensure that the $l = 1$ mode does not grow later.

One can also intentionally excite $l \geq 2$ modes in electron columns before hollowing, creating initial conditions with perturbations having a preferred l symmetry. For example, a $l = 2$ diocotron mode (Kelvin mode) can be excited through feedback growth, resulting in an evolution dominated by the $l = 2$ instability. Note that unlike $l = 1$ center-of-mass mode, $l \geq 2$ diocotron modes are generally damped by the resonant electrons through the 2D spatial Landau damping [9, 16].

Chapter 3

Fundamentals of 2D $\mathbf{E} \times \mathbf{B}$ Drift Turbulence

3.1 Overview

In this chapter, I review the nondissipative two-dimensional $\mathbf{E} \times \mathbf{B}$ drift dynamics in magnetically confined electron columns. The same dynamics can also be readily applied to various pure ion systems. The isomorphism with the Euler dynamics that governs 2D incompressible inviscid (ideal) fluids is discussed in detail. I also examine the boundary conditions for the trapped columns, and comment on the effect of dissipation and three-dimensionality to the ideal 2D dynamics.

Theoretical insights on 2D turbulence phenomena are surveyed, with emphases on the global conservation laws and the Reynolds decomposition formalism that separates the 2D turbulence into constituent mean background flow and turbulent fluctuations.

I also describe experimental measurement methods and data processing techniques, including CCD camera imaging of the 2D density distribution, and ensemble averaging over many evolutions. The coarse-graining effect of finite-size collectors is analyzed in detail as well.

3.2 2D E × B Drift Dynamics

In classical mechanics, a charged particle in a magnetic field **B** executes circular gyromotion around its guiding center with angular velocity $w_c = q|\mathbf{B}|/mc$, where q and m are the charge and mass of the particle respectively, and c is the speed of light in vacuum. For a collection of particles of the same species with temperature T, the average radius of this gyromotion is called the gyroradius or Larmor radius [12], $R_L = c(2mk_BT)^{\frac{1}{2}}/q|\mathbf{B}|$, with k_B being the Boltzmann constant.

Under typical circumstances, the pure electron plasmas studied here typically have gyroradius $R_L \sim 50$ μm; therefore, electron cross-field movements are quite limited, except for the drifting motions of their guiding centers. Among the various cross-field guiding-center drift motions [12], the $\mathbf{E} \times \mathbf{B}$ drift with velocity $c\mathbf{E} \times \mathbf{B}/|\mathbf{B}|^2$ is dominant, since zeroth-order space charge field **E** is large, and magnetic field **B** is uniform and well aligned with the cylindrical axis.

When certain conditions are satisfied (see following discussions), an electron column can be treated as 2D-like, i.e., as a section of an infinitely long axially uniform column, and its (r, θ) fluid motion can be approximately described by the 2D $\mathbf{E} \times \mathbf{B}$ dynamics. Here, one substitutes the density of electrons with the density of their guiding centers, since the gyroradius is much smaller compared to the typical spatial scale of the dynamical structures; furthermore, all other non-$\mathbf{E} \times \mathbf{B}$ drift motions are assumed to be negligible. The dynamics of this $\mathbf{E} \times \mathbf{B}$ "guiding-center" fluid can be summarized by the drift-Poisson equations [44, 69]

$$\frac{\partial n}{\partial t} + \mathbf{v} \cdot \nabla n = 0\,, \quad \mathbf{v} = -\frac{c}{B_z}\nabla\phi \times \hat{\mathbf{z}}\,, \quad \nabla^2\phi = 4\pi e n\,, \tag{3.1}$$

where $n(r, \theta, t)$, $\mathbf{v}(r, \theta, t)$, and $\phi(r, \theta, t)$ are the 2D electron density, fluid velocity, and electrostatic potential respectively, with $-e$ being the electron charge.

3.2.1 Conditions of Applicability

The ideal 2D drift dynamics in Equation (3.1) is obviously a highly simplified description of the true 3D plasma system. It is a good approximation of the real dynamics only when the following conditions are satisfied:

(a) the background magnetic field is uniform and in good alignment with the axis of the conducting cylinders;

(b) the temporal and spatial scales of the gyromotion of individual particles are both much smaller than those of the fluid motion under consideration;

(c) the axial length of the column is large compared to the plasma Debye length λ_D, so end effects are relatively unimportant;

(d) the electron axial bounce frequency γ_b is much faster than the $\mathbf{E}\times\mathbf{B}$ drift motion in the (r,θ) plane;

(e) the time scale of the fluid motion under study is much shorter than the like-particle collision time and external transport time.

Here, conditions (a) and (b) ensure that the $\mathbf{E}\times\mathbf{B}$ guiding-center drift approximation is valid for the cross-field plasma fluid motion. In a typical experiment, B_z is about 500 G, with relative field errors less than 10^{-4}, providing a uniform axial background field; the gyrofrequency $w_c/2\pi$ is thus on the order of 1.5 GHz, and $R_L \sim 50\ \mu$m (for $T \simeq 1$ eV), making these two conditions well satisfied.

Conditions (c) and (d) are necessary in order to achieve two-dimensionality. The column axial lengths L_p are normally between 20 cm and 50 cm, while the plasma Debye length $\lambda_D = (k_B T/4\pi n e^2)^{\frac{1}{2}} \simeq 2.5$ mm; the average bounce frequency $\gamma_b = (\frac{k_B T}{m_e})^{\frac{1}{2}}/2L_p \sim 1$ MHz, whereas the bulk $\mathbf{E}\times\mathbf{B}$ rotation frequency is around 100kHz. Therefore electron columns are quite 2D-like under these typical conditions.

Finally, condition (e) is required in order to justify neglecting dissipation mechanisms. For these plasmas, the electron like-particle collision time τ_{ee} is longer than 10 ms and the external transport time scale is seconds, making the $\mathbf{E} \times \mathbf{B}$ drift dynamics basically nondissipative, except perhaps for columns with fine-scale distributions.

3.2.2 Analogy with Ideal 2D Fluid Dynamics

2D incompressible, homogeneous (uniform density and temperature) Newtonian fluids follow the Navier-Stokes equation in the (x,y) plane

$$\frac{d\mathbf{v}}{dt} = (\frac{\partial}{\partial t} + \mathbf{v} \cdot \nabla)\mathbf{v} = -\frac{1}{\rho_{\mathrm{m}}}\nabla P_{\mathrm{m}} + \nu_{\mathrm{m}}\nabla^2\mathbf{v}, \tag{3.2}$$

where d/dt is the material derivative along the trajectory of a fluid element with velocity $\mathbf{v}(x,y,t)$, ρ_{m} is the specific mass of the fluid, P_{m} is the pressure, and ν_{m} is the fluid molecular kinematic viscosity.

When the incompressibility condition $\nabla \cdot \mathbf{v} = 0$ is satisfied in 2D, the fluid velocity $\mathbf{v}$ can be rewritten in term of a scalar stream function $\Psi(x,y,t)$, with $\mathbf{v} \equiv \hat{\mathbf{z}} \times \nabla\Psi$. Consequently, at each moment, contours of the stream function correspond to the 2D flow stream lines [71]. The fluid vorticity $\zeta(x,y,t)$ is also a scalar in 2D, defined as $\zeta \equiv \hat{\mathbf{z}} \cdot \nabla \times \mathbf{v} = \nabla^2\Psi$. From Equation (3.2), the vorticity equation for the 2D fluid can be derived,

$$\frac{\partial\zeta}{\partial t} + \mathbf{v} \cdot \nabla\zeta = \nu_{\mathrm{m}}\nabla^2\zeta\,, \tag{3.3}$$

or

$$\frac{\partial(\nabla^2\Psi)}{\partial t} + (\hat{\mathbf{z}} \times \nabla\Psi) \cdot \nabla(\nabla^2\Psi) = \nu_{\mathrm{m}}\nabla^4\Psi\,.$$

Provided that the following sufficient conditions are met, the vorticity dynamics is the complete description of a 2D flow, i.e., once the distribution of the vorticity ζ is set, the stream function Ψ, velocity $\mathbf{v}$, and pressure P_{m} are all determined through the Green function of the system [82],

(i) the region occupied by the fluid is bounded and singly connected;

(ii) the normal component of the velocity is given at the boundary.

Note that conditions (i) and (ii) are generally satisfied in the electron column experiments under the 2D approximation, as shown later in the section.

In the inviscid limit, $\nu_m \simeq 0$, Equation (3.3) becomes the Euler equation,

$$\frac{\partial \zeta}{\partial t} + \mathbf{v} \cdot \nabla \zeta = 0 \,, \tag{3.4}$$

which describes the simple advection of fluid vorticity ζ along stream lines [82]. The convective velocity $\mathbf{v}$ is determined by the distribution of ζ and the boundary conditions.

Levy first pointed out that there exists a mathematical isomorphism between the nondissipative 2D $\mathbf{E} \times \mathbf{B}$ drift dynamics in non-neutral plasmas and the Euler equation that governs ideal 2D fluids [44]. As can be seen clearly from Equation (3.1), the fluid stream function Ψ is directly proportional to the electrostatic potential ϕ, with $\Psi = c\phi/B_z$; and the scalar vorticity ζ is directly proportional to the electron density n, with $\zeta = 4\pi ecn/B_z$. As shown in Figure 3.1, the motion of a magnetized electron column confined in a conducting cylinder with density distribution $n(r,\theta)$ is completely analogous to a uniform density fluid in a free-slipping cylindrical tank with the vorticity distribution $\zeta(r,\theta) = 4\pi ecn(r,\theta)/B_z$.

The significance of this analogy is two-fold: first, 2D fluid dynamics has been studied extensively over the past one hundred years, rendering many results directly applicable to the $\mathbf{E} \times \mathbf{B}$ drift dynamics; second, owing to the inherently low collisionality and high degree of two-dimensionality, magnetized electron columns are excellent test-beds for the study of the 2D Euler dynamics. In addition, the electron columns are easy to manipulate and can be measured with high degree of accuracy and resolution.

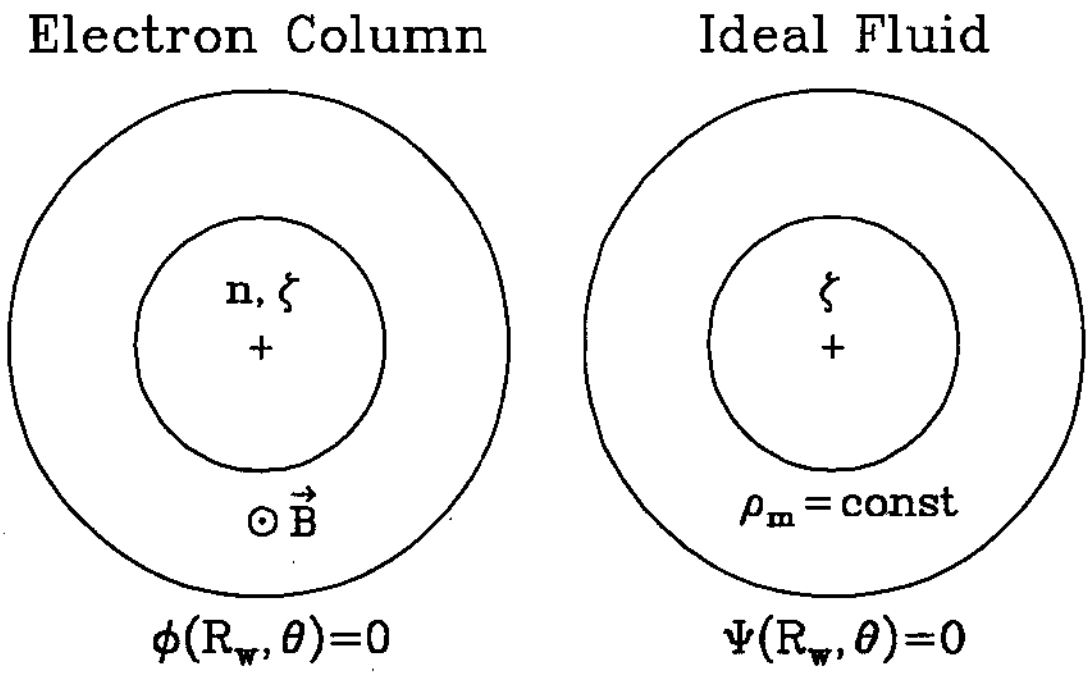

Figure 3.1: Analogy between electron $\mathbf{E} \times \mathbf{B}$ drift motion and ideal 2D fluid flows.

3.2.3 Boundary Condition

Boundary conditions are needed in order to fully describe the flow dynamics in the entire 2D domain. In the experiments performed for this thesis, there is no central conducting wire in the V′ machine, as is the case for some other non-neutral plasma devices [80]; consequently, the region occupied by an electron column is always bounded and singly connected, satisfying the vorticity completeness condition (i). Generally speaking, except for small portions being used as receivers and transmitters of waves, all the confinement cylinders are electrically grounded with $\phi(R_w, \theta) = 0$, ensuring that the 2D boundary is everywhere parallel to the equipotential (stream function) contour. This also implies that the $\mathbf{E} \times \mathbf{B}$ drift velocity does not have a normal component at wall, as a result, no electrons can $\mathbf{E} \times \mathbf{B}$ drift out of the confinement region under this boundary condition.

Other boundary conditions have been applied by Notte *et al.* to study the stationary density distribution in an asymmetric trap [67]. Here, sector probes extending over the entire column axial length are biased to electrostatic voltages up to 100 V, giving a piecewise equipotential boundary condition, which also satisfies the vorticity completeness condition (ii).

In conventional fluid experiments, there normally exists a complicated "viscous boundary layer" near the wall regions, due to the "no-slip" boundary condition where the fluid velocity must remain the same as that of the wall [71]. In Malmberg-Penning traps, electrons are normally far away from the cylinder wall at all times, so one can avoid considering the complex particle-wall interactions. Here, the flow velocity is well defined at the wall even when the electrons are absent, giving a true *free-slip* boundary.

3.2.4 Ideal 2D Invariants

Under the nondissipative 2D $\mathbf{E} \times \mathbf{B}$ drift dynamics, the following integrals (called ideal 2D invariants) are conserved:

- number of particles

$$N_L \equiv \int d^2\mathbf{x}\, n(\mathbf{x},t)\,,$$

- angular momentum

$$\mathcal{P}_\theta \equiv (\frac{eB_z R_w^2 N_L}{2c})\, P_\theta \equiv \frac{eB_z}{2c} \int d^2\mathbf{x}\, (R_w^2 - |\mathbf{x}|^2)\, n(\mathbf{x},t)\,,$$

- electrostatic energy

$$\mathcal{H}_\phi \equiv (e^2 N_L^2)\, H_\phi \equiv -\frac{e}{2} \int d^2\mathbf{x}\, \phi(\mathbf{x},t)\, n(\mathbf{x},t) = \frac{1}{8\pi} \int d^2\mathbf{x}\, |\mathbf{E}(\mathbf{x},t)|^2\,,$$

- mth moment of density

$$\mathcal{Z}_m \equiv [N_L^m / R_w^{2(m-1)}]\, Z_m \equiv \frac{1}{m} \int d^2\mathbf{x}\, [n(\mathbf{x},t)]^m\,, \quad m = 2,3,4,\ldots\,.$$

Here P_θ, H_ϕ, and Z_m represent the corresponding dimensionless invariants normalized by using R_w, B_z, and N_L. Since N_L is well-conserved in the experiments (see Appendix A), typically varying less than 2%, this choice of using N_L for normalizations is justified, and these dimensionless invariants will be used in the following chapters.

Let the dimensionless spatial coordinate be $\mathbf{r} \equiv \mathbf{x}/R_w$. One can define characteristic density and potential as $n_0 \equiv N_L/R_w^2$ and $\phi_0 \equiv eN_L$. Therefore, the dimensionless ideal invariants can rewritten as

$$\begin{aligned} P_\theta &= \int d^2\mathbf{r}\,(1-r^2)\,(\frac{n}{n_0})\,, \\ H_\phi &= -\frac{1}{2}\int d^2\mathbf{r}\,(\frac{\phi}{\phi_0})\,(\frac{n}{n_0})\,, \\ Z_m &= \frac{1}{m}\int d^2\mathbf{r}\,(\frac{n}{n_0})^m\,. \end{aligned}$$

Generally speaking, a global integral of any function of density n, $F \equiv \int d^2\mathbf{r}\, f(n)$ is also an ideal invariant. An important example is the dimensionless mean-field entropy $S \equiv -\int d^2\mathbf{r}\,(n/n_0)\,\ln(n/n_0)$, which is also conserved.

Employing the analogy to the 2D Euler flow discussed earlier, the following correspondence between ideal invariants of the $\mathbf{E}\times\mathbf{B}$ drift dynamics and those of the Euler dynamics can be listed:

$$\begin{aligned} N_L &\leftrightarrow \text{total circulation } \Gamma, \\ \mathcal{P}_\theta &\leftrightarrow \text{angular impulse } \mathcal{A}_z, \\ \mathcal{H}_\phi &\leftrightarrow \text{kinetic energy } \mathcal{E}, \\ \mathcal{Z}_m &\leftrightarrow m\text{th moment of vorticity;} \end{aligned}$$

in particular, $\mathcal{Z}_2$ corresponds to enstrophy $\Omega \equiv \frac{1}{2}\int d^2\mathbf{x}\,\zeta^2$.

As in any other physical systems, invariants of the evolution play an important role in the behavior of these 2D-like electron columns. When the evolution does not involve turbulent motions, these infinite number of invariants are strictly conserved, putting strong constraints on the possible cross-field motions.

3.2.5 Dissipation and 3D Effects

The ideal 2D $\mathbf{E} \times \mathbf{B}$ drift dynamics neglects the axial degree of freedom and the effect of dissipation. An electron column in the experimental situation is, of course, a three-dimensional object, and its 3D nature inevitably influences the dynamics to some degree. In addition, even though this system is highly inviscid at large scales, various kinds of dissipation still play a role in the turbulence energy and enstrophy balance, due to their enhanced effectiveness at the fine scales [95]. Current knowledge of these non-ideal effects is far from complete; here, I summarize some qualitative understandings that appear to be relatively sound.

Any non-ideal effects not included in Equation (3.1) can be treated as dissipation in a general sense. For example, the column internal transport to its 3D thermal equilibrium has been studied experimentally by Driscoll [22], and theoretically by Dubin and O'Neil [25]; they found that the dominant transport can be attributed to non-local, resonant 2D $\mathbf{E} \times \mathbf{B}$ "collisions", which arise due to the "granular" nature of the relatively low-density electron column. The time scale for this dissipation is typically on the order of 10^6 bulk rotations for a quiescent column [22].

Other microscopic dissipation mechanisms include finite-gyroradius effect [42], 3D particle collisions [37], and the external anomalous transport [50], etc. In addition, a systematic error associated with changes in column end shape can happen when there is significant amount of 2D density redistribution during the evolution of a column; for example, the end shape of a hollow column is relatively flat compared to that of a peaked column, resulting in an apparent deviation from the ideal 2D dynamics in the z-averaged density measurement. Finally, the finite ratio of bounce to rotation frequency $2\pi\gamma_b/\omega$ results in some 2D density "smearing", in that electrons with unequal parallel kinetic energies tend to drift at slightly different angular velocity due to column axial variations and end confinement voltages, causing density

to spread in the θ-direction [63, 74].

If one is concerned only with the fast $\mathbf{E} \times \mathbf{B}$ drift dynamics and large-scale phenomena, the effects of all these imperfections are generally quite small and can be safely neglected. One such example is the off-axis dynamical equilibrium state of large-amplitude $l = 1$ mode, which was treated successfully with the ideal 2D dynamics [31, 28].

In a turbulent flow where fine-scale motions are excited, however, these effects are presumably non-negligible, which tend to smooth out the fine-scale features quickly. Since these "viscous" effects are not well understood, it may seem doubtful that the turbulent phenomena in this system can be studied in any meaningful fashion; experimentally, however, this does not present any serious problems when the smallest scale the diagnostic can resolve is larger than the scale-length at which dissipation is important. This is because the influence on the large-scale dynamics by motions at the "dissipative scale" is quite weak [41], i.e., two columns, having identical large-scale but different fine-scale density distributions, will evolve to approximately the same large-scale distributions at later times, at least in the statistical sense. Physically, it reflects the fact that the column space charge $\mathbf{E}$ field is largely determined by the mean-field (large-scale) density distribution; in other words, the fine-scale structures are averaged out when Poisson equation is integrated to obtain the $\mathbf{E} \times \mathbf{B}$ drift velocity, limiting their influence on the large-scale flow.

In numerical simulations, to facilitate computations, investigators often use the so-called "hyper-viscosities", which artificially cause dissipation to appear as $(-1)^{p-1}\nu_p \nabla^{2p}\zeta$, $p = 2, 3, \ldots$, in Equation (3.3), instead of the physical molecular viscosity ν_{m} with $p = 1$; they have found that flows at large scales are nearly independent of the nature of viscosity as long as it is small compared to the inviscid interactions [56, 3]. Therefore, the existence of small but finite dissipation appears

to act only as a "drain" for the conserved quantities at the dissipative scale, and does not influence the large-scale dynamics. For this reason, these systems are referred to as "effectively inviscid" by Batchelor [4]. Experiments on relatively short electron columns in moderately high magnetic fields indicate that the fast $\mathbf{E} \times \mathbf{B}$ dynamics studied here is indeed effectively inviscid [19, 60].

3.3 General Properties of 2D Turbulence

The detailed dynamics of turbulence involves many degrees of freedom with disparate temporal and spatial scales, making it complicated and difficult to formulate [47]. Consequently, dynamical theories that have been proposed are generally, to certain degree, speculative and controversial in nature. Here, I only discuss some universal properties of 2D turbulence that either have been tested in experiments or numerical simulations, or are generally held to be true.

3.3.1 Robust and Fragile Invariants

During unforced turbulent evolutions characterized by the generation of fine-scale structures and strong mixing, some of the ideal invariants discussed in Section 3.2 can change significantly. These fragile invariants vary due to dissipation at fine scales and coarse-graining associated with the measurement processes. In contrast, other invariants are well conserved even in the presence of dissipation and coarse-graining, and these are called robust invariants.

In the absence of particle–wall interactions and field errors, N_L and $\mathcal{P}_\theta$ are robust invariants, since the internal dissipation does not affect the column particle number or total angular momentum [69]. In addition, electrostatic energy $\mathcal{H}_\phi$ is nearly conserved when the dissipation acts on fine scales and is small in magnitude [5]. This is apparently due to the weak dependence of potential ϕ on the fine-scale density distribution. The conclusion can be illustrated in the case of molecular

viscosity. Using the analogy with the 2D Euler flow, from Equation (3.3), one can derive the decay rate of the electrostatic energy $\mathcal{H}_\phi$,

$$\frac{d\mathcal{H}_\phi}{dt} = -8\pi e^2 \nu_{\rm m} \mathcal{Z}_2 \,. \tag{3.5}$$

Since $\mathcal{Z}_2$ is bounded, i.e., it can not go to infinity, the decay rate of energy approaches zero as viscosity $\nu_{\rm m}$ goes to zero.

Whenever the evolution creates fine-scale structures, the robust invariants are the only true invariants of the experimentally measured density distribution, since the coarse-graining effect of the finite-size collectors would still cause apparent dissipation even if the dynamics were ideal.

The higher moments of density $\mathcal{Z}_m$ and entropy $\mathcal{S}$ are all fragile invariants. Take $\mathcal{Z}_2$ as an example, its fragility can be understood by considering the case of molecular viscosity. From Equation (3.3), one gets

$$\frac{d\mathcal{Z}_2}{dt} = -\nu_{\rm m} \int d^2\mathbf{x} \, |\nabla n|^2 \,. \tag{3.6}$$

Since the density gradient ∇n is intensively amplified as a turbulent evolution proceeds, the integral on the right hand side of Equation (3.6) tends to increase to large values. As a result, even in the limit of small viscosity $\nu_{\rm m}$, the decay rate of the enstrophy can still be finite [5], causing enstrophy to decrease.

3.3.2 Transfer of Energy and Enstrophy in Spectral Space

Another way to understand the behavior of ideal invariants is to consider the spectral transfer of the two quadratic integrals: energy and enstrophy. Here, for simplicity, I use a periodic 2D square domain with unit area. The potential $\phi(\mathbf{x}, t)$ can be written in terms of its Fourier components,

$$\phi(\mathbf{x}, t) = \sum_{\mathbf{k}} \phi_{\mathbf{k}}(t) \exp(i\mathbf{k} \cdot \mathbf{x}) \,,$$

where

$$\phi_{\mathbf{k}}(t) \equiv \int d^2\mathbf{x}\, \phi(\mathbf{x},t) \exp(-i\mathbf{k}\cdot\mathbf{x})\,.$$

The energy and enstrophy can then be written as sums of all the contributions in Fourier spectral space,

$$\mathcal{H}_\phi(t) = \sum_{\mathbf{k}} \mathcal{H}_{\phi\mathbf{k}}(t) \propto \sum_{\mathbf{k}} |\mathbf{k}|^2 |\phi_{\mathbf{k}}(t)|^2\,, \tag{3.7}$$

$$\mathcal{Z}_2(t) = \sum_{\mathbf{k}} \mathcal{Z}_{2\mathbf{k}}(t) \propto \sum_{\mathbf{k}} |\mathbf{k}|^4 |\phi_{\mathbf{k}}(t)|^2\,, \tag{3.8}$$

where components of energy and enstrophy for wavenumber $\mathbf{k}$ are related by

$$\mathcal{Z}_{2\mathbf{k}}(t) \propto |\mathbf{k}|^2 \mathcal{H}_{\phi\mathbf{k}}(t)\,. \tag{3.9}$$

Generally speaking, when a flow is turbulent, distributions of energy and enstrophy among various scales in spectral space are being dynamically altered by the intense nonlinear couplings. By examining the energy and enstrophy balance for elementary triad interactions in 2D turbulent flows, Kraichnan demonstrated that statistically speaking there is a net transfer of energy from fine scales to large scales; in contrast, the net transfer of enstrophy is from large scales to fine scales [39]. This nonlinear coupling between different spatial scales is crucial for determining the robustness of the ideal invariants. Normally, appreciable dissipation occur only at fine scales, the fact that net energy transfer is from fine scales to large scales verifies that energy is indeed a robust invariant during a turbulent evolution; whereas significant amount of enstrophy decays away apparently due to the spectral enstrophy transfer from large scales to fine scales.

3.3.3 Reynolds Decomposition of Turbulent Flows

The idea that a turbulent flow can be theoretically decomposed into a slowly varying mean flow and rapidly changing random fluctuations may be traced back to da Vinci, before Reynolds put forward a rigorous definition (see [47] and references

therein). The mean flow can be regarded as the average over the fast time scales, whereas the fluctuating part is the instantaneous deviation from the mean flow.

For turbulent electron columns confined in conducting cylinders, the mean flow can be taken as the time-average over the column rotation period, which is approximately equivalent to the θ-average, as represented by the symbol $<>$. The instantaneous turbulent flow can therefore be decomposed as the following,

$$\begin{cases} n(r,\theta,t) = < n(r,t) > + \tilde{n}(r,\theta,t) \\ \mathbf{v}(r,\theta,t) = \omega(r,t) r \hat{\boldsymbol{\theta}} + \tilde{\mathbf{v}}(r,\theta,t) \\ \phi(r,\theta,t) = < \phi(r,t) > + \tilde{\phi}(r,\theta,t)\,, \end{cases} \tag{3.10}$$

where the mean flow is assumed to be axisymmetric and slow-varying, with the mean angular velocity $\omega(r,t)$ satisfying the relation

$$\omega(r,t) = \frac{4\pi e c}{B_z r^2} \int_0^r dr'\, r' < n(r',t) > \ . \tag{3.11}$$

From Equation (3.1), the dynamics of the mean flow and fluctuations can be summarized as the following coupled equations,

$$\frac{\partial < n >}{\partial t} + \frac{\partial < \tilde{v}_r \tilde{n} >}{\partial r} = 0\,, \tag{3.12}$$

$$\frac{d\tilde{n}}{dt} = (\frac{\partial}{\partial t} + \omega \frac{\partial}{\partial \theta} + \tilde{\mathbf{v}} \cdot \nabla)\tilde{n} = -(\frac{\partial}{\partial t} + \tilde{v}_r \frac{\partial}{\partial r}) < n >\,, \tag{3.13}$$

with

$$\tilde{\mathbf{v}} = \frac{c}{B_z} \hat{\mathbf{z}} \times \nabla \tilde{\phi}\,, \quad \nabla^2 \tilde{\phi} = 4\pi e \tilde{n}\,. \tag{3.14}$$

In this view of the turbulent flow, the axisymmetric background is changed gradually by the flux $< \tilde{v}_r \tilde{n} >$ due to the fluctuations. The fluctuating component is not axisymmetric in general, and its evolution is determined by the nonlinear convective coupling, $(\omega \frac{\partial}{\partial \theta} + \tilde{\mathbf{v}} \cdot \nabla)\tilde{n}$, and the source term due to the interaction with the vorticity of the mean flow, $-(\frac{\partial}{\partial t} + \tilde{v}_r \frac{\partial}{\partial r}) < n >$. These equations lay the foundation for further developments of theories on dynamics in cylindrical geometry,

e.g., the passive tracer model neglects the effects of the fluctuating velocity $\tilde{\mathbf{v}}$, leading to a simple equation:

$$[\frac{\partial}{\partial t} + \omega(r)\frac{\partial}{\partial \theta}]\tilde{n} = 0 \,.$$

Furthermore, it is often convenient to express the fluctuating density $\tilde{n}(r,\theta,t)$ in terms of its azimuthal Fourier components,

$$\tilde{n}(r,\theta,t) = \sum_{l=0}^{\infty} \tilde{n}^{(l)}(r,t)\exp(il\theta)\,, \tag{3.15}$$

with the understanding that whenever the equations are complex, the physical density is the real part of the expressions. The complex Fourier component $\tilde{n}^{(l)}(r,t)$ is

$$\tilde{n}^{(l)}(r,t) = \frac{1}{2\pi}\int_0^{2\pi} d\theta'\, \tilde{n}(r,\theta',t)\exp(-il\theta')\,.$$

This is especially convenient when dealing with normal modes of the electron column.

3.3.4 Coherent Structures in Decaying 2D Turbulence

Earlier theories of 2D turbulence have mainly concentrated on the spectral analysis of the flow field, where the phase information of Fourier modes are generally assumed to be unimportant [41]. However, more recent numerical simulations [56, 6, 7, 84] and some laboratory experiments [81, 13, 93] have demonstrated that the so-called "coherent structures" play a dominant role in the decaying 2D turbulence. These structures are spatially localized, robust blobs of vorticity (vortices) co-existing with seemingly structureless turbulent background; the late-time dynamics of turbulent relaxation can often be characterized by the mutual interactions between these coherent vortices [11, 55].

Furthermore, as part of the effort to understand the giant vortices in outer planets, investigations have shown that coherent vortices can also exist prominently in shearing flows [52, 90, 53]. Here, the mean shearing background breaks the sign

symmetry of the coherent vortices, and only those vortices that rotate in the same sense as the background shear (prograde vortices) can survive in the mean flow.

The dominance of these coherent structures indicates that the phase information of the Fourier modes is crucial to the understanding of 2D turbulence [2, 3, 57], and that the elementary excitations of the flow are these coherent vortices existing in real space, rather than the Fourier modes in spectral space.

3.4 Diagnosing 2D Turbulence

3.4.1 Collector Measurement and Coarse-Graining Effect

As described in Chapter 2, 2D density distributions can be measured at ten different locations for a single-shot using the endplate collector assembly. The diameter $2R_{\mathrm{C0}}$ of the nine fixed collectors is 0.40 cm; whereas the diameter $2R_{\mathrm{Cr}}$ of the mobile collector Cr is 0.20 cm, and it can be placed at any radial position along $\theta \simeq 0°$.

The collector density measurement can be easily calibrated, and has the advantages of being fast, accurate, and reliable. When used to measure turbulent distributions, the main limitation of these collectors is their finite spatial resolution. Since the measured charge is necessarily the spatial average over the cross section of a collector, one can not resolve density structures that are smaller than the size of the collector. Therefore, measuring a physical 2D turbulent flow using these collectors is similar to seeing a picture through a slightly unfocused camera. This convolution effect by the finite-size collectors is commonly referred to as "coarse-graining".

One can study this coarse-graining effect on a more quantitative level. Let's again consider the periodic 2D square domain with unit area (this is justified on the ground that coarse-graining only affects scale-lengths much smaller than the cylinder radius); here, $n(\mathbf{x}) = \sum n_{\mathbf{k}} \exp(i\mathbf{k} \cdot \mathbf{x})$ is the real density distribution being

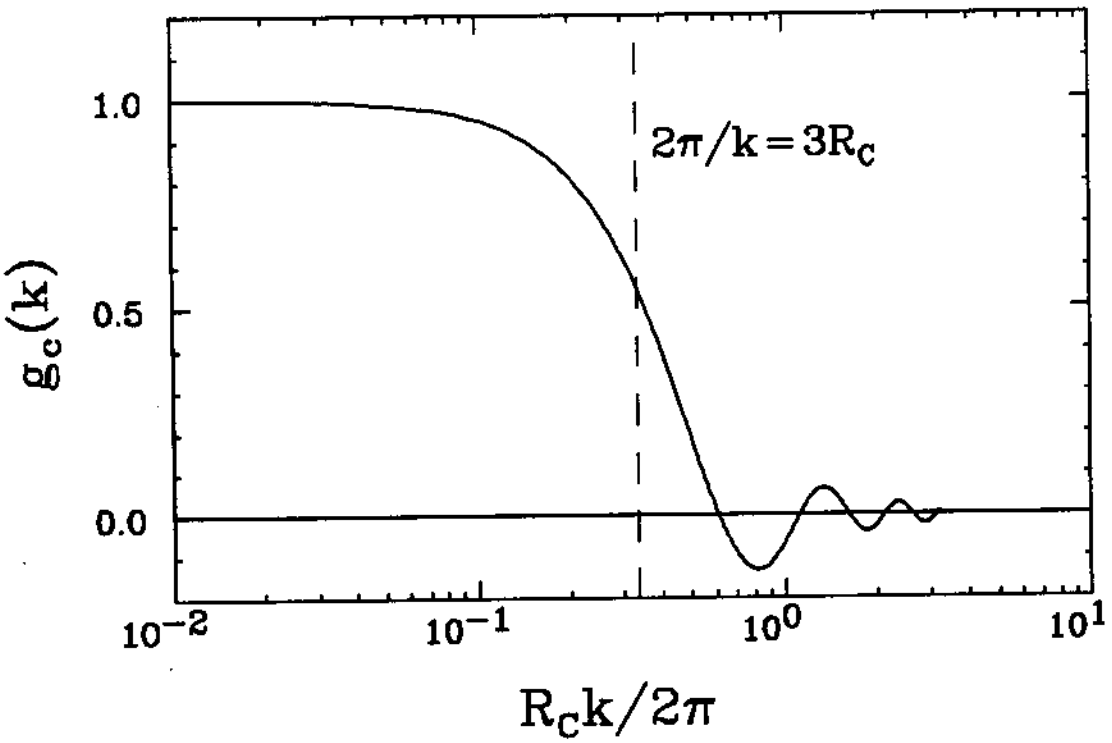

Figure 3.2: Collector coarse-graining effect on Fourier component $\mathbf{k}$ with 2D wavenumber amplitude k.

measured, where $n_{\mathbf{k}}$ is the Fourier transform of $n(\mathbf{x})$. The measured density n_c as seen by a circular collector centered at $\mathbf{x}$ with diameter $2R_C$ is (see Appendix D)

$$\begin{aligned} n_c(\mathbf{x}) &= \frac{1}{\pi R_C^2}\int_C d^2\mathbf{x}'\, n(\mathbf{x}+\mathbf{x}') \\ &= \sum_{\mathbf{k}} n_{\mathbf{k}} \exp(i\mathbf{k}\cdot\mathbf{x}) \frac{1}{\pi R_C^2}\int_0^{R_C} d|\mathbf{x}'|\,|\mathbf{x}'| \int_0^{2\pi} d\theta'\, \exp(i\mathbf{k}\cdot\mathbf{x}') \\ &= \sum_{\mathbf{k}} n_{\mathbf{k}} \exp(i\mathbf{k}\cdot\mathbf{x}) [\frac{2J_1(R_C|\mathbf{k}|)}{R_C|\mathbf{k}|}] \,. \end{aligned} \tag{3.16}$$

Thus, the attenuation factor for the Fourier component with wavenumber amplitude $k \equiv |\mathbf{k}|$ is

$$g_c(k) = \frac{2J_1(R_C k)}{R_C k} \,. \tag{3.17}$$

This attenuation factor $g_c(k)$ is plotted as a function of $(R_C k/2\pi)$ in Figure 3.2. As expected from physical intuition, for large-scale components (wavelength $2\pi/k \gg R_C$), the measurement of density is not affected by the collector radius R_C; whereas for fine-scale components (wavelength $2\pi/k \ll R_C$), the collector averages out most of their contributions to the measured density. In essence, the collector acts like a "low-pass" filter for the spatial scales of the 2D density distribution, with sensitivity of 50% for structures with wavelength $\simeq 3R_C$.

3.4.2 Single-Shot Imaging

The phosphor screen/CCD camera diagnostic allows 2D density imaging of a single shot with high spatial resolution (up to 512×512 pixels). This diagnostic is still in the trial stage, and many subtle aspects, such as accurate calibration, image distortion due to high voltage axial acceleration, and light diffusion in the optical system have yet to be fully understood. Nonetheless, the ability to obtain single-shot images of column 2D density distribution represents a great improvement over the traditional collector (Faraday cup) diagnostic.

Due to the fact that the density diagnostics in Malmberg-Penning traps are inherently destructive, many essentially identical plasmas must be created in order to study the temporal evolution of dynamical processes. For evolutions that are non-chaotic and highly repeatable in experiments, the camera setup is an excellent 2D density diagnostic, containing all the information of the dynamics. For chaotic or turbulent evolutions, however, one still has to resort to statistical analyses, since the detailed dynamics of these processes are sensitive to arbitrarily small variations in the initial conditions. Each particular image of the evolution is then just a sample out of many possible dynamical states.

3.4.3 Experimental Ensembles for Statistical Averaging

Devising an experimental ensemble to perform statistical analyses requires some explanations, since the meaning of ensemble averaging can be easily misinterpretted. The assumptions built into the theoretical ensemble described in Section 3.3 are not always automatically met in the experiments, so careful selection of ensemble for statistical averaging is needed.

In Chapter 2, I described the experimental techniques used in the preparation of initial electron hollow columns. These columns are very reproducible experimentally, with shot-to-shot variations typically less than 0.5%, and have roughly axisymmetric density distribution. Unstable diocotron modes will grow, resulting in the onset of turbulence.

One simple statistical ensemble is to use all the shots measured at the time t of the evolution. If the instabilities arise predominantly from random noise in columns, this choice will satisfy the assumptions made in the theoretical Reynolds decomposition of the mean flow and fluctuations. In the experiments, however, I found that the instabilities generally grow out of reproducible asymmetric perturbations created by the ejection process, rather than from random noise. Consequently, the growing instabilities are initially phase locked with respect to $t = 0$.

Figure 3.3 shows such an example of density versus time at radius $R = 0.5$cm, $\theta = 0$ and $\theta = 180°$, during the early growth of the unstable $l = 1$ diocotron mode in a 20 cm long hollow column. The density evolution is constructed from many shots, which clearly shows growing phase-locked oscillations (out of phase between $\theta = 0$ and $\theta = 180°$), indicating that the mode is growing out of the same seeded asymmetries created by the ejection process from shot-to-shot. The frequency of the density oscillations is about 72 kHz, in correspondence with the sector probe measurement of the unstable $l = 1$ mode.

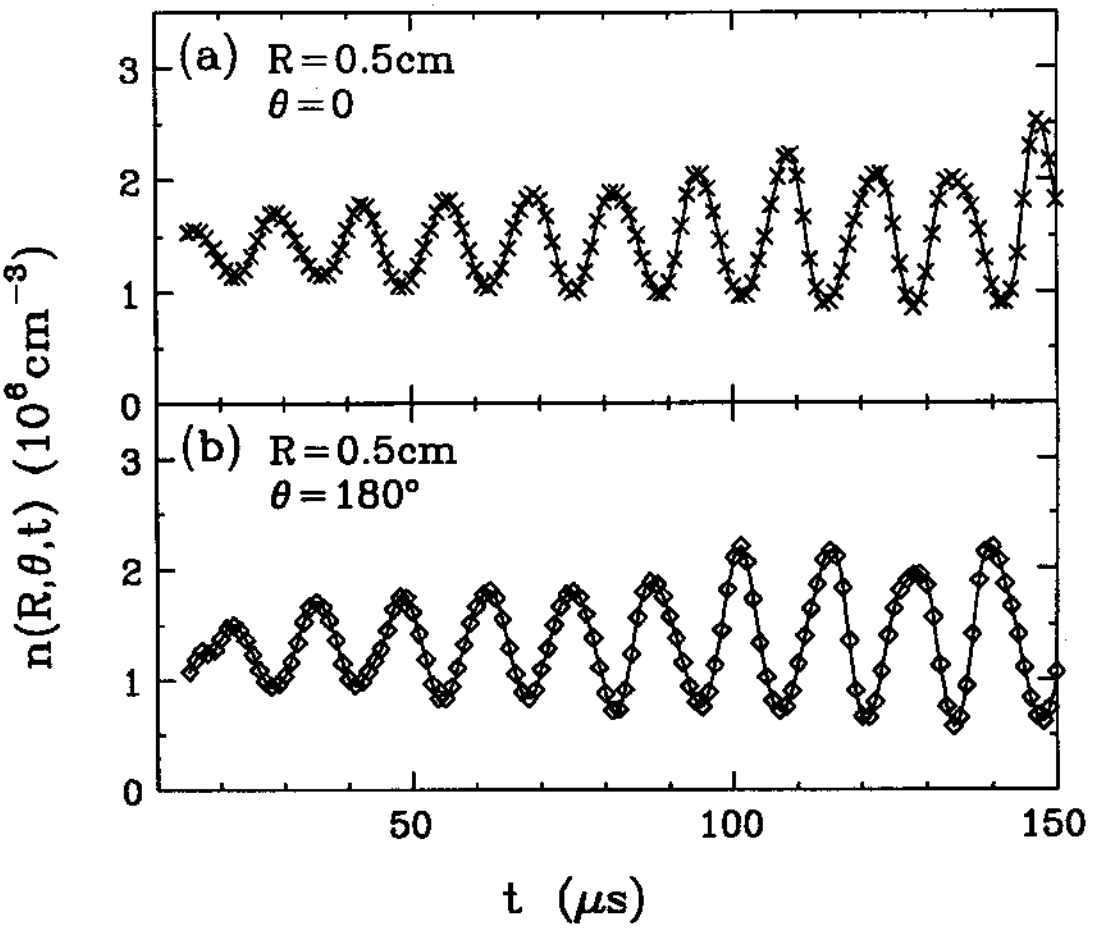

Figure 3.3: Density versus time showing the initial growth of the unstable $l = 1$ mode. (a) At $R = 0.5$ cm, $\theta = 0$, (on C1); (b) at $R = 0.5$ cm, $\theta = 180°$, (on Cr).

To construct an ensemble that allows for meaningful Reynolds decomposition as discussed in Section 3.3, I devise another statistical ensemble that randomly varies the dump time within one period of the dominant unstable mode. Here, one first finds out the frequency of this primary unstable mode through measurements like those shown in Figure 3.3, then a variable-time trigger generator is utilized to vary the dump time randomly within l times the period of this mode (normally $\leq 20\,\mu$s). This effectively scrambles the phase of the dominant unstable mode during the early stage of the mode growth. In this case, the evolution time t is designated as the dump time for the halfway point of this period.

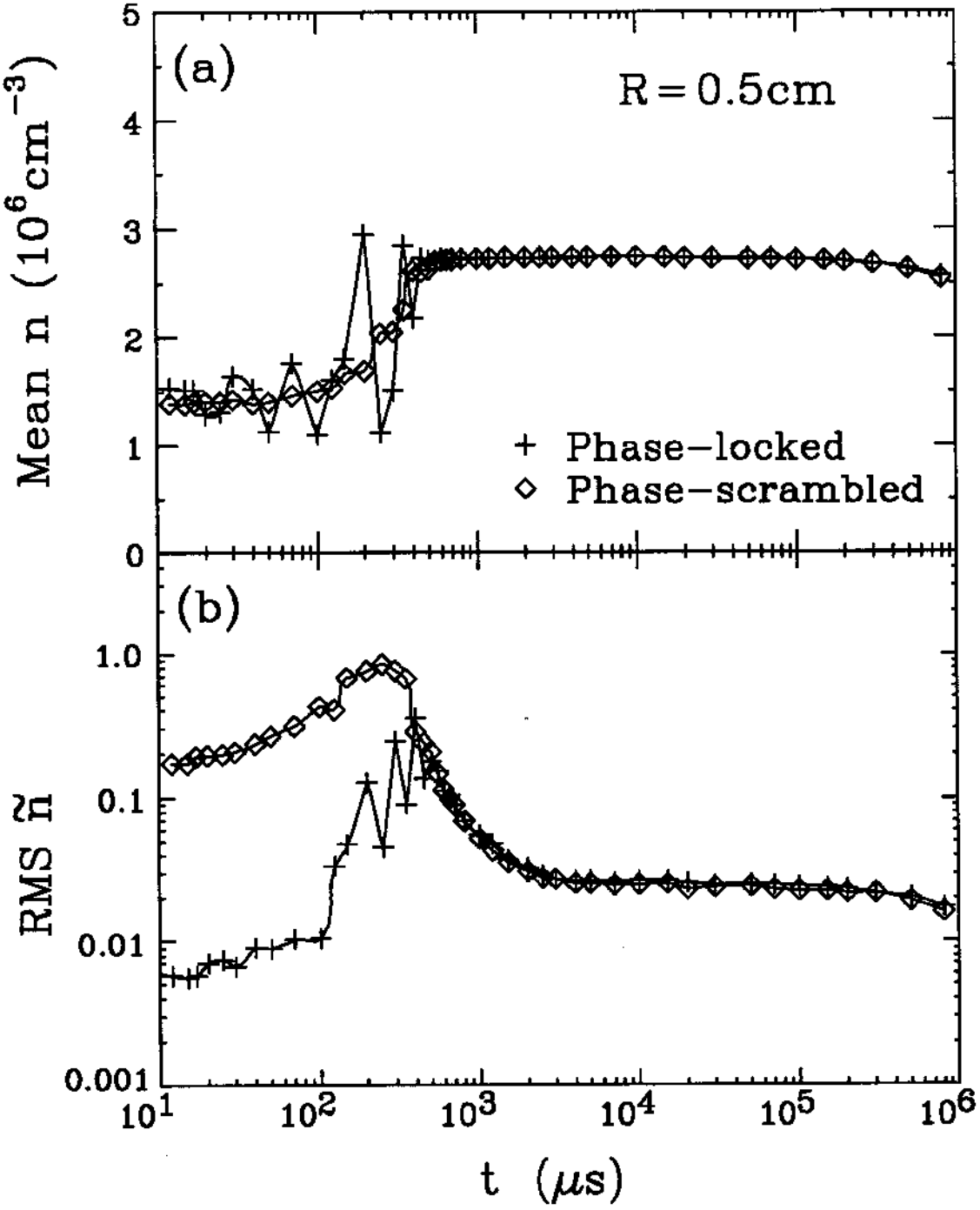

Figure 3.4: Comparison between the phase-locked and phase-scrambled averaging. (a) Mean density at $R = 0.5$ cm; (b) RMS fluctuation level at $R = 0.5$ cm.

Figure 3.4 shows the comparison of these two averages used to measure the mean density and RMS (Root-Mean-Square) density fluctuation level (at $R = 0.5$cm) of the same hollow column evolution. At early times, the phase-locked average yields an oscillating mean density and small shot-to-shot RMS fluctuations, reflecting the good shot-to-shot reproducibility of the initial hollow column. As expected, the phase-scrambled average smoothes out the fast oscillations and gives a much higher fluctuation level, which is simply $1/\sqrt{2}$ times the amplitude of the unstable mode. This unstable mode continues to grow, and soon saturates to form nonlinear vortices, causing rapid convective inward transport, which establishes a monotonically decreasing mean radial profile and stabilizes the column (see Chapter 4). After the radial transport, these two averages give essentially identically results, presumably because all the initial phase information is lost at late times of the evolution.

The main emphasis of this thesis is on the turbulent relaxation of these columns after the establishment of the mean radial profiles, so the two averages are generally interchangeable. Without being specified otherwise, I normally use this phase-scrambled average as the experimental ensemble, represented by the symbol $<>$, to perform statistical analyses.

3.4.4 Fluctuations and Correlations

It is necessary to distinguish between the density readings measured on different plasma shots when the amplitude of the shot-to-shot fluctuations is large. At time t of the evolution and for shot i, the density measured by collector Cj positioned at (r_j, θ_j) is designated as $n_i(r_j, \theta_j, t)$. Let N_s be the total number of shots measured, one-point quantities as functions of time and location can be calculated as the following:

- Mean density

$$< n(r_j, t) > \equiv \frac{1}{N_s} \sum_{i=1}^{N_s} n_i(r_j, \theta_j, t) \,,$$

- Fluctuation level

$$< \tilde{n}(r_j, t) >_{\rm rms} \equiv \{ \frac{1}{N_s - 1} \sum_{i=1}^{N_s} [n_i(r_j, \theta_j, t) - < n(r_j, t) >]^2 \}^{\frac{1}{2}} \,,$$

- Skewness

$$S_k(r_j, t) \equiv \frac{\frac{1}{N_s - 1} \sum_{i=1}^{N_s} [\tilde{n}_i(r_j, \theta_j, t)]^3}{< \tilde{n}(r_j, t) >^3_{\rm rms}} \,,$$

- Kurtosis

$$K_u(r_j, t) \equiv \frac{\frac{1}{N_s - 1} \sum_{i=1}^{N_s} [\tilde{n}_i(r_j, \theta_j, t)]^4}{< \tilde{n}(r_j, t) >^4_{\rm rms}} \,,$$

where $\tilde{n}_i(r_j, \theta_j, t) \equiv n_i(r_j, \theta_j, t) - < n(r_j, t) >$ is the density fluctuation. Futhermore, all the measured one-point statistical information on Cj is contained in the probability distribution function (PDF) $\rho(n', r_j, t)$, where $\rho \, dn'$ is the statistical probability for the measured density n_i to appear in the density range $n' \rightarrow n' + dn'$.

Two-point correlation functions of the density fluctuations contain information about the scale-lengths of the fluctuations in various directions. They are defined as

$$C_{jk} \equiv \frac{\frac{1}{N_s - 1} \sum_{i=1}^{N_s} \tilde{n}_i(r_j, \theta_j, t) \, \tilde{n}_i(r_k, \theta_k, t)}{< \tilde{n}(r_j, t) >_{\rm rms} < \tilde{n}(r_k, t) >_{\rm rms}} \,,$$

where indices j, k represent collector Cj and Ck (or pixel j, k) at two different locations (r_j, θ_j) and (r_k, θ_k), with j, k = r, 0, 1, 2, 2^+, 2^*, 2^-, 3, 4, 5. Note that the position of the mobile collector Cr is simply (r, θ).

According to Equation (3.15), the measured density fluctuation $\tilde{n}$ can be written in terms of its azimuthal Fourier components,

$$\tilde{n}(r, \theta, t) = \sum_{l=0}^{\infty} \tilde{n}^{(l)}(r, t) \exp(il\theta) \,;$$

therefore, ensemble-averaged quantities are related to the Fourier component $\tilde{n}^{(l)}(r,t)$; e.g., the fluctuation level is

$$<\tilde{n}(r,t)>_{\rm rms}= \frac{1}{\sqrt{2}}[\sum_{l=0}^{\infty} < |\tilde{n}^{(l)}(r,t)|^2 >]^{\frac{1}{2}} , \tag{3.18}$$

and the correlation function is

$$C_{jr}(r,\theta,t) = \frac{\sum_{l=0}^{\infty} < \tilde{n}^{(l)}(r,t)\, \tilde{n}^{(l)*}(r_j,t) > \exp[\, il(\theta-\theta_j)\,]}{[\sum_{l=0}^{\infty} < |\tilde{n}^{(l)}(r,t)|^2 > \sum_{l=0}^{\infty} < |\tilde{n}^{(l)}(r_j,t)|^2 >]^{\frac{1}{2}}} , \tag{3.19}$$

where component $\tilde{n}^{(l)*}$ is the complex conjugate of $\tilde{n}^{(l)}$.

The ensemble-average measurement method can be tested on columns with known fluctuations, such as a single stable diocotron wave with mode number l,

$$\tilde{n}(r,\theta,t) = \sqrt{2}\, <\tilde{n}(r)>_{\rm rms}\, \exp\{\, i[l\theta - \omega_l t + \varphi_l(r)]\,\} ,$$

where $\varphi_l(r)$ is the phase of mode l. Here, the two-point correlation functions are particularly simple,

$$C_{jr}(r,\theta) = \exp\{\, i[l(\theta-\theta_j) + \varphi_l(r) - \varphi_l(r_j)]\,\} , \tag{3.20}$$

where (r_j,θ_j) is the position of the fixed collector Cj.

Figure 3.5 shows the ensemble-average measurement using the phase-scrambled ensemble on a column with a $l=1$ stable mode. Plotted in Figure 3.5(a) and (b) are radial profiles of the mean density and fluctuation level respectively. The solid curve in Figure 3.5(b) is the prediction by the linear theory of diocotron modes [44, 45, 19], $<\tilde{n}(r)>_{\rm rms} \propto -d<n(r)>/dr$, where the overall amplitude is obtained by fitting at $R \simeq 1.3$ cm, the point of steepest mean-density gradient. The measured fluctuation level basically agrees with the linear theory.

The correlation functions C_{2r} and C_{2-r} are shown in Figure 3.5(c) and (d), where the vertical dashed lines mark the locations of the fixed collector C2 ($\theta_2 = 0$) and C2$^-$ ($\theta_{2-} = -90°$). For the stable $l=1$ diocotron mode, phase $\varphi_1(r) = 0$ for all

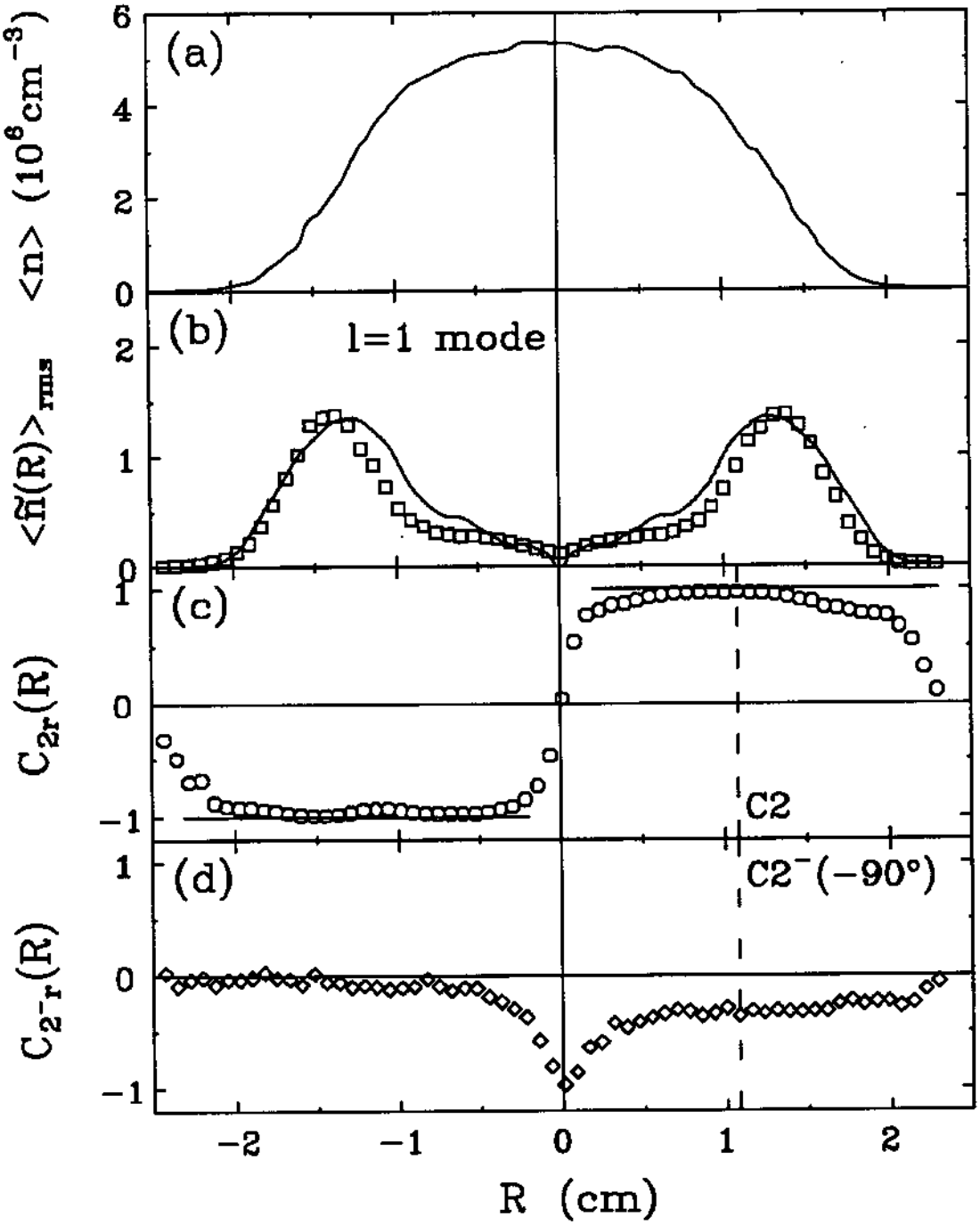

Figure 3.5: Ensemble averages of a stable column with $l = 1$ diocotron mode. (a) Mean density; (b) fluctuation level; (c) correlation function C_{2r}; (d) C_{2-r}. Solid curves in (b) & (d) are the theoretical predictions.

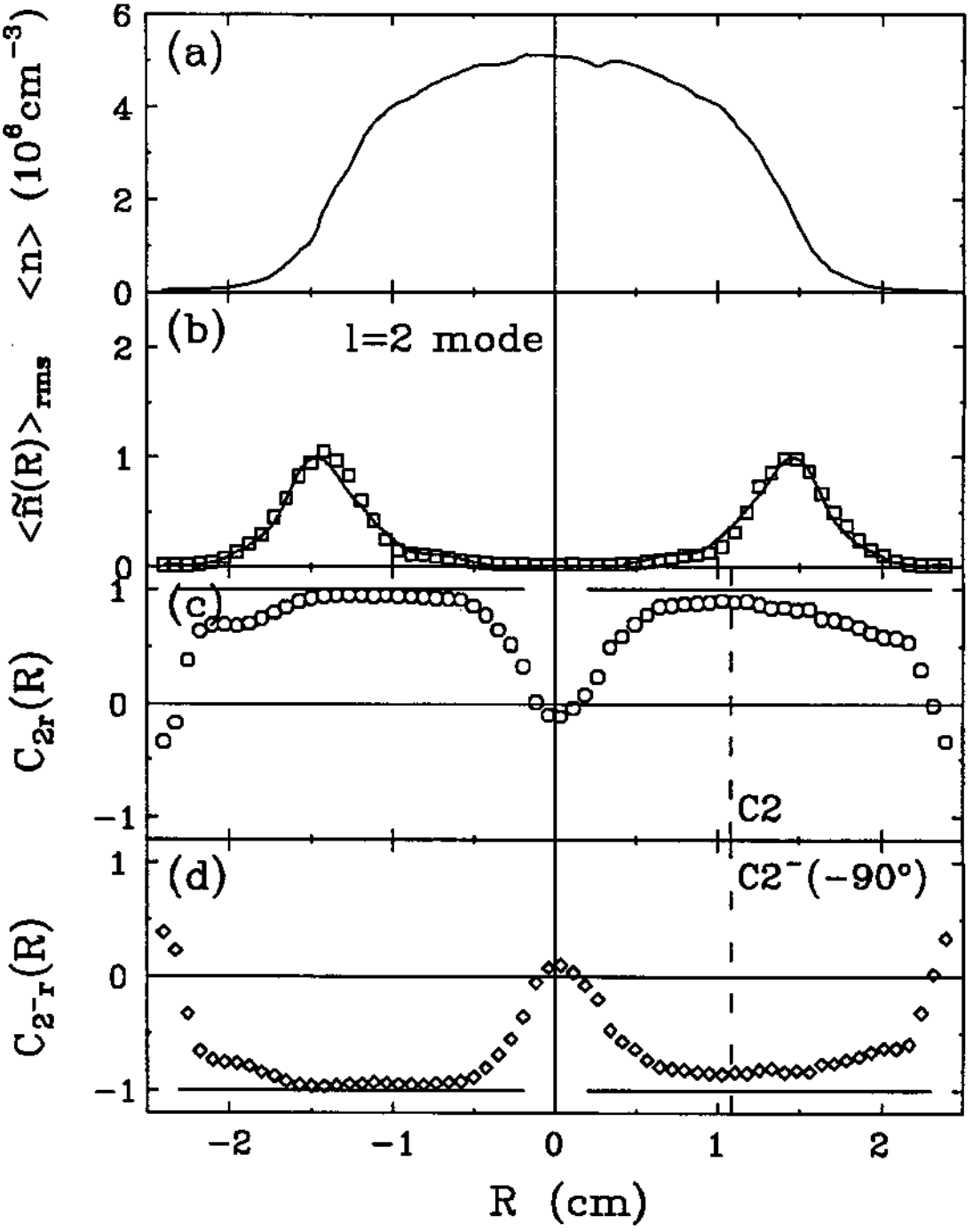

Figure 3.6: Ensemble averages of a stable column with $l = 2$ diocotron mode. (a) Mean density; (b) fluctuation level; (c) correlation function C_{2r}; (d) C_{2-r}. Solid curves in (b)–(d) are the theoretical predictions.

radii; therefore, from Equation (3.20), one has

$$C_{jr}(\theta) = \exp[i(\theta - \theta_j)] ,$$

where $\theta = 0$ or $180°$ for the mobile collector Cr. For C_{2r}, the prediction is plotted as the horizontal lines in Figure 3.5(c), and is verified by the measurement; For C_{2-r}, theory predicts a zero correlation for all radii, while the measurement has a 30% discrepancy for $\theta = 0$, which is apparently caused by the slight misalignment between the center of the column and that of the endplate.

The same ensemble-average measurement is also carried out for the stable $l = 2$ mode, as shown in Figure 3.6. In this case, the linear theory predicts that the fluctuation level satisfies $<\tilde{n}(r)>_{\rm rms} \propto -r\, d<n(r)>/dr$ [19], which agrees quite well with the data shown in Figure 3.6(b); in addition, from Equation (3.20) and using $\varphi_2(r) = 0$, the correlation functions take the form

$$C_{jr}(\theta) = \exp[\, i2(\theta - \theta_j)\,] ,$$

and is essentially confirmed by the measurement shown in Figure 3.6(c) and (d). Note that here, $C_{2r}(r)$ and $C_{2-r}(r)$ both go to zero at origin, for the reason that the measured fluctuation level at $R \simeq 0$ is dominated by random noise, since the mode eigenfunction is close to zero.

Chapter 4

Measurements of 2D Turbulent Relaxation

4.1 Overview

Experimental measurements on the free relaxation process of 2D $\mathbf{E} \times \mathbf{B}$ drift turbulence in magnetized electron columns are presented and discussed in this chapter. Starting from a hollow density distribution, the turbulence arises as a result of diocotron instabilities and subsequent nonlinear vortex interactions, and then relaxes after the convective inward transport establishes a globally stable, albeit turbulent column.

Section 4.2 describes the characteristics of the overall plasma column evolution, which consists of early unstable mode growth and saturation, turbulence and relaxation, meta-equilibrium, and 3D "viscous" particle transport. These features are illustrated by measurements from both the single-shot CCD camera images and the ensemble averages. Correlation measurements on the initial hollow column with a growing unstable mode and on the turbulent column are examined, complementing the direct observations from the CCD images.

In Section 4.3, the 2D turbulent relaxation process is studied in detail. I find that the entire relaxation lasts several hundred column bulk rotations, and can be roughly divided into three phases: Phase I is characterized by the rapid filamenta-

tion and mixing of turbulent density clumps (electron surpluses) and shallow holes (deficiencies) in the shearing background rotation; Phase II is dominated by the remaining elongated medium-size holes, which are prograde and thus can survive the background shear, and are settling into symmetric configurations through mutual interactions such as occasional merger; in Phase III, these coherent holes slowly drift radially outward and are finally axisymmetrized with respect to the column center, bringing forth the meta-equilibrium state of the 2D relaxation.

As a result of the longevity of these deep density holes, the observed noise decay time is 10–50 times slower than that of a simple "passive tracer" mixing. The survivability of the individual holes is quantitatively understood using the Moore-Saffman model based on the equilibration of an elliptical vorticity patch in a background flow with a uniform simple shear. The tendency for the holes to settle into symmetric configurations in the column are explained by physically intuitive stability arguments on the hole–hole and hole–shear interactions. The decline of the fluctuation level at late times, which apparently reflects the outward drift of the density holes, can be approximated with an exponential decay. The dependences of the e-folding decay rate on the radial position, on the column axial length, and on the magnetic field are found to be weak; this consistent with the 2D $\mathbf{E} \times \mathbf{B}$ dynamics.

4.2 Characteristics of the Overall Evolution

General characteristics of the overall evolution of the initially hollow electron columns are discussed in this section, for the purpose of providing background information for discussions on the turbulent relaxation period of the evolution. Two plasma columns are used to illustrate these characteristics: the $l = 1$ sequence has a relatively deep initial hollow profile ($n_{\max}/n(r = 0) \simeq 3.7$) and large column radius ($R_p \simeq 2.2$ cm, $L_p = 20$ cm, and $B_z = 507$ G), dominated by the $l = 1$ dio-

cotron instability at early times; the $l = 2$ sequence has a shallower initial profile ($n_{\max}/n(r=0) \simeq 1.5$) with smaller radius ($R_p \simeq 1.6$ cm, $L_p = 46$ cm, $B_z = 422$ G), dominated by the $l = 2$ diocotron instability.

A series of CCD camera images of the density $n(r, \theta, t)$ are displayed as false-color contour plots in Figure 4.1, showing the evolution dominated by the $l = 2$ instability. Here, the initial hollow column is seeded with a $l = 2$ perturbation by exciting stable $l = 2$ mode (see Section 3.4) prior to the column hollowing, resulting in an evolution initially driven by the $l = 2$ diocotron instability. Note that in this case, no external damping is applied to the column after the creation of the initial condition, so the slightly damped stable $l = 2$ mode co-exists with the growing unstable $l = 2$ mode and the turbulent fluctuations [16, 19].

At $t = 30\ \mu$s, the unstable $l = 2$ diocotron mode has grown to a moderate amplitude, and two large-size density blobs start to form as the mode approaches its nonlinear saturation. After orbitting around for several rotations, these two blobs begin to merge near the column center ($t = 145\,\mu$s). The merger convectively transports electrons from outer radii to the column center, thus establishes a monotonically decreasing mean radial profile, which is globally stable. By $t = 230\,\mu$s, the merger event has basically completed, while turbulent structures, such as filaments and vortices, have been generated in the column.

Following the formation of the column mean profile, these turbulent fluctuations start to decay by going through three distinct phases of relaxation ($t = 230\,\mu$s – 5 ms), which are discussed in detail in Section 4.3. At $t = 5$ ms, this 2D relaxation process is essentially finished, with the column being completely axisymmetrized. This meta-equilibrium column will be analyzed in Chapter 5, where I will show that the measured meta-equilibrium state is well predicted by the minimum enstrophy vortex resulting from "selective decay".

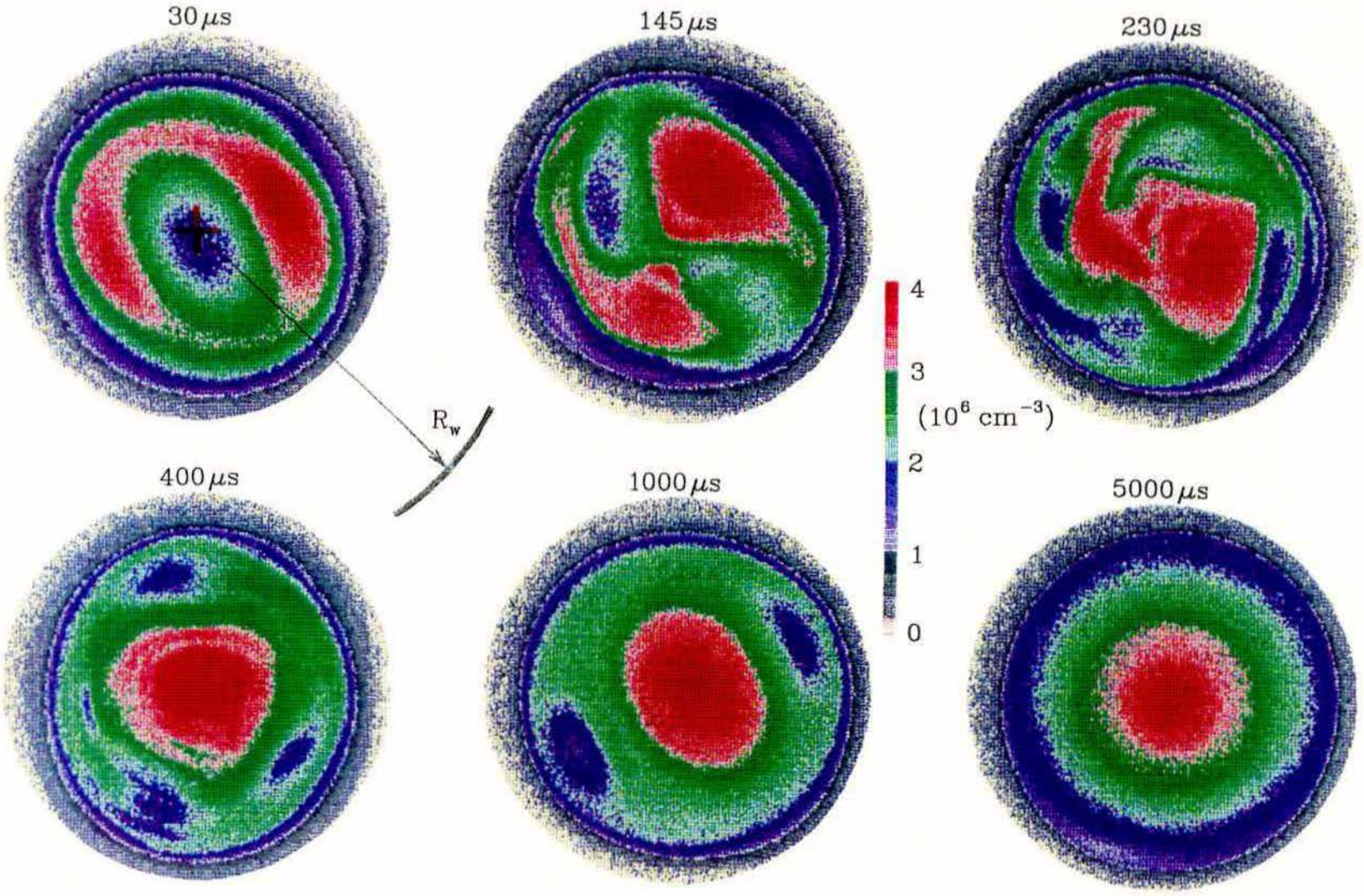

Figure 4.1: CCD camera images of $n(r, \theta, t)$ at a series of times of the $l = 2$ evolution.

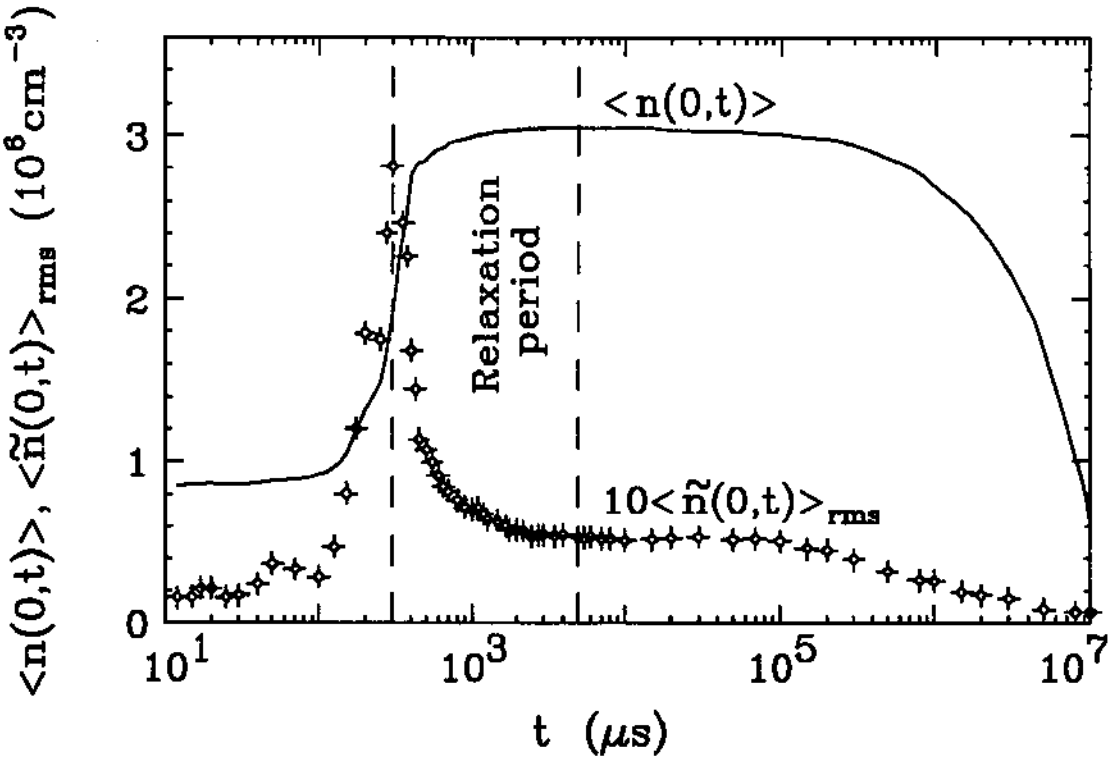

Figure 4.2: Long-term temporal evolution of the central mean density $< n(0,t) >$ and fluctuation level $< \tilde{n}(0,t) >_{\rm rms}$ (the $l = 1$ sequence).

The overall column evolution can also be studied using the ensemble averages described in Chapter 3. Figure 4.2 shows the evolution of the central mean density $< n(0,t) >$ and fluctuation level $< \tilde{n}(0,t) >_{\rm rms}$ of the $l = 1$ sequence over 10 second temporal span. At the early stage, the initial increase in the fluctuation level reflects similar unstable mode growth and saturation ($l = 1$ in this case). The subsequent ascend of the mean density underlies the convective inward transport; concurrently, large-amplitude fluctuations are generated indicating the onset of the turbulence in the column. The relaxation period of the evolution occurs approximately between $t = 300$ μs and 5 ms (corresponding to $t = 230$ μs – 5 ms for the $l = 2$ sequence), as marked by the dashed vertical lines in Figure 4.2.

After $t = 5$ ms, the mean density and fluctuation level remain essentially

unchanged for about 100ms, or 10^4 column bulk rotations, reflecting the fact that the dissipation of the system is quite small. The measured long-lasting fluctuations (3–5 times greater than that of the initial state) are caused by the shot-to-shot variations of the radial profile of the meta-equilibrium column (see Section 5.3). Eventually, the meta-equilibrium column decays away in a few seconds, on the same time scale associated with the microscopic "viscous" process which drives the column to its 3D thermal equilibrium, and other mechanisms that transport electrons to the cylinder wall. At $t = 5\,\mathrm{s}$, as the radial profile $< n(r, t = 5\mathrm{s}) >$ indicates (shown in Figure 2.4), significant fraction of the electrons are lost to the boundary. These 3D dissipation effects are beyond the scope of this work.

4.2.1 Correlation Measurements of Diocotron Instability and Turbulence

Diocotron instabilities are equivalent to Kelvin-Helmholtz shear-induced instabilities in fluid flows, and have been experimentally studied on magnetized electron annuli and hollow columns by many investigators [96, 18, 19, 80, 73]. Generally speaking, according to Rayleigh's stability criterion (see e.g., [46]), electron columns with monotonically decreasing radial density profiles are stable against all 2D perturbations. For columns with non-monotonic radial profiles, however, there normally exist unstable modes, which can grow exponentially to large amplitudes and change the column density distribution as a result.

Detailed experimental investigation of the linear $l = 1$ and $l = 2$ diocotron instabilities on hollow columns that are similar to the ones used in this work were carried out by Driscoll. For $l = 2$ mode, general agreements with the 2D inviscid theory has been found [19]; for $l = 1$ mode, some subtle discrepancies with a theoretically predicted mode having algebraic growth have been observed [18, 89]. Here, the theory predicts that the $l = 1$ unstable mode grows algebraically from $t = 0$, whereas

the experimental measurement shows an essentially exponential growth, even though the mode eigenfunctions are similar. This disagreement has been attributed to the small non-ideal effects that were entirely neglected in the 2D inviscid theory [86].

In Chapter 3, I have demonstrated that ensemble-average measurements can be utilized to study the normal modes of stable electron columns. Here, I apply this technique to analyze the unstable $l = 1$ diocotron mode of the hollow column. Special care is taken to prepare the initial hollow column at $t = 0$, so that the stable $l = 1$ (center-of-mass) mode is not present in the system (see Section 2.4).

Figure 4.3 shows the ensemble-average measurements of the initial hollow column at $t = 20\mu$s. The radial profiles of the measured mean density and fluctuation level are plotted in (a) and (b) respectively, while the correlation function C_{1r} is shown as a function of radius in (c). If one assumes that at 20μs (~ 2 bulk rotations) after hollowing, most of the perturbations which are not part of the unstable mode have phase mixed away, leaving only the single-mode perturbation in the hollow column, then the measured fluctuation level should be directly related to the unstable $l = 1$ eigenfunction $\tilde{n}^{(1u)}$ (see Section 3.4),

$$< \tilde{n}(r) >_{\rm rms} = \frac{1}{\sqrt{2}} \tilde{n}^{(1u)} ;$$

and the correlation function $C_{jr}(r, \theta)$ should be

$$C_{jr}(r, \theta) = \exp\{ i[(\theta - \theta_j) + \varphi_{1u}(r) - \varphi_{1u}(r_j)] \} ,$$

where (r_j, θ_j) is the position of the fixed collector Cj, and $\varphi_{1u}(r)$ is the phase of the eigenmode. Indeed, the ensemble-average fluctuation level $< \tilde{n}(r) >_{\rm rms}$ has a radial dependence qualitatively the same with that of the measured $l = 1$ eigenfunction for a somewhat different hollow column [18]. Furthermore, the correlation function $C_{1r}(r, \theta)$ shows that as the radius increases, the phase of the mode experiences a sharp shift from 0 to π at $r_{\rm max}$, the radius at which the mean density has the peak

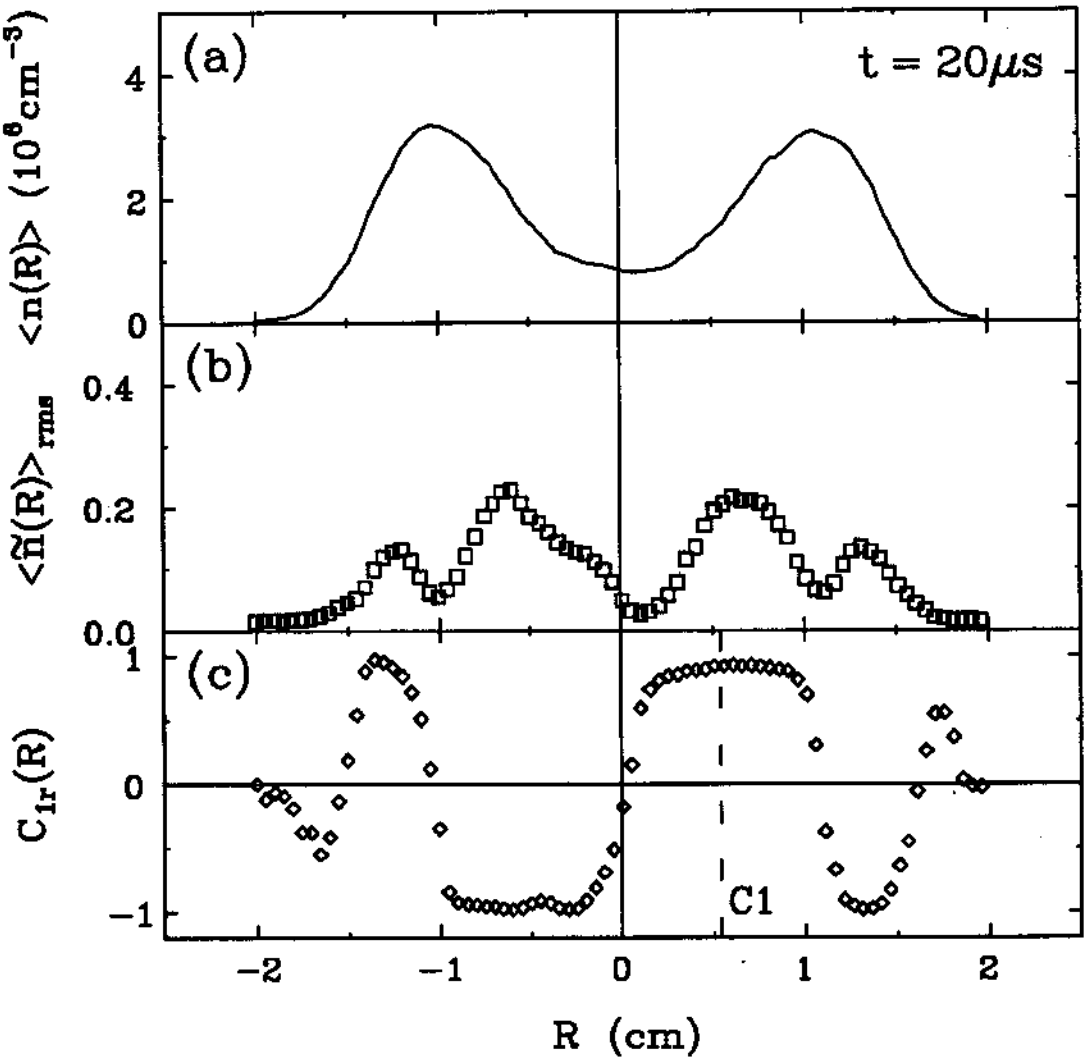

Figure 4.3: Ensemble-average measurements of the $l = 1$ unstable initial hollow column at $t = 20$ μs. (a) Mean density radial profile; (b) fluctuation level; (c) correlation function C_{1r} with the fixed collector C1 marked by the dashed line.

value, and then shift again from π to around 2π near the edge of the column. This is essentially the same mode phase behavior discovered experimentally by Driscoll [18]. These observations confirm that the measured perturbation at 20 μs is dominated by the single unstable $l = 1$ mode.

Analogous to the $l = 2$ sequence shown in Figure 4.1, the unstable $l = 1$ mode saturates to form a large-size blob. The subsequent nonlinear flow moves the large density blob to the column center, creating a globally stable mean density profile, and generates large-amplitude secondary turbulent fluctuations, such as filaments and vortices (see [19] for details). At $t = 400\,\mu$s, the column is qualitatively similar to the $l = 2$ evolution at $t = 230\,\mu$s, as shown in Figure 4.1, characterized by a monotonically decreasing mean density profile with large-amplitude turbulent fluctuations.

Figure 4.4 shows the ensemble-average measurements of the turbulent column (the $l = 1$ sequence) at $t = 400$ μs. The radial profile $< n(r) >$, plotted in (a), has become monotonically decreasing; large-amplitude fluctuations ($< \tilde{n} >_{\rm rms} / < n >$ $\sim$ 30%) are observed, as shown in (b), which are approximately 4 times greater than that of the column at $t = 20$ μs. From the correlation functions $C_{2r}(r)$ and $C_{2-r}(r)$, plotted in Figure 4.4(c) and (d), one can see that the measured large-amplitude fluctuations are no longer dominated by a single global mode, since neither $C_{2r}(r)$ nor $C_{2-r}(r)$ shows significant long-range coupling associated with a single-mode perturbation, indicating that the column is indeed quite turbulent at this time.

The excitation of turbulence in the column is transient in nature and soon gives away to the stabilizing effect of the column background rotation induced by the mean density radial profile. The column evolution then enters the relaxation period.

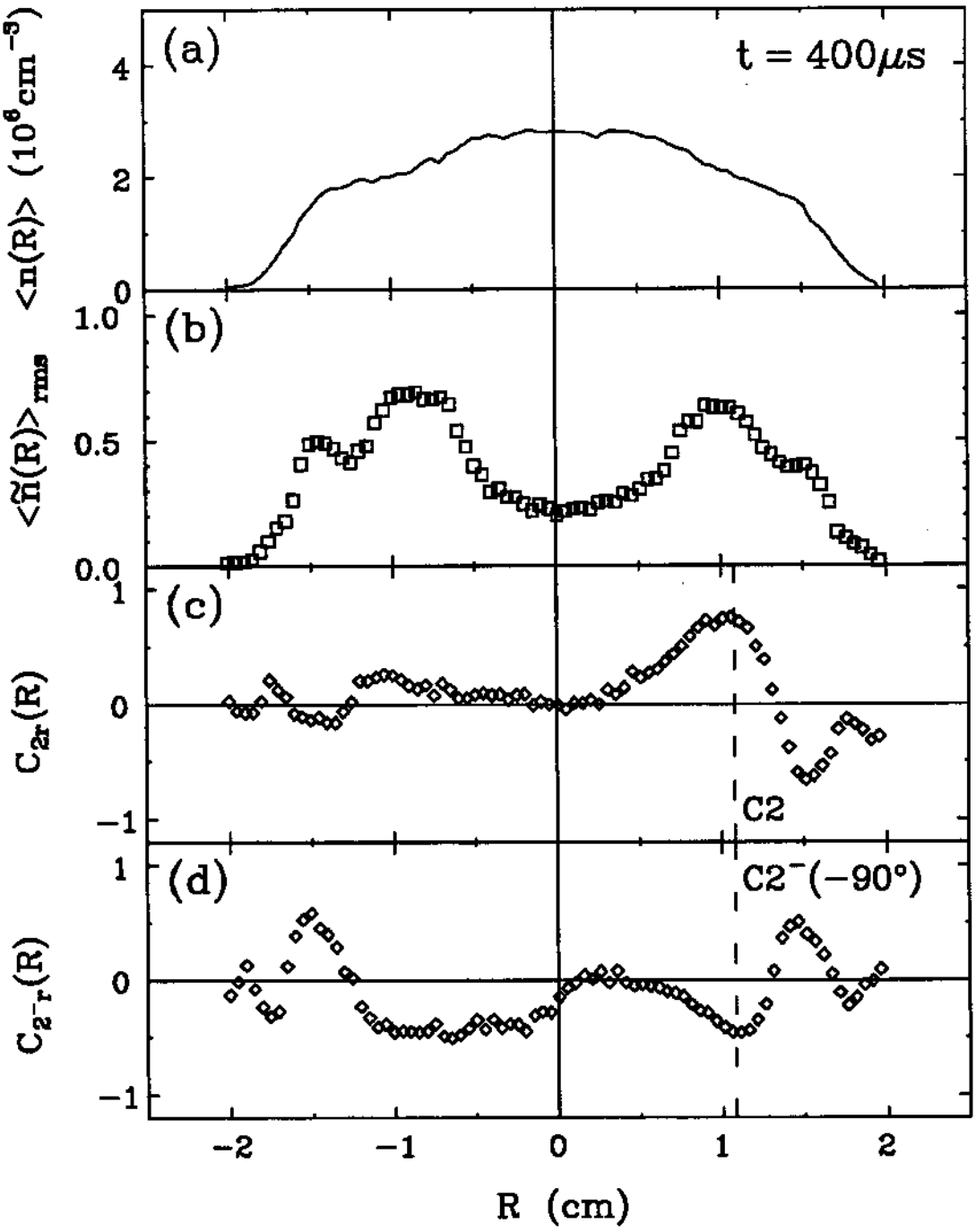

Figure 4.4: Ensemble-average measurements of a turbulent column ($l = 1$) at $t = 400$ μs. (a) Mean density radial profile; (b) fluctuation level; (c) correlation function C_{2r} with the fixed collector C2 marked by the dashed line; (d) correlation function C_{2-r} with C2$^-$ being $-90°$ from C2.

4.3 Measurements of the Relaxation Period

4.3.1 Background Rotation and Passive Tracer Decay

The existence of the column background rotation has a profound influence on the relaxation of 2D turbulence in the system. Unlike 2D neutral turbulence studied in computer simulations, the background rotation breaks the symmetry between plus and minus vorticity distributions, and dominates the convective flow dynamics, as will be illustrated in this section. During most of the relaxation period, the column mean density profile, which induces the background rotation, experiences only small and gradual changes. For example, for the $l = 1$ evolution, Figure 4.2 shows that the central mean density $< n(0) >$ increases by less than 10% between the turbulent column at $t = 400\ \mu$s and the meta-equilibrium state at $t = 5$ ms. Therefore, the properties of the background rotation can be studied at one particular time.

For the $l = 2$ evolution at $t = 1$ ms, the radial profiles of the background mean vorticity $< \zeta(r) > = 4\pi ec < n(r) > / B_z$ and rotational angular velocity $\omega(r)$ are shown in Figure 4.5(a), while their radial gradients are plotted in Figure 4.5(b). The mean density $< n(r) >$ is the θ-averaged radial profile taken from the CCD camera image averaged over 4 shots at $t = 1$ ms. The angular velocity $\omega(r)$ is calculated from $< \zeta(r) >$,

$$\omega(r,t) = \frac{1}{r^2} \int_0^r dr'\, r' < \zeta(r') > ,$$

which is the background rotational environment seen by the turbulent fluctuations during the relaxation period. As shown in Figure 4.5, the mean density profile is not uniform, with a monotonically decreasing distribution. Consequently, the rotational motion described by $\omega(r)$ is sheared, characterized by the rotational shear rate

$$r\frac{d\omega}{dr} = < \zeta(r) > -2\omega(r) , \tag{4.1}$$

which is zero at the column center and negative everywhere else. At $R \simeq 1$ cm,

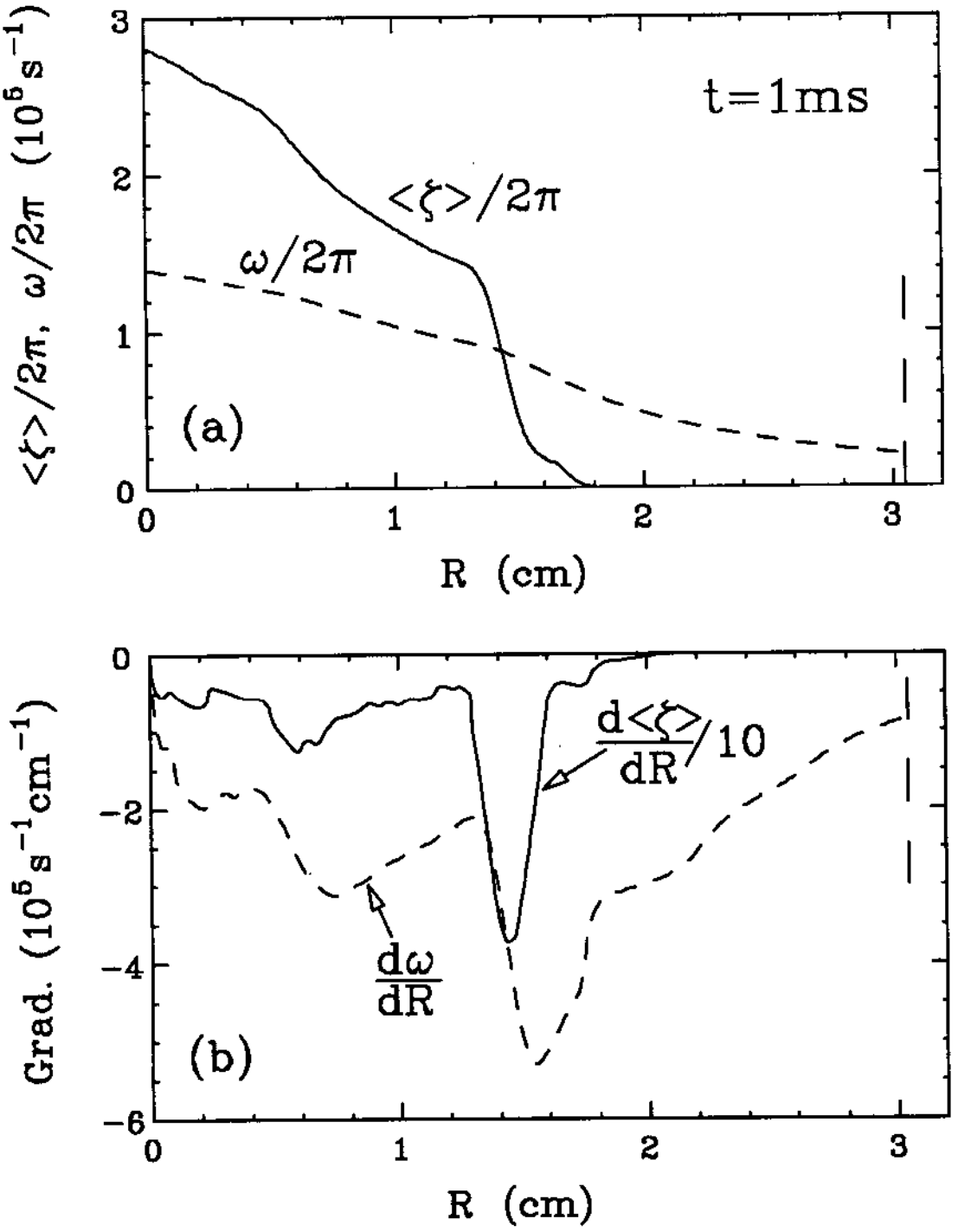

Figure 4.5: Column background rotation at $t = 1$ ms (the $l = 2$ sequence). (a) Radial profiles of the mean vorticity $<\zeta(r)>$ and angular velocity $\omega(r)$; (b) radial gradients of $<\zeta(r)>$ and $\omega(r)$.

the bulk rotation period is about 10μs, and the shear rate $rd\omega/dr$ is about -2.7×10^5 s^{-1}. Note that, in general, the convective velocity seen by any fluid element is the combination of the background rotation and the convection due to all other fluctuating structures.

If one assumes that the dynamical effect of the fluctuations $\tilde{n}(r,\theta,t)$ is negligible, i.e., the fluctuating velocity $\tilde{\mathbf{v}}(r,\theta,t)$ is small compared to the background rotation, the passive tracer mixing model can be constructed, which describes the simplest kind of relaxation [76]. Here, $\tilde{n}$ is treated as a conserved passive tracer that is merely being convected by the prescribed background rotation $\omega(r)$. Applying $\tilde{\mathbf{v}} = 0$ to the inviscid Equations (3.12) and (3.13), one gets

$$\frac{\partial \tilde{n}}{\partial t} + \omega(r)\frac{\partial \tilde{n}}{\partial \theta} = 0\,, \tag{4.2}$$

which determines the dynamics of the passive tracer distribution $\tilde{n}(r,\theta,t)$.

According to Equation (4.2), for a rigid rotor column background rotation $\omega(r) = \text{const}$, distribution $\tilde{n}$ does not change in the rotating frame. When the gradient of $\omega(r)$ is not zero, however, the differential rotation can break up the original density variations through phase mixing, typically on the time scale of a few column bulk rotations. Using the azimuthal Fourier decomposition described by Equatons (3.15), the evolution of the density component $\tilde{n}^{(l)}(r,t)$ for modenumber l is determined by Equation (4.2),

$$\tilde{n}^{(l)}(r,t) = \tilde{n}_0^{(l)}(r)\,\exp[-il\omega(r)\Delta t]\,, \tag{4.3}$$

where $\tilde{n}_0^{(l)}(r)$ is the Fourier component of the original density distribution $\tilde{n}(r,\theta,t_0)$, with t_0 being the start of the relaxation and $\Delta t \equiv t - t_0$.

In this inviscid model, the phase mixing induced decay occurs when a finite-size collector (diameter $2R_C$) centered at (r_j,θ_j) is used to measure the real density distribution. Following the same procedure to derive collector coarse-graining effect

in Section 3.4, one can show that the measured Fourier component $\tilde{n}_c^{(l)}(r_j,t)$ is

$$\tilde{n}_c^{(l)}(r_j,t) \simeq \tilde{n}_0^{(l)}(r_j)\,\exp[-il\omega(r_j)\Delta t]\,[\frac{2J_1(\chi_l\Delta t)}{\chi_l\Delta t}]\,, \tag{4.4}$$

and the characteristic mixing rate for component l is

$$\chi_l(r_j) = -l\frac{R_C}{R_w}\frac{d\omega}{dr}|_{r_j}\,, \tag{4.5}$$

where I have assumed that the radial lengthscales of the original density variations are larger than $3R_C$ and that the linear Taylor expansion of ω can be used over the cross-section of the collector, i.e., $\omega(r) \simeq \omega(r_j) + (d\omega/dr)\,|_{r_j}\,(r - r_j)$.

It is clear from Equation (4.4) that the decay of the measured passive tracer intensity is caused by the continuous transformation of structures with large radial lengthscales into ones with fine radial lengthscales, which can not be detected by the finite-size collector (see Section 3.4). Physically, this reflects the fact that a patch of passive tracer in a background rotation is being sheared apart and "wrapped" around as the time progresses, resulting in the creation of fine filaments which are too thin to be discerned.

For collector radius $R_C = R_{C0} = 0.20$ cm at $R \simeq 1$ cm, and gradient $d\omega/dR \simeq -2.7 \times 10^5\ \mathrm{s^{-1}cm^{-1}}$, the $l = 2$ passive tracer e-folding decay time is $\tau_2 \equiv 2.8/\chi_2 \simeq 30\ \mu$s, or about 3 column rotations. This highly simplified relaxation model is seen to be a poor description of the experimental data in the following discussions.

4.3.2 Phase I – Filamentation and Mixing

From CCD camera images of the $l = 2$ evolution (shown in Figure 4.1), it is observed that the early-time relaxation (Phase I) is characterized by the rapid filamentation and mixing of the fluctuating turbulent density clumps (electron surpluses) and shallow holes (deficiencies) which are generated by the merger of the two

large-size density blobs. This phase lasts approximately 150 μs, or about 15 bulk rotations. Images indicate that the clumps and shallow holes are being sheared apart into spiral-like thin filaments by the strong background differential rotation, which has nearly finished its formation. This shear-induced filamentation has previously been studied by Marcus in a computer simulation [52] and observed experimentally by Sommeria *et al.* in a forced rotating fluid system. The spiral shape of the density clumps being sheared apart may be the underlying dynamical reason for the observed "peaks" and "dips" near $R \simeq 1.5$ cm in the profiles of the correlation function C_{2r} and C_{2-r} shown in Figure 4.4.

By $t = 400\mu$s (see Figure 4.1), Phase I of the relaxation is essentially complete, with the turbulent density clumps and shallow holes having been filamented and destroyed, leaving only a few medium-size deep density holes prominently visible in the column. This marks the beginning of the Phase II of the relaxation. It is worth noting that the turbulent filamentation and mixing in Phase I apparently cause significant dissipation in the measured fragile ideal invariants of 2D $\mathbf{E} \times \mathbf{B}$ dynamics, such as the enstrophy $\mathcal{Z}_2$, as will be discussed in Section 5.3. Similar dissipation is also observed in the merger of two isolated columns [60].

Let's examine the decay of the ensemble-averaged fluctuation level and make the comparison with the simple passive tracer model. Figure 4.6 shows the relaxation of the mean density and the fluctuation level measured by a collector (diameter $2R_{C0} = 0.40$ cm) positioned at $R = 1$ cm. At $t = 300$ μs, $< n(1\text{cm}, t) >$, plotted in Figure 4.6(a), has basically reached a constant level, indicating that the background rotation is well established at this time. Therefore, for this $l = 2$ evolution, $t = 300\,\mu$s is designated as the theoretical starting time t_0 for the passive tracer relaxation model, shown as the solid curve in Figure 4.6(b). It is clear that the measured fluctuation decay is very gradual compared to that of the passive tracer, typically

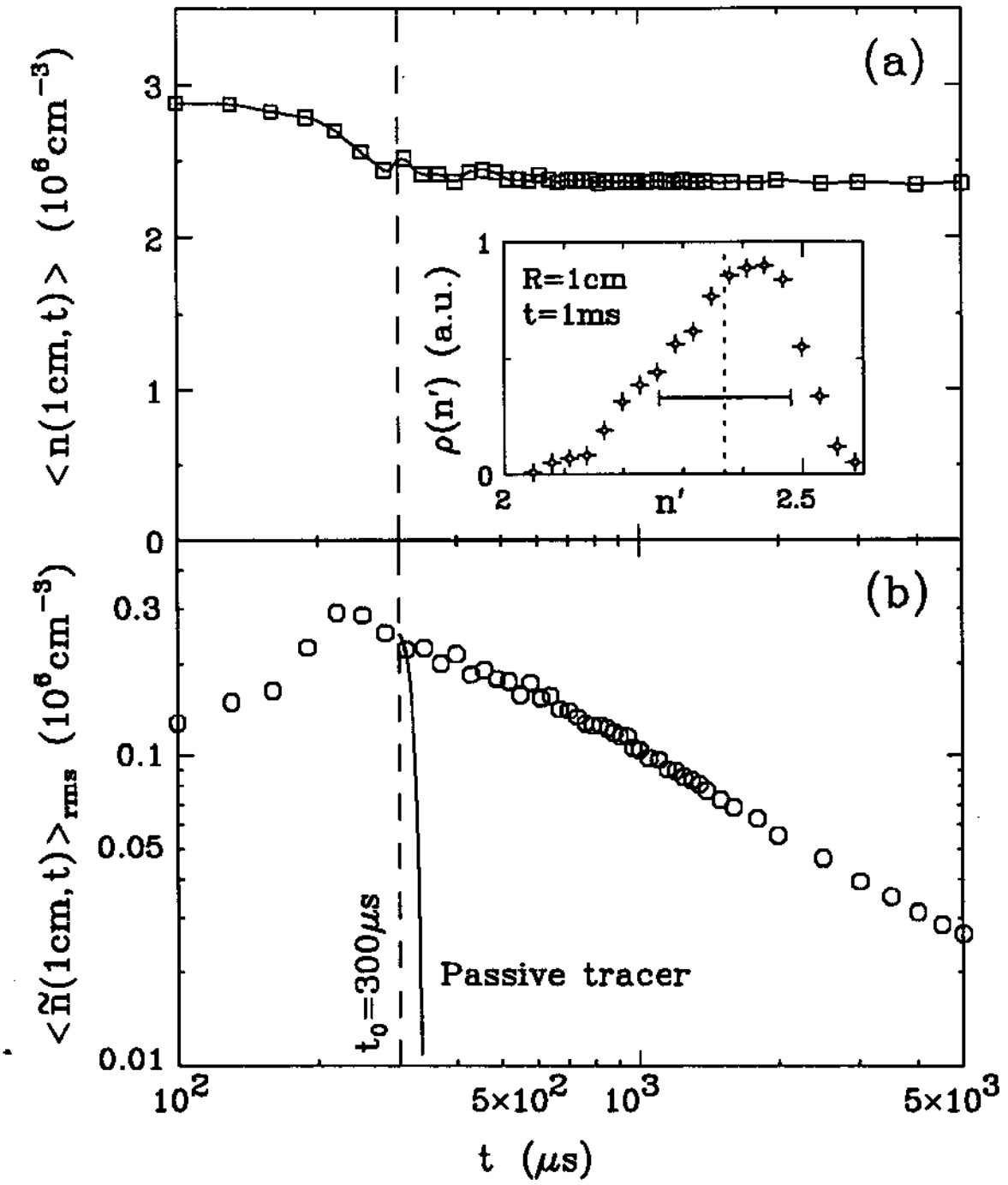

Figure 4.6: The relaxation of the mean density $< n >$ and the fluctuation level $< \tilde{n} >_{\rm rms}$ at $R = 1$ cm. (a) Mean density $< n(1{\rm cm}, t) >$ versus time, and the PDF $\rho(n', 1{\rm cm}, 1{\rm ms})$ versus n' (inserted graph), with the dotted line being $< n >$ and the bar being $2\times < \tilde{n} >_{\rm rms}$; (b) the decay of the fluctuation level $< \tilde{n}(1{\rm cm}, t) >_{\rm rms}$ and the prediction of the passive tracer model (for $l = 2$).

over 10 times slower at various column radii and for other evolutions. This suggests that some fluctuating structures are nonlinear and self-coherent in nature, and do not behave like passive tracers. Indeed, as shown in the inserted graph in Figure 4.6(a) , the measured PDF $\rho(n', 1\text{cm}, 1\text{ms})$ (defined in Section 3.4) has a characteristic skewed shape with a long low-amplitude "tail" on the small density side, indicating that spatially-isolated deep density holes dominate the measured late-time fluctuations.

Both the CCD camera images and the ensemble-average measurements show that the relaxing electron column can have long-lived density holes (i.e., regions of negative relative vorticity) embedded in the background rotation, but not density clumps (regions of positive relative vorticity). This observation can be quantitatively explained by an idealized model adopted from the original work by Moore and Saffman [65, 38], which describes how an individual vorticity clump or hole behaves under a shearing background rotation. This model treats the interior vorticity distribution of a clump or hole as an elliptical vortex (aspect ratio λ_v) with uniform relative vorticity $\tilde{\zeta}_v$ being embedded in a background rotation $\omega(r)$. In addition, the size of the vortex is assumed to be small compared to the radial length over which ω varies, so that near the vortex center r_v, the linear Taylor expansion of the background rotation can be used, i.e., $\omega(r) \simeq \omega(r_v) + (d\omega/dr)\,|_{r_v}\ (r - r_v)$.

Here, the scaled shear rate σ of the background rotation $\omega(r)$ is defined as

$$\sigma \equiv r_v \frac{d\omega}{dr}\,|_{r_v}\ /\tilde{\zeta}_v\ ,$$

which is the ratio of the vorticity in the background rotation and the relative vorticity of the elliptical vortex (see Appendix B). Following the derivations of Moore and Saffman [65], one can show that for certain values of σ, the vortex can achieve stable dynamical equilibrium with the background flow by orienting its major axis to the $\hat{\boldsymbol{\theta}}$-direction (for $\sigma > 0$), or to the $\hat{\mathbf{r}}$-direction (for $\sigma < 0$). Let a be the elliptical semi-axis in the $\hat{\boldsymbol{\theta}}$-direction, the equilibrium aspect ratio $\lambda_{\text{eq}} \equiv a/b$ must satisfy the

relation,

$$\lambda_{\rm eq} = \begin{cases} -\dfrac{2\sigma}{1+\sigma-\sqrt{1+6\sigma+\sigma^2}} & -(3-2\sqrt{2}) \le \sigma < 0 \\ \dfrac{1+\sigma+\sqrt{1+6\sigma+\sigma^2}}{2} & 0 \le \sigma < \infty\,. \end{cases} \tag{4.6}$$

This prediction is plotted as the solid curve in Figure 4.7. For the background rotation considered here, $d\omega/dr \le 0$, therefore, σ is positive for vorticity holes, i.e., hole rotates in the same direction as that of the background shear; whereas σ is negative for vorticity clumps, i.e., hole rotates against the background shear. From Equation (4.6), it is clear that in order for a clump to survive the adverse background shear, it must be quite intense, i.e., $|\sigma|$ must not be less or equal than $3-2\sqrt{2}$, or alternatively,

$$\tilde{\zeta}_v \ge -(3+2\sqrt{2})\, r_v \frac{d\omega}{dr}|_{r_v}\ . \tag{4.7}$$

Experimentally, for a typical density profile during the relaxation, this necessary condition generally can not be satisfied by a clump located inside the column. This can be seen from the following example: for a parabolic background radial profile $<n(r)>=<n(0)>\,(1-r^2/r_0^2)$, it can be shown from Equation (4.7) that the absolute density $n_v \equiv \tilde{n}_v + <n(r_v)>$ of a clump at radius r_v must fulfill the requirement

$$\frac{n_v}{<n(0)>} \ge 1 + (\frac{1}{2}+\sqrt{2})\,\frac{r_v^2}{r_0^2}\,,$$

which is impossible under 2D incompressible dynamics, since $<n(0)> \lesssim n_{\rm max}$, where $n_{\rm max}$ is the peak density in the initial condition (see Section 5.3). In fact, if one assumes that $n_v = <n(0)>$, in order to survive the adverse shear in the background rotation, the density clump has to go out of the column, with

$$\frac{r_v}{r_0} \ge \sqrt{\frac{3}{2}+\sqrt{2}}\,.$$

In contrast, according to Equation (4.6), arbitrarily weak holes can survive the background shear in principle, albeit with large aspect ratio $\lambda_{\rm eq}$, because density

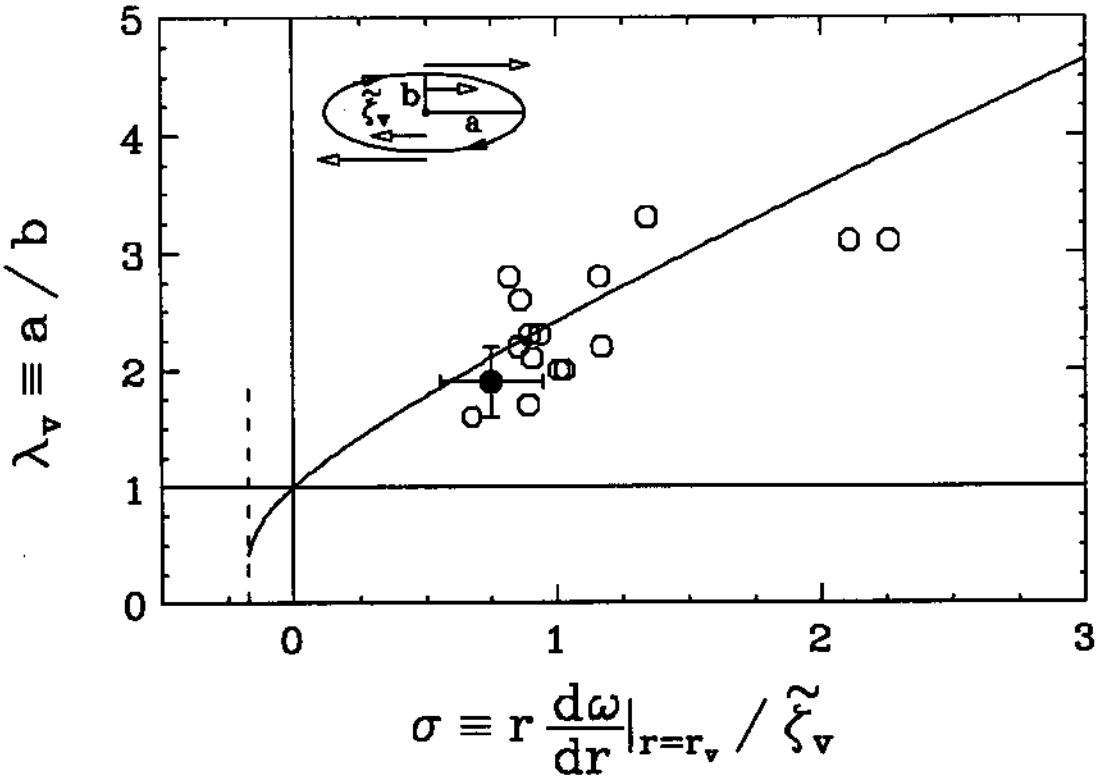

Figure 4.7: Model for the quasi-stability of density holes in a shearing background rotation. Equilibrated aspect ratio λ_{eq} is plotted versus the scaled background rotation shear rate σ, from measurements (symbols) and from the theoretical prediction (curve).

holes are prograde with respect to the shear. Of course, one would expect that when a holes is too weak, it is simply filamented and axisymmetrized in the column. In the experiments, I see holes with relative density depth $0.2 \lesssim \tilde{n}_v / <n(r_v)> \lesssim 0.4$, resulting in observed λ_v falling between 1.5 and 3.0.

Measurements of the aspect ratios of the observed density holes in CCD camera images between $t = 400$ μs and $t = 4$ ms are shown in Figure 4.7 as symbols. Here, the scaled background shear rate σ is calculated from the rotation profile shown in Figure 4.5 and the difference between the central vorticity of the holes and the mean vorticity at that radius. The aspect ratios λ_v is measured manually

from the images for one density contour of the holes, e.g., the blue-green transition in Figure 4.1. Reasonable agreement between the measurement and the model is found, validating the applicability of the model to these columns. Some discrepancies arise, since the holes have a nonuniform interior density distribution, and since neither deformation of the column core nor the influences of other holes is included in this simple model.

4.3.3 Phase II – Interactions of Coherent Holes

During the Phase II of the relaxation, columns with 3 or more medium-size holes generally involve to having 2 holes located opposite to each other in θ (for the $l = 2$ sequence). This can involve merger, or mutual advection causing 1 hole to move outward and be destroyed by the background shear, or other processes. I do not observe in-place dissipation of the individual holes, presumably because the size of the holes are large compared to the dissipation lengthscale. The symmetric two-hole configuration ("tripole") appears to be particularly stable and long-lived. On a somewhat longer time scale, the two holes tend to drift outward radially, where they are finally sheared apart (Phase III).

Figure 4.8 presents a density hole "census" as a function of time. The number of observed elliptical holes $N_{\rm hole}$ is plotted versus t. Cross symbols represent images where the positions of the holes are irregular in θ, and circle symbols represent images where the holes are symmetrically configured, i.e., they are at same r, and less than $\pm 10^\circ$ deviation from symmetric θ positions. Statistically speaking, at early stage of the relaxation, there are more holes, and they are generally irregularly positioned. As the relaxation progresses, $N_{\rm hole}$ decreases, and the holes settle into symmetric configurations (mostly tripoles). After $t \simeq 800\,\mu$s , virtually all the images are in the tripole configuration, as shown in Figure 4.1 (at 1000 μs), with a large oval-shaped core and two elliptical holes opposite in θ. This tripolar state likely reflects the early

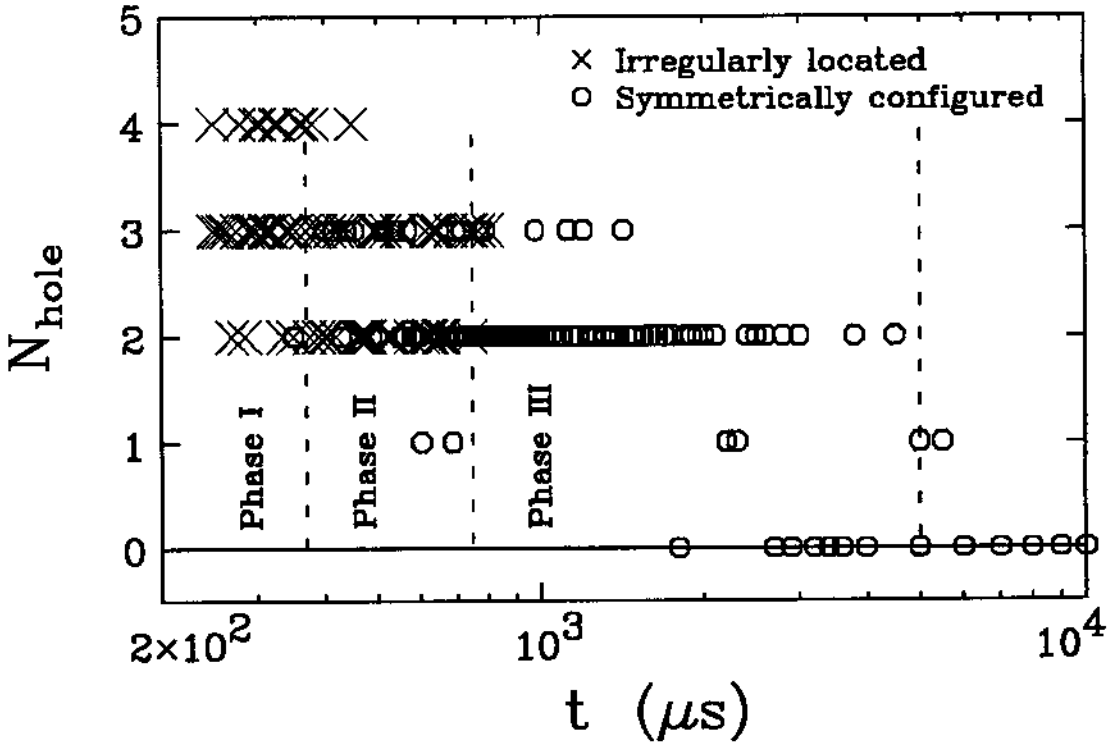

Figure 4.8: Observed number of holes in the column versus time, compiled from about 200 CCD images between $t = 400$ μs and 10 ms, with crosses representing irregularly located holes and circles representing symmetrically configured holes.

$l = 2$ diocotron instability, in fact, dipolar configurations are normally observed for columns with $l = 1$ mode growth (not shown).

In Phase II, the main drive for relaxation appears to be the mutual interactions between the holes embedded in the background rotation. For example, the decrease in the number of density holes is due to binary holes mutual advection and merger events. These hole merger events have been observed among the CCD camera images during this phase of the relaxation. The dynamical bases for the merger have not been established experimentally. However, two holes that are at slightly different radial positions are convected at different angular velocity, thus, the hole that is closer to the center will be able to catch up with the other and likely to merge,

presumably within several rotations. Of course, they may alternately be so far apart radially that they are unable to get into contact at all. It is worth pointing out that compared to the case of two isolated vortices, the presence of the strong rotational background seems to have profound influences on the merger dynamics of the holes [53]: first, these holes take the elliptical shape with major axis in the θ-direction and aspect ratio of about 2, whereas two merging isolated vortices are deformed under their mutual influence with their major axes pointing toward each other [83, 32]; second, two holes must also overcome the strong tendency of maintaining their azimuthal orbital motion in order for the merger to happen, or else they simply scrape past each other [53].

Hole mutual interaction can cause the merger of two holes that are at the same radii but separated by a short azimuthal angle ($< 90°$), as first suggested by Marcus [53]. Since the mutual interaction between two neighboring holes tends to generate rotation around their center of mass (see Appendix C), this small rotation perturbs the radial positions of the two holes, enabling the trailing hole to move slightly inward and the leading hole slightly outward, resulting in either the leading hole being sheared apart by the background or their complete merger. This mechanism is consistent with the fact that late-time columns normally have only 2 holes left (1 or 3 on rare occasions), which are always far apart in their θ position. In principle, there can also be some mechanism which makes the symmetric configuration to be the most probable state.

One can understand the observed quasi-stability of the tripolar configuration by noting that the elongated core tends to maintain the symmetric θ-positions of the 2 remaining holes (see Figure 4.1). Here, I argue that for a hole, the dominant interaction is with the deformed core rather than the other hole, since they are far apart in this case. Core region acts like a vortex with positive vorticity at the center,

which adjusts its shape in response to the location of the holes. In the tripole case, the core vortex takes an oval shape with it major axis oriented parallel to those of the symmetrically positioned holes. The stability argument is the following: suppose that the radial position of a hole is perturbed slightly inward, its orbital motion then will speed up, allowing it to catch up with the other hole; however, this trend is suppressed by the core, since its influence tends to move the hole outward radially, slowing it down and restoring the symmetric configuration. The observed longevity of the tripolar configuration (> 200 rotations) supports this stability argument.

4.3.4 Phase III – Hole Radial Drift and Axisymmetrization

In Phase III of the relaxation, the quasi-stable tripolar configuration is destroyed by a slow outward drift of the holes. Figure 4.9 shows the radial position $R_{\rm hole}$ of the hole centers versus time, measured from the CCD camera images. Most of these images have two symmetrically positioned holes. These holes travels from $R_{\rm hole} \simeq 1.0\,{\rm cm}$ to $R_{\rm hole} \simeq 1.5\,{\rm cm}$ within about $5\,{\rm ms}$, giving an estimated drift speed of $0.1\,{\rm cm/ms}$. The scattering of the data points reflects the shot-to-shot irreproducibility of this $l = 2$ evolution. The cause of this outward motion is unknown at this moment. However, the experiments varying L_p and B_z suggest that this outward drift is 2D $\mathbf{E} \times \mathbf{B}$ drift in nature. Note that holes that are strictly symmetric in θ-position do not feel $\mathbf{E}$ field in the θ-direction, and consequently have no radial drift velocity. Therefore, any radial drift motions must come from asymmetric effects.

The outward radial drift apparently causes these holes to stretch in the azimuthal direction and to be axisymmetrized eventually. This is because that as a hole moves outward radially, it should maintain its absolute density according to the 2D dynamics; when the hole is no longer deep enough with respect to the background, it is stretched apart and axisymmetrized by the shear in the background rotation. This

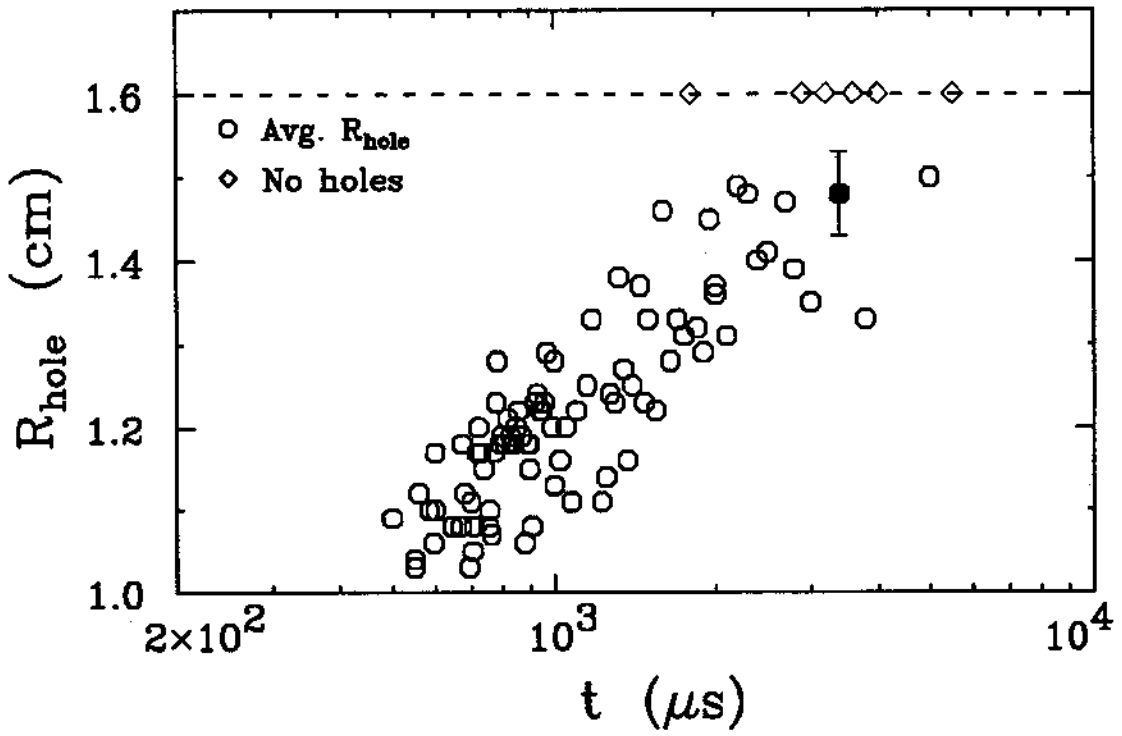

Figure 4.9: Average radial positions of hole centers versus time, measured from CCD images of the $l = 2$ sequence between $t = 500$ μs and 5 ms. The dashed line marks the radial extent of the column.

argument can be seen graphically from Figure 4.10, where the expected hole equilibrium aspect ratio λ_{eq} is plotted as a function of the radial position R_v of the hole. Here, I assume that the hole always has a uniform density of $n_v = 1.2 \times 10^6$ cm^{-3} (similar to the ones shown in Figure 4.1 at 1000 μs), and that as the hole drifts out, it remains equilibrated with the background rotation. At around $R_v \simeq 1.4$ cm (see Figure 4.5 for the background rotation), λ_{eq} becomes large, indicating large extension in the azimuthal direction of the column. For example, in Figure 4.1 at $t = 5000$ μs, an azimuthally long-stretched hole is still visible near the column edge at lower left corner, which is probably going to be completely destroyed soon.

The column axisymmetrization process can also be observed from the mea-

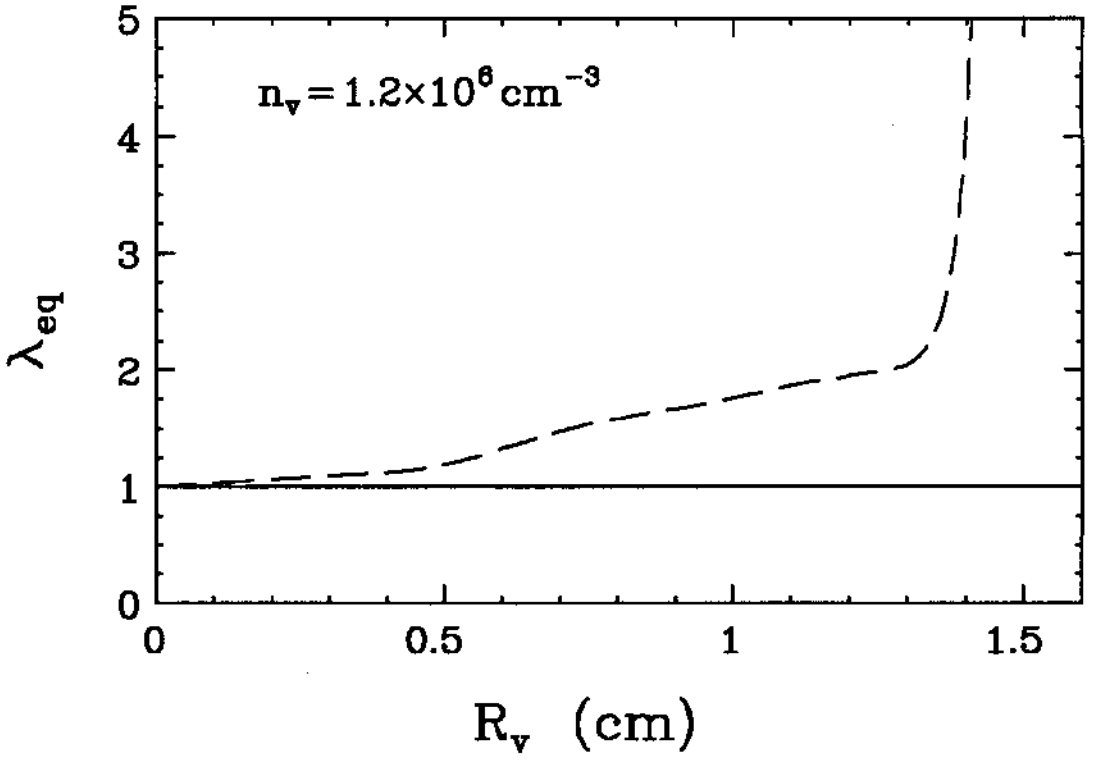

Figure 4.10: Theoretically expected hole aspect ratio λ_{eq} versus its radial position R_v, for a hole with central absolute density $n_v = 1.2 \times 10^6$ cm^{-3}.

sured two-point correlation functions. Here, I use the $l = 1$ evolution as an example, whose initial condition is shown in Figure 4.3. Using the endplate multi-collector array, angular correlation function $C(R, \Delta\theta, t)$ between two collectors at the same radius R and separated azimuthally by $\Delta\theta$ (e.g., C2 and C2$^-$, or C3 and Cr at $R = -1.6$ cm) can be calculated as functions of time. Figure 4.11 shows the evolution of $C(R, \Delta\theta, t)$ at 3 radial positions ($R = 0.5$ cm, 1.0 cm, and 1.6 cm) and 2 $\Delta\theta$ separations ($\Delta\theta = 90°$ and 180°). At the early times, these functions show perfect anti-correlation for $\Delta\theta = 180°$ and near zero correlation for $\Delta\theta = 90°$, reflecting the growing unstable $1 = 1$ mode. In Phase I and II of the relaxation, these correlations are generally near zero, due to the small spatial scales of the turbulent density structures and coherent holes. After $t = 1$ ms, in Phase III, all the functions

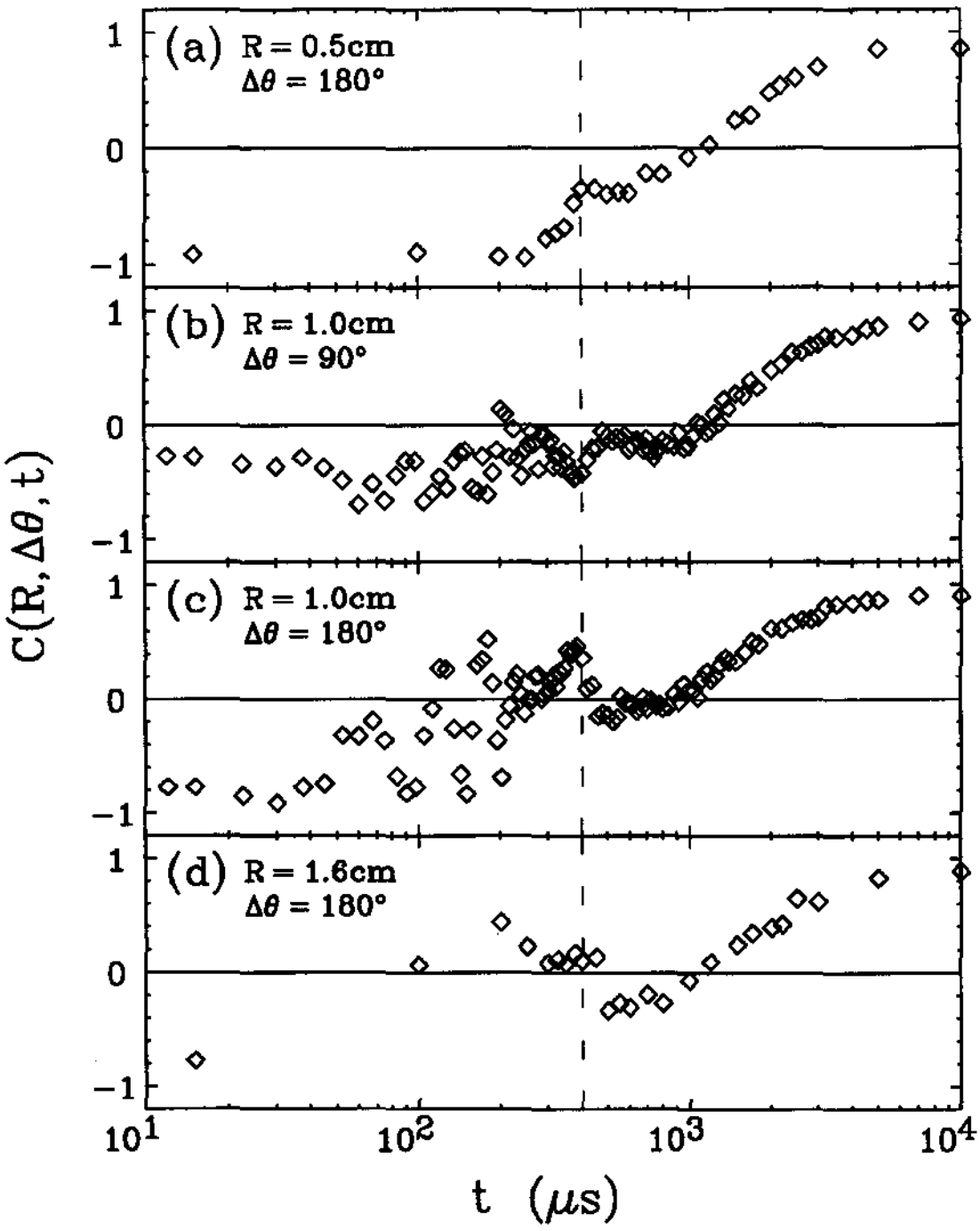

Figure 4.11: Evolution of the θ-correlations $C(R, \Delta\theta, t)$ of the $l = 1$ sequence showing the column axisymmetrization. (a) $C(0.5\text{cm}, 180°, t)$; (b) $C(1\text{cm}, 90°, t)$; (c) $C(1\text{cm}, 180°, t)$; (d) $C(1.6\text{cm}, 180°, t)$. The dashed line marks the time $t = 400\ \mu$s which is shown in Figure 4.4.

start to approach unity at roughly the same rate, indicating that the θ-variations are decaying away, leaving the axisymmetric shot-to-shot variations ($\sim 2\%$) of the radial profile to dominate the measured noise.

This late-time axisymmetrization process can be seen in greater detail in the evolution of the radial correlation functions $C_{j_r}(R,t)$. Figure 4.12 shows the radial profiles of $C_{2_r}(R,t)$ at 3 times during Phase III of the relaxation. At $t = 1$ ms, the radial correlation is localized around the position of C2, underlying the narrow radial extent of the density hole(s); as the relaxation progresses, radial correlation patterns appear ($t = 2$ ms), and at $t = 5$ ms, nearly perfect correlation is achieved for the same radius $R \simeq 1$ cm, even at $\Delta\theta = 180°$. Figure 4.13 shows the corresponding evolution of $C_{2^-{}_r}(R,t)$, where the fixed collector $C2^-$ is at the same radius of C2, but separated $-90°$ azimuthally (see Figure 2.2). Again, near zero correlations for all radii are observed at $t = 1$ ms, in agreement with Figure 4.11(b); as the column further relaxes, symmetric patterns develop ($t = 2$ ms), and perfect correlations are achieved for the same radius, at $\Delta\theta = \pm 90°$. These radial correlation measurements again show that all the θ-variations are decaying away while radial variations remain, demonstrating that the late-time Phase III of the relaxation indeed brings the complete axisymmetrization of the column.

It is useful to characterize the axisymmetrization rate, in light that its mechanism is still unknown yet. As mentioned above, the residual fluctuation level reflects the shot-to-shot variations of the axisymmetric meta-equilibrium radial profiles, and is different in nature compared with the decaying azimuthal fluctuations. Therefore it is logical to decompose the measured fluctuation level into two parts: $<\tilde{n}_\theta(t)>_{\rm rms}$ which is θ-dependent and is decaying to zero, and $<\tilde{n}_r(t)>_{\rm rms}$ which remains constant during the axisymmetrization, with the relation

$$[<\tilde{n}(t)>_{\rm rms}]^2 \equiv [<\tilde{n}_\theta(t)>_{\rm rms}]^2 + [<\tilde{n}_r(t)>_{\rm rms}]^2 . \qquad (4.8)$$

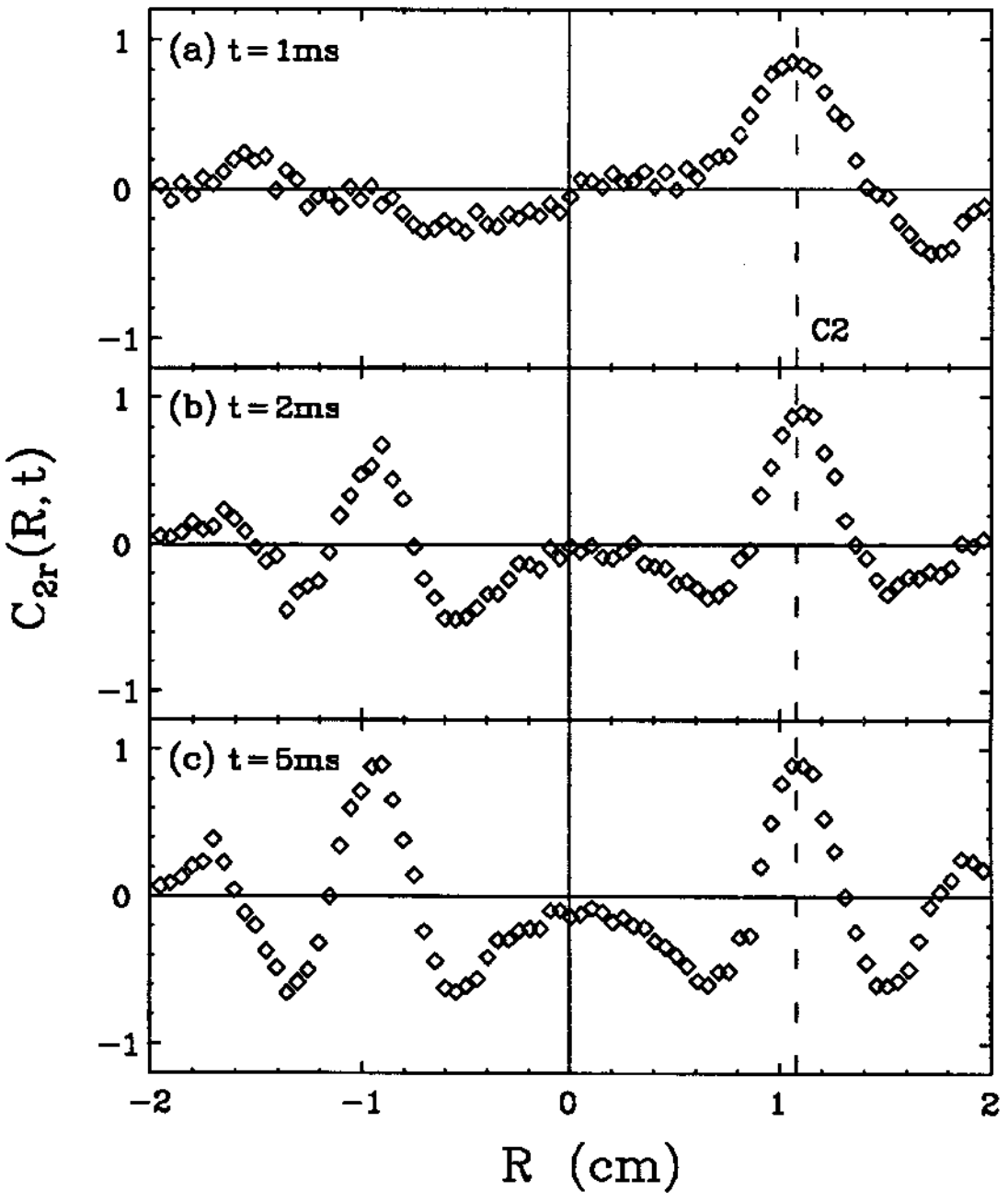

Figure 4.12: Correlation function $C_{2r}(R,t)$ at 3 times of the $l=1$ evolution. (a) $t=1$ ms; (b) $t=2$ ms; (c) $t=5$ ms. The dashed line is the location of the fixed collector C2.

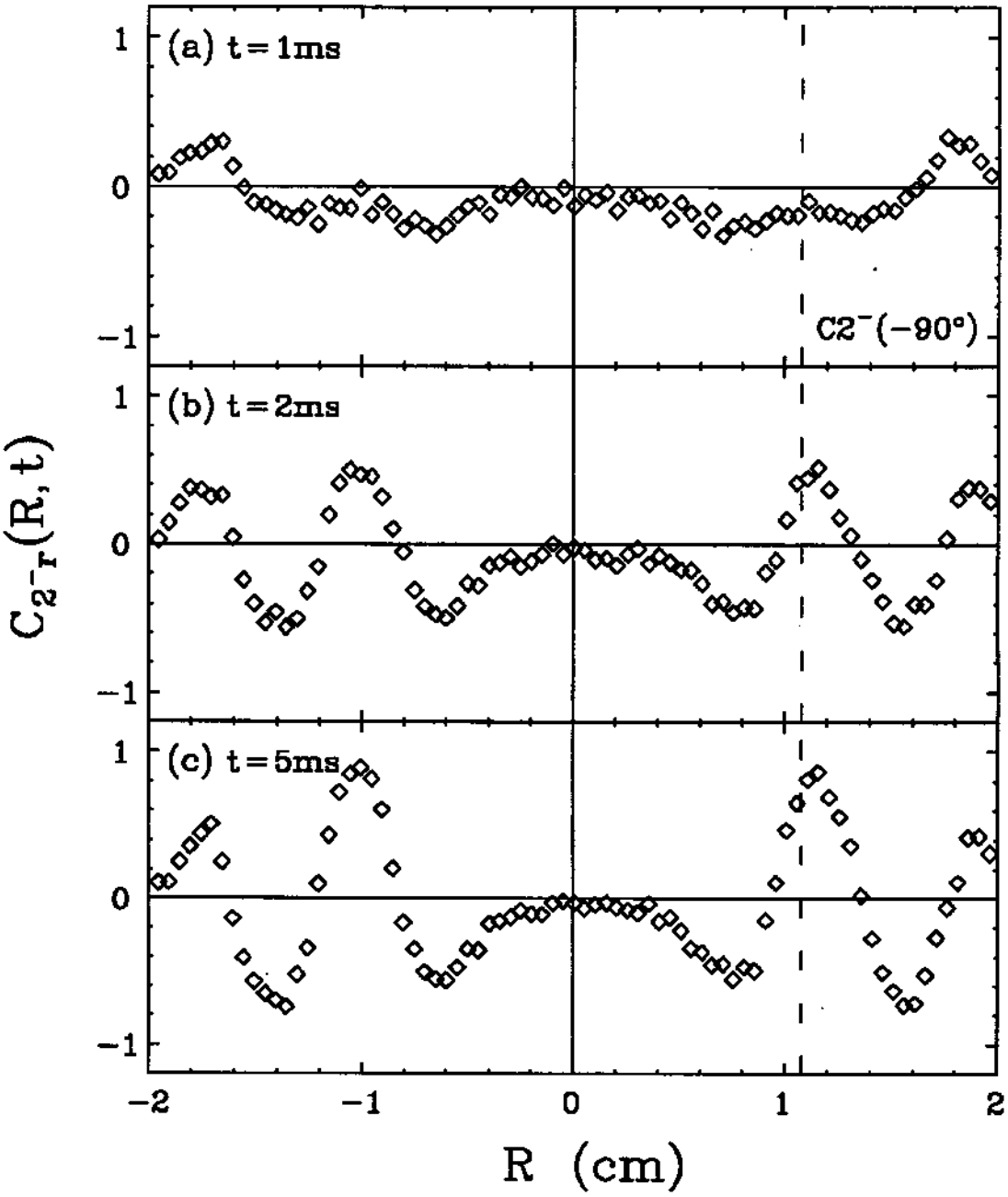

Figure 4.13: Correlation function $C_{2^-r}(R,t)$ at 3 times of the $l=1$ evolution. (a) $t=1$ ms; (b) $t=2$ ms; (c) $t=5$ ms. The dashed line is the radial location of the fixed collector $C2^-$ ($\theta_{2^-}=-90°$).

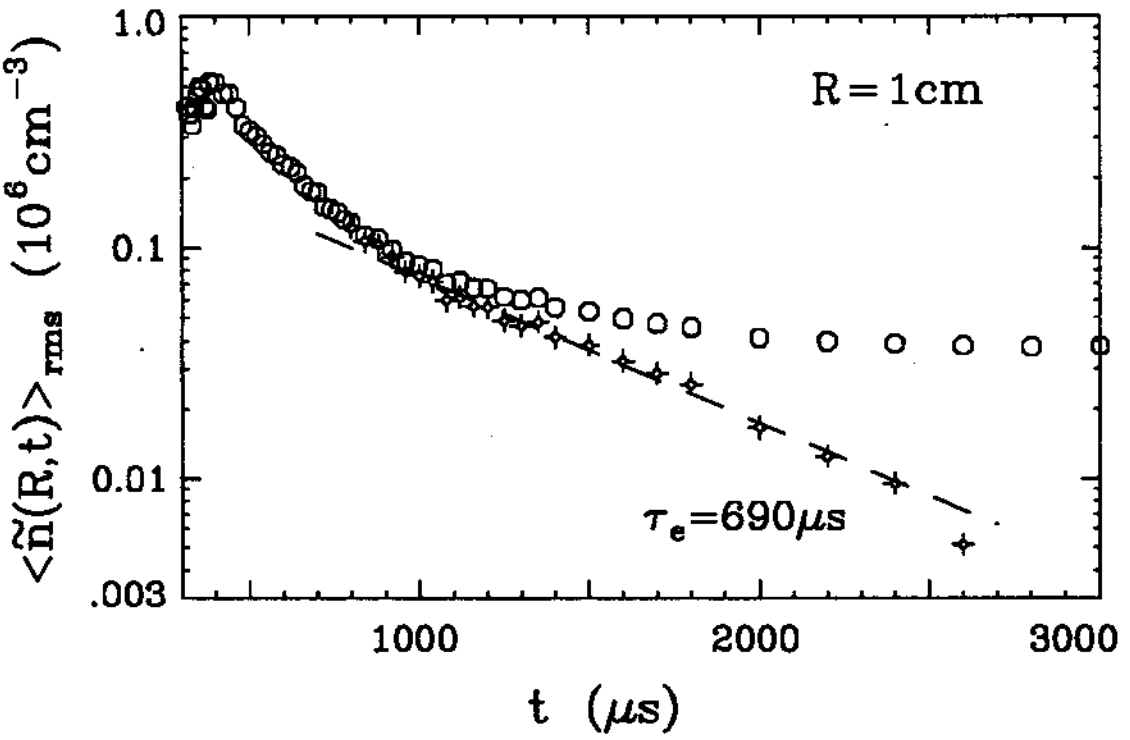

Figure 4.14: Exponential decay of the θ-fluctuations during the column axisymmetrization (the $l = 1$ sequence). Star symbols represent data after the asymptotic level has been subtracted as in Equation (4.8), and the dashed line is the least-square-fit.

Figure 4.14 shows the decay of the fluctuation level at $R = 1\,\mathrm{cm}$, corresponding to the axisymmetrization process illustrated in Figures 4.11–4.13. Circle symbols represent the measured $<\hat{n}(t)>_{\mathrm{rms}}$, while star symbols are the calculated late-time decaying component $<\tilde{n}_\theta(t)>_{\mathrm{rms}}$ from Equation (4.8). The exponential least-square-fit to the $<\tilde{n}_\theta(t)>_{\mathrm{rms}}$ data is plotted as the dashed line, with an e-folding decay time $\tau_e \simeq 690\ \mu\mathrm{s}$. The decay rate $\gamma_e \equiv 1/\tau_e$ is presumably determined by the radial drift speed of the holes, as discussed above. Note that the exponential fit to the decaying fluctuation component normally does not work very well for the entire relaxation, as can be seen from Figure 4.14. In fact, power law fit $<\tilde{n}_\theta(t)>_{\mathrm{rms}} \sim t^{-\xi}$, with $\xi = 1.5$–

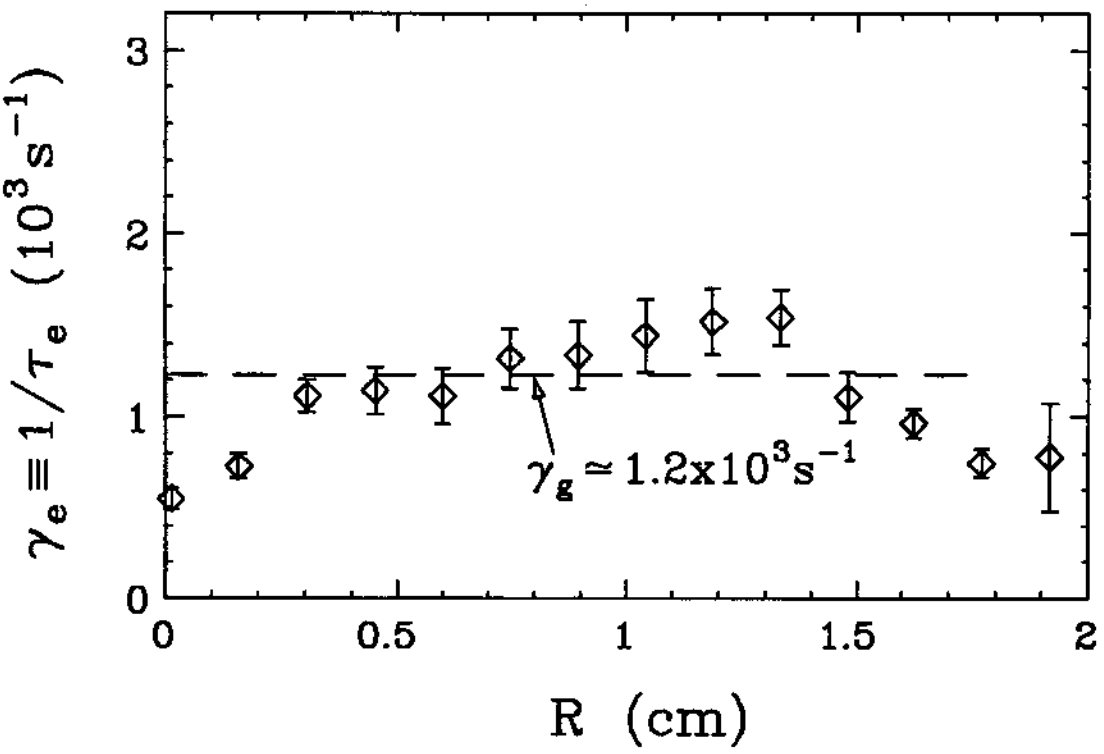

Figure 4.15: Measured exponential decay rate γ_e versus radius R for the $l = 1$ evolution, with the global decay rate γ_g being plotted as the dashed line.

3.0, appears to do a better job in some cases. Therefore, the exponential decay rate γ_e should be viewed simply as a characteristic relaxation time scale.

The same decomposition and exponential fitting procedure has been performed on data measured at various radial positions. The resulting radial dependence of the decay rate is shown in Figure 4.15. Except for the center and the very edge of the column, the measured decay rate γ_e does not depend strongly on the radial position, even though the background rotational shear has quite large radial variations (see e.g., Figure 4.5). Experimentally, this is also true for many other columns with various initial conditions.

The global decay rate γ_g characterizes the overall relaxation, and is calculated

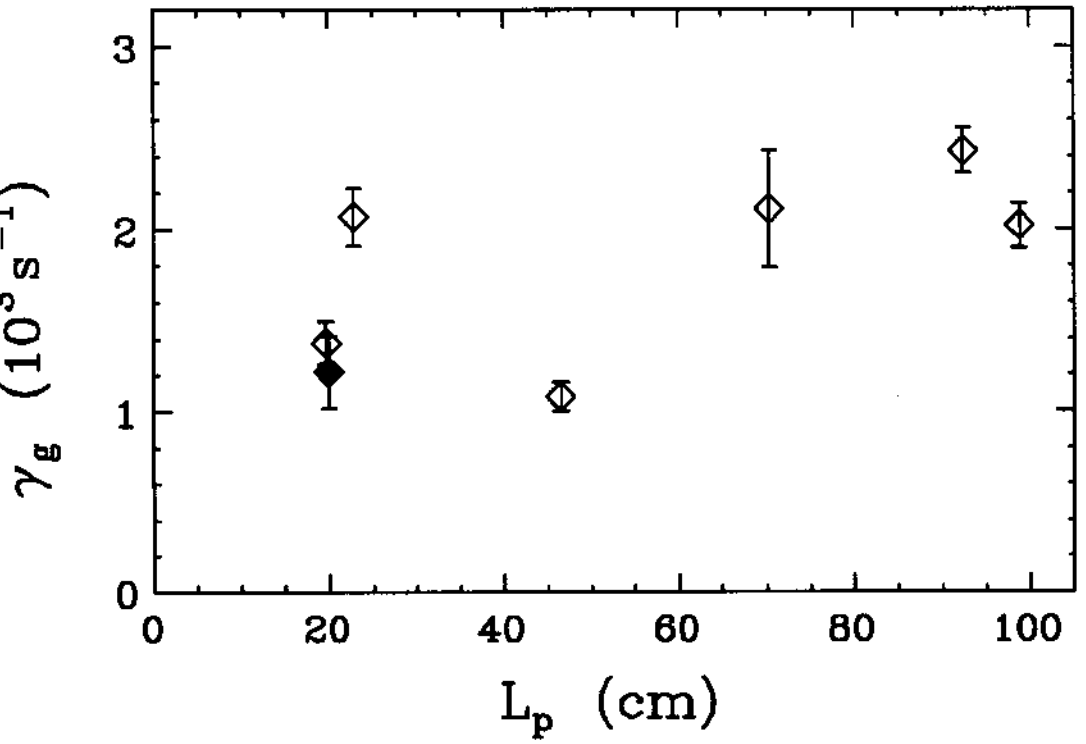

Figure 4.16: Measured global decay rate γ_g versus axial length L_p, for columns with approximately the same initial radial profile.

by decomposing and fitting the globally integrated fluctuation level

$$< \tilde{n}_g(t) >_{\rm rms} \equiv 2\pi R_w^2 \int dr\, r\, < \tilde{n}(r,t) >_{\rm rms} \ .$$

The global decay rate γ_g averages out the radial dependence of the local $\gamma_e(r)$, and generally gives a better exponential fit. This decay rate is plotted as the horizontal dashed line in Figure 4.15.

Similarly, γ_g rates for other evolutions with different initial conditions have been calculated, and scaling laws with various plasma parameters such as column axial length L_p and magnetic field B_z have been measured. Ideally, one has to ensure that when a plasma parameter is varied, other parameters remain the same, especially for the detailed initial 2D density distribution. However, this can only be achieved

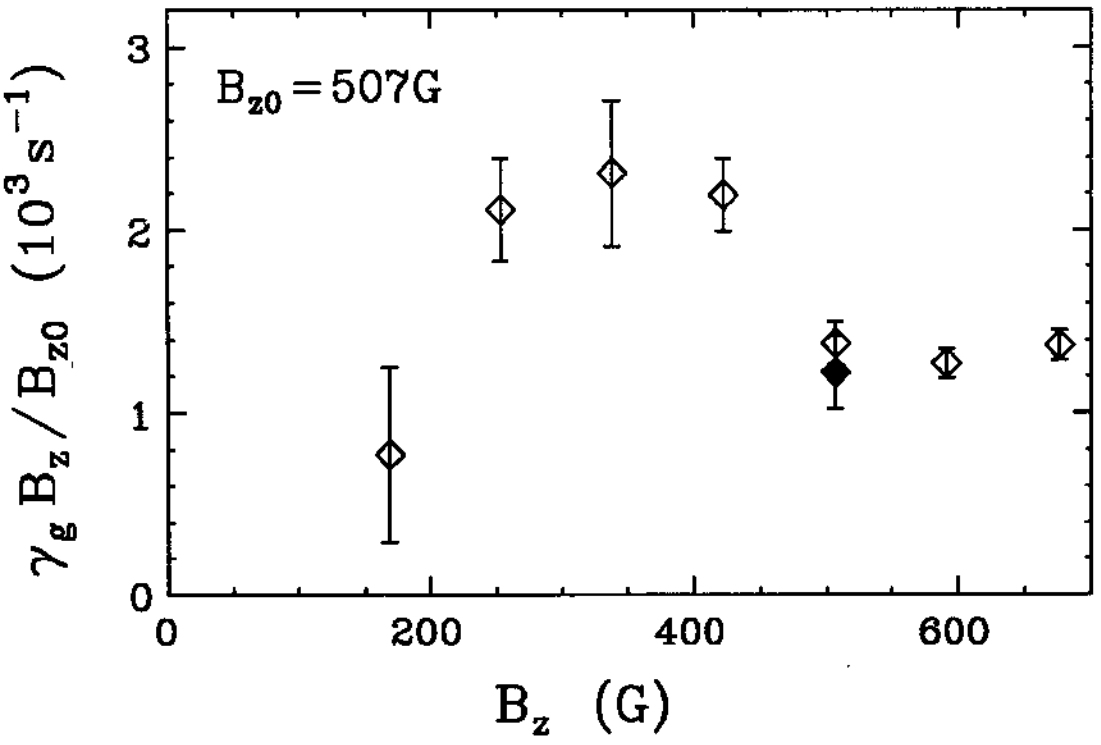

Figure 4.17: Scaled global decay rate $\gamma_g B_z/B_{z0}$ versus magnetic field B_z, for columns with approximately the same initial radial profile.

approximately in the experiments, due to the uncontrollable factors involved in the electron column preparation process.

Figure 4.16 shows the axial length dependence of γ_g for columns with initial conditions similar to the one shown in Figure 4.3. The γ_g calculated for the evolution of Figure 4.3 is shown as the solid symbol. Here, L_p ranges from 20 cm $\leq L_p \leq$ 80 cm; the global decay rate γ_g varies up to a factor of two, but does not show a simple dependence on L_p. In fact, if the relaxation were dominated by end effects, one would expect to see a strong dependence of γ_g on L_p. This suggests that the relaxation processes, including the radial outward drift of the density holes are basically 2D in nature.

The dependence of γ_g on the axial magnetic field B_z has also been measured

in the same way. Here, the drift-Poisson equations predict that all the dynamical time scales are directly proportional to the magnetic field B_z, so the scaled global decay rate $\gamma_g B_z/B_{z0}$ should be independent of B_z , where constant field $B_{z0} = 507\,\mathrm{G}$. Figure 4.17 shows $\gamma_g B_z/B_{z0}$ versus B_z, where B_z ranges from $170\ \mathrm{G} \leq B_z \leq 640\ \mathrm{G}$. The measured scaled global decay rate changes by a factor of two, with no systematic dependence on B_z. Again, the measurements are consistent with 2D $\mathbf{E}\times\mathbf{B}$ dynamics.

Chapter 5

Meta-Equilibrium State of 2D Turbulence

5.1 Overview

The relaxation process of 2D turbulence is generally complex, with many intriguing features as illustrated in Chapter 4. After the turbulence fully relaxes and equilibrates, however, it is tempting to expect that the equilibrium is determined only by the conserved quantities of the motion, independent of the details of the relaxation. This idea works well in systems having many degrees of freedom, such as an ideal gas, which always relaxes to its Maxwellian thermal equilibrium. Here, I consider the equilibrium state of 2D turbulence, which it is presumably reached through inviscid, nonlinear interactions of the turbulent flow. This 2D equilibrium persists for over 10^4 column bulk rotations until dissipation drives the system toward its final 3D thermal equilibrium [22, 25]. Owing its long but finite lifetime, this 2D equilibrium is called the meta-equilibrium state of 2D turbulence.

In this chapter, I present quantitative experimental measurements of the meta-equilibrium state, for comparison with the theoretical predictions of various models. Section 5.2 introduces several theories of 2D meta-equilibrium state. The point vortex and continuous fluid maximum entropy theories are within the framework of statistical mechanics applied to the configurational space of 2D flows. In

contrast, the global minimum enstrophy model follows directly from the "selective decay" hypothesis based largely on physical intuition. Here, I develop a "restricted" minimum enstrophy model appropriate to the experimental constraints of density being non-negative and monotonic in radius. These models are examined in detail, laying the foundation for further improvements and generalizations.

Section 5.3 describes the experimental measurements of the long-lasting meta-equilibrium column. It is shown that between the initial and meta-equilibrium states, the number of electrons (circulation), angular momentum (angular impulse), and electrostatic energy (kinetic energy) are well conserved during the evolution. In contrast, less robust invariants, such as the enstrophy and mean-field entropy, vary significantly. This variation is apparently due to dissipation or measurement coarse-graining of structures at fine scales generated by the strong turbulence. I also find that the measured meta-equilibrium density (vorticity) profiles exhibit close agreement with predictions of the restricted minimum enstrophy model, while differing substantially from maximum entropy predictions. Furthermore, I examine the small-amplitude ($\sim 2\%$), shot-to-shot variations observed in the meta-equilibrium profiles, and the effects of the relaxation dynamics on the meta-equilibrium state. In Section 5.4, I discuss the gradual decay of the meta-equilibrium state caused by the microscopic "viscous" effects and external particle transport. These 3D processes are beyond the scope of this work.

5.2 Theories of Meta-Equilibrium State

Theoretical efforts to predict the meta-equilibrium state date back to 1940s, when Onsager published his pioneering work on the statistical equilibrium of a point vortex gas [70]. To derive the predictions for the meta-equilibrium state, theories generally propose variational principles, such as the maximization of entropy and

minimization of enstrophy, based on certain physical insights on the relaxation dynamics.

Experimentally, meta-equilibrium states resulting from initially hollow columns are axisymmetric, with monotonically decreasing density profiles. Consequently, the theoretical models discussed in this section all treat equilibria that have only radial dependence. These four theories are

- point vortex maximum entropy theory,
- continuous fluid maximum entropy theory,
- global minimum enstrophy theory,
- restricted minimum enstrophy theory.

Here, I develop the restricted minimum enstrophy theory to apply to the particular experimental situation. Connections between some of these models have been explored theoretically [59, 26]; and in some cases, computer simulations have been performed to test the validity of these ideas [88, 91, 61, 59]. However, to our best knowledge, they have not previously been quantitatively tested in experiments.

5.2.1 Point Vortex Maximum Entropy Theory

The point vortex maximum entropy model derives its prediction by maximizing the mean-field entropy of a point vortex gas. A comprehensive survey of this approach was given by Smith, with references to most of the important developments [85]. This compressible point vortex gas serves as an approximation to a real turbulent fluid. Here, one assumes that the 2D turbulence is sufficiently violent that vorticity structures are being shredded into small pieces which wander ergodically over the configurational space. As a result, the statistical equilibrium of the flow is

merely the maximum entropy state of this point vortex gas, subject to constraints of fixed total circulation, angular momentum, and kinetic energy.

Mathematically, the entropy of a point vortex gas is the mean-field entropy S defined in Section 3.2. The maximum entropy state can therefore be calculated from the functional derivation,

$$\delta(S - \alpha_P P_\theta - \alpha_H H_\phi) = 0 \,. \tag{5.1}$$

Here, α_P and α_H are Lagrange multipliers embodying conservation of angular momentum and energy, and the conservation of circulation is implicitly satisfied by the normalization of the integrals. In general, a relation between the equilibrium density $n_{\rm eq}$ and potential $\phi_{\rm eq}$ can be derived from Equation (5.1),

$$n_{\rm eq} = C \exp[\alpha_H(\phi_{\rm eq}/\phi_0) + \alpha_P r^2] \,. \tag{5.2}$$

The density and potential must be related by Poisson equation, giving

$$\frac{1}{r}\frac{d}{dr}[r\frac{d\phi_{\rm eq}(r)}{dr}] = 4\pi e R_w^2 n_{\rm eq}(r) \,, \tag{5.3}$$

with wall boundary condition $\phi_{\rm eq}(r=1) = 0$. The Lagrange multipliers and the constant C are determined from the values of N_L, P_θ, and H_ϕ self-consistently by plugging the solution $n_{\rm eq}$ into the definitions of these fixed integrals.

5.2.2 Continuous Fluid Maximum Entropy Theory

Strictly speaking, the point vortex model can only be valid in the limit where the vorticity is sparsely distributed and concentrated in discrete vortices. In this case, one obtains a statistical equilibrium analogous to the Boltzmann distribution in thermal dynamics. The more realistic continuous fluid approach was developed by Lynden-Bell in the context of collisionless relaxation of self-gravitating galaxies [48]. Here, the 2D incompressible flow is broken into small non-overlapping fluid elements

with arbitrary vorticity. A generalized entropy functional gives the statistical equilibrium, which is essentially the same as the Fermi distribution [48, 58, 78, 59, 79].

This approach conserves N_L, P_θ, and H_ϕ, and also conserves all the moments of vorticity $\mathcal{Z}_m$ until averaging is performed over the fine scales. That is, the fractional area $A(n')$ is conserved, where $A(n')dn'$ is the area occupied by fluid elements with vorticity between n' and $n' + dn'$. The macroscopic equilibrium state is obtained in terms of equilibrium probability function $\rho_{\rm eq}(\mathbf{x}, n')$, which represents the probability of having density n' at location $\mathbf{x}$. The statistical analysis gives [59]

$$\rho_{\rm eq}(\mathbf{x}, n') = \frac{\exp\{-\beta n'[-\phi_{\rm eq}(\mathbf{x}) + \gamma r^2] - \alpha(n')\}}{\int_{-\infty}^{\infty} dn'' \exp\{-\beta n''[-\phi_{\rm eq}(\mathbf{x}) + \gamma r^2] - \alpha(n'')\}}\,, \tag{5.4}$$

where β, γ, and function $\alpha(n')$ are parameters to be determined from the conserved quantities.

The mean density $n_{\rm eq}(r)$ is calculated through the general relation

$$n_{\rm eq}(r) = \int_{-\infty}^{\infty} dn'\, n' \rho_{\rm eq}(r, n')\,. \tag{5.5}$$

Again, the density and potential must satisfy the Poisson Equation (5.3). Normally, Equation (5.5) leads to a n–ϕ relationship analogous to that of the Fermi distribution. The parameters are determined numerically from P_θ, H_ϕ, and $A(n')$ of the initial hollow density distribution. In practice, the measured initial $A(n')$ is approximated by a polynomial fit to the data [87], such as, $A(n') \simeq A_0 + A_1 n' + A_1 n'^2 + \ldots$, to facilitate the determination of the parameter function $\alpha(n')$ through the equation

$$A(n') = 2 \int dr\, r \rho_{\rm eq}(r, n')\,, \tag{5.6}$$

which follows from the definition of $\rho_{\rm eq}(r, n')$.

One conclusion of this theory is worth mentioning: at the macroscopic spatial scales, the statistical equilibrium is predicted to be completely fluctuationless as time approaches infinity [59]. This point can be readily tested in the experiment

by comparing the initial and meta-equilibrium shot-to-shot statistical variations. If the system has indeed equilibrated to the continuous fluid maximum entropy state, the shot-to-shot variation level should not be too much higher than that of the well-controlled initial state, provided that the equilibrium does not depend on the conserved quantities very sensitively.

Another comment concerns the fact that the statistical (maximum entropy) theories postulate that the meta-equilibrium state is intimately associated with the ergodicity of the flow in 2D configurational space. This assumption can not be proven from the true 2D dynamics, although attempts have been made to formulate a H-theorem for the dynamical relaxation to the most probable state [79]. Ultimately, the validity of this idea must be quantitatively tested in experiments and/or accurate computer simulations.

5.2.3 Selective Decay Hypothesis

In principle, inviscid 2D dynamics conserves the vorticity associated with each Lagrangian fluid elements. However, as the turbulent flow evolves, more and more fine-scale motions with complex spatial structures are created. Consequently, any slight dissipation or measurement coarse-graining will cause variations in some ideal invariants.

Experimentally, the total number of electrons (circulation) and angular momentum are well conserved, and the energy is nearly conserved (see Section 5.3); in contrast, higher moment integrals (fragile invariants) changes significantly during the evolution. In a 2D statistical spectral theory, Kraichnan argues that the only important fragile integral is the enstrophy. This is because that it is a quadratic function of vorticity, and therefore independent of the high wavenumber cut-off which must be used in any practical spectral analyses [39, 40, 41]. Carnevale and Frederiksen suggest that the uniqueness of enstrophy is probably connected to the complicated

phase space topology of the higher Z_m constraints [10]. However, there is still no universally accepted justification for this choice of enstrophy as the uniquely important fragile invariant [59].

Based on this physical insight, the selective decay relaxation mechanism conjectures that the meta-equilibrium state of 2D turbulence results from unequal decay of the robust invariants (such as energy) and the enstrophy [8, 54, 35]. Therefore, the proposed 2D meta-equilibrium is simply the minimum enstrophy state constrainted by the fixed robust invariants of the system [8, 43, 36]. Again, this hypothesis can not be proven from the dynamical equation. However, similar conjectures have been successfully applied to experiments on turbulent MHD plasma systems [94, 62].

In this model, the equilibrium density distribution $n_{\rm eq}(r,\theta)$ is obtained by minimizing Z_2 subject to the constraints that N_L, P_θ, and H_ϕ remain fixed. It follows that

$$\delta(Z_2 - \alpha_P P_\theta - \alpha_H H_\phi) = 0\,, \tag{5.7}$$

where the N_L constraint is implicitly included in the normalizations. This functional variation leads to an equilibrium n–ϕ relation,

$$n_{\rm eq}(r,\theta) = -n_0[\alpha_H \phi_{\rm eq}(r,\theta)/\phi_0 + \alpha_P r^2] + C\,, \tag{5.8}$$

where $n_0 \equiv N_L/R_w^2$ and $\phi_0 \equiv eN_L$ are the characteristic density and potential respectively, and C is a constant. Note that $n_{\rm eq}$ is not a function of $\phi_{\rm eq}$ alone, due to the angular momentum constraint in the laboratory frame. However, by choosing a rotating frame with proper angular velocity, the r^2 term in Equation (5.8) can be cancelled out, allowing a simple linear n–ϕ relation [69].

5.2.4 Minimum Enstrophy Vortices in a Cylinder

The axisymmetric minimum enstrophy states can be derived analytically for magnetized electron columns bounded by conducting cylinders. Note that here, the

conducting cylinders provide a complete neutralizing shield, not found in open flows; as a result, one needs not to impose any *ad hoc* boundary conditions to avoid energy divergence [43].

Minimum enstrophy radial profiles are derived for the global model, and for a "restricted" model which requires that density remains positive everywhere and is monotonically decreasing. In both models, I solve for the axisymmetric equilibrium profile $n_{\rm eq}(r)$ by combining the minimum enstrophy n–ϕ relation Equation (5.8) with Poisson Equation (5.3). This gives

$$\frac{d^2 n_{\rm eq}}{dr^2} + \frac{1}{r}\frac{dn_{\rm eq}}{dr} + \beta(n_{\rm eq} + \gamma) = 0\,, \tag{5.9}$$

with the solution

$$n_{\rm eq}(r) = \alpha J_0(\beta^{\frac{1}{2}} r) - \gamma\,, \tag{5.10}$$

where J_0 is the zeroth order Bessel function. The parameters (α, β, γ) and the minimum enstrophy $Z_2^{\rm min} \equiv Z_2[n_{\rm eq}]$ are completely determined by the integral invariants (N_L, P_θ, H_ϕ).

For the global minimum enstrophy model, $n_{\rm eq}(r)$ from Equation (5.10) is used in the entire region of $0 \le r \le 1$, since no additional requirement for density and boundary is imposed. For typical values of (N_L, P_θ, H_ϕ) of the initially hollow columns, this $n_{\rm eq}$ profile goes negative at large radii and is finite at the wall; furthermore, it generally is not monotonically decreasing in radius. Clearly, negative electron density would be unphysical, and non-monotonic profiles would be unstable to diocotron instabilities, indicating that the global minimum enstrophy state may be non-axisymmetric and/or off-axis away from the cylinder center [43].

These difficulties can be overcome by requiring that $n_{\rm eq}(r)$ follows the solution of Equation (5.10) until it reaches zero at some radius r_0, after which $n_{\rm eq} = 0$. This

restricted minimum enstrophy model yields a solution

$$n_{eq}(r) = \begin{cases} \alpha[J_0(\beta^{\frac{1}{2}} r) - J_0(\beta^{\frac{1}{2}} r_0)] & 0 \le r \le r_0 \\ 0 & r_0 < r \le 1 \,, \end{cases} \tag{5.11}$$

where (α, β, r_0) and $Z_2^{\min}$ are again determined from the measured (N_L, P_θ, H_ϕ), with no other adjustable parameters.

This added requirement is mainly based on the experimental observation that the meta-equilibrium columns considered here are normally confined in a core region of the cylinder, completely isolated from the wall. Mathematically, the solution of Equation (5.11) can be derived more rigorously by taking the following generalized functional variation

$$(\frac{\delta}{\delta n} + \frac{d}{dr_0})\{\int_0^{r_0} dr\, \pi r[(\frac{n}{n_0})^2 - 2\alpha_P(1-r^2)(\frac{n}{n_0}) + \alpha_H(\frac{\phi}{\phi_0})(\frac{n}{n_0})]\} =$$

$$\int_0^{r_0} dr\, \frac{2\pi r}{n_0}[(\frac{n}{n_0}) - \alpha_P(1-r^2) + \alpha_H(\frac{\phi}{\phi_0})] = 0 \,, \tag{5.12}$$

where the d/dr_0 term vanishes, since density $n_{eq}(r_0)$ is assumed to be zero. The restricted minimum enstrophy solution Equation (5.11) then follows directly from Equation (5.12).

The meta-equilibrium potential $\phi_{eq}(r)$ follows from n_{eq} and the boundary condition $\phi_{eq}(r=1) = 0$, as

$$\phi_{eq}(r) = \begin{cases} -\frac{4\pi e R_w^2 \alpha}{\beta}\{[J_0(\beta^{\frac{1}{2}} r) - J_0(\beta^{\frac{1}{2}} r_0)] + \frac{\beta J_0(\beta^{\frac{1}{2}} r_0)}{4}(r^2 - r_0^2)\} & \\ \qquad + 2\phi_0 \ln r_0 & 0 \le r \le r_0 \\ 2\phi_0 \ln r & r_0 < r \le 1 \,. \end{cases} \tag{5.13}$$

Because $\phi_{eq}(r)$ is a monotonically increasing function of r, the functional relation $n_{eq}(\phi_{eq})$ can be derived and compared with experimental data.

Applying $n_{eq}(r)$ in Equation (5.11) to the N_L and P_θ integrals, α and β can be expressed in terms of the scaled cut-off radius $\hat{r}_0 \equiv \beta^{\frac{1}{2}} r_0$ by using the mathematical

identities listed in Appendix D,

$$\alpha(\hat{r}_0) = \frac{n_0}{2\pi(1-P_\theta)\hat{r}_0^2 J_2(\hat{r}_0)}[(\hat{r}_0^2-8)+\frac{2\hat{r}_0 J_1(\hat{r}_0)}{J_2(\hat{r}_0)}] \tag{5.14}$$

$$\beta(\hat{r}_0) = \frac{1}{2(1-P_\theta)}[(\hat{r}_0^2-8)+\frac{2\hat{r}_0 J_1(\hat{r}_0)}{J_2(\hat{r}_0)}]\,. \tag{5.15}$$

The scaled cut-off radius $\hat{r}_0$ can be solved numerically from the energy integral of the equilibrium profile. Using the solutions for the equilibrium density and potential, the energy can be expressed as a function of P_θ and $\hat{r}_0$, $F_H(P_\theta,\hat{r}_0)$. Parameter $\hat{r}_0$ will have to satisfy $F_H(P_\theta,\hat{r}_0)=H_\phi$. It turns out that function $F_H(P_\theta,\hat{r}_0)-H_\phi$ depends explicitly *only* on the scaled cut-off radius $\hat{r}_0$ and the excess energy, $H_\phi^{\rm exc}\equiv H_\phi - H_\phi^{\rm min}$, with

$$H_\phi^{\rm min}=\frac{1}{4}-\frac{\ln 2(1-P_\theta)}{2} \tag{5.16}$$

being the minimum energy possible for a column with fixed N_L and P_θ, which occurs for a uniform density profile. Analytically, this dependence can be expressed as

$$F_H(P_\theta,\hat{r}_0)-H_\phi = G(\hat{r}_0)-H_\phi^{\rm exc}\,, \tag{5.17}$$

where $G(\hat{r}_0)$ is a universal function of $\hat{r}_0$ without parameters.

Figure 5.1 shows a typical solution for $H_\phi^{\rm exc}=1\times10^{-2}$, with $\hat{r}_0\simeq 2.87$ in the region $0\le\hat{r}_0\le j_{1,1}$ ($j_{1,1}=3.8317$ is the first root of J_1, corresponding also to the minimum of J_0), within which the first zero of J_0 lies. The second root is discarded since it permits negative density, and thus is not physical. From Figure 5.1, it is clear that in order to derive a self-consistent analytical solution, $H_\phi^{\rm exc}$ must satisfy a prerequisite,

$$H_\phi^{\rm exc}\le\frac{6}{j_{1,1}^2}+\frac{1}{2}\ln(1-\frac{8}{j_{1,1}^2})\,. \tag{5.18}$$

Furthermore, the sufficient condition

$$P_\theta\ge\frac{1}{2}+\frac{4}{j_{1,1}^2} \tag{5.19}$$

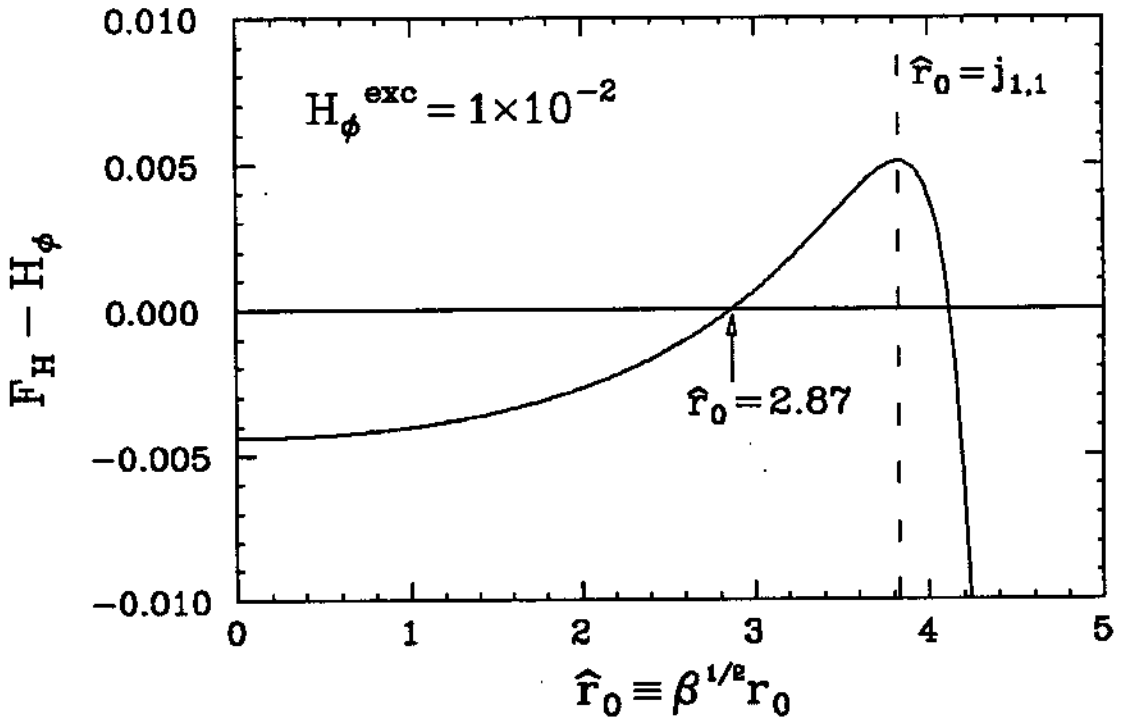

Figure 5.1: Solving for parameters in the restricted minimum enstrophy model. Analytical function $F_H - H_\phi$ is plotted versus $\hat{r}_0$, with one root being found between 0 and $j_{1,1}$.

ensures that the cut-off radius $r_0 \leq 1$, i.e., within the boundary wall. Of course, when Equation (5.18) is not satisfied, the restricted minimum enstrophy state still exists — it simply no longer occurs as a local extremum for the multi-dimensional variation Equation (5.7), and must be solved through more advanced numerical means [24]. Furthermore, preliminary calculation suggests that near the upper excess energy limit in Equation (5.18), a bifurcation of solution may occur, resulting in an off-axis state with slightly lower enstrophy [88].

At the upper excess energy limit,

$$r_0 = [\frac{2}{1 - 8/j_{1,1}^2}(1 - P_\theta)]^{\frac{1}{2}} ,$$

and the density profile is an up-shifted Bessel function. When the excess energy

satisfies

$$H_\phi^{\rm exc} = H_{\phi 0}^{\rm exc} = \frac{5}{24} - \frac{1}{2}\ln\frac{3}{2}\,, \tag{5.20}$$

the equilibrium density profile becomes a parabola,

$$n_{\rm eq}(r) = \begin{cases} \dfrac{2n_0}{\pi r_0^2}\,[1-(\dfrac{r}{r_0})^2] & 0 \le r \le r_0 \\ 0 & r_0 < r \le 1\,, \end{cases}$$

with $r_0 = [3\,(1-P_\theta)\,]^{\frac{1}{2}}$ and $Z_2^{\rm min} = 2\,/\,[9\pi(1-P_\theta)\,]$.

For $H_\phi^{\rm exc} < H_{\phi 0}^{\rm exc}$, α and β are both negative, Equation (5.11) becomes (see Appendix D)

$$n_{\rm eq}(r) = \begin{cases} \alpha[I_0(|\beta|^{\frac{1}{2}}r) - I_0(|\beta|^{\frac{1}{2}}r_0)] & 0 \le r \le r_0 \\ 0 & r_0 < r \le 1\,, \end{cases}$$

where I_0 is the zeroth order modified Bessel function. As $H_\phi^{\rm exc} \to 0$, the minimum enstrophy state approaches the uniform density column of radius $r_0 = [2(1-P_\theta)]^{\frac{1}{2}}$, with $Z_2^{\rm min} = 1\,/\,[4\pi(1-P_\theta)\,]$.

Generally speaking, the minimum enstrophy value $Z_2^{\rm min}$ depends both on P_θ and H_ϕ; under this restricted model, however, $Z_2^{\rm min}$ can be rescaled so that the scaled minimum enstrophy $\hat{Z}_2^{\rm min} \equiv 4\pi(1-P_\theta)Z_2^{\rm min}$ is only a function of the excess energy $H_\phi^{\rm exc}$. Here, the factor 4π is chosen so that a uniform column would have $\hat{Z}_2^{\rm min} = 1$. When the analytical solution exists, this dependence can be seen from the equation

$$\begin{aligned} \hat{Z}_2^{\rm min}(\hat{r}_0) \;\; = \;\; & [\frac{(\hat{r}_0^2-8)J_2(\hat{r}_0) + 2\hat{r}_0 J_1(\hat{r}_0)}{\hat{r}_0^3 J_2(\hat{r}_0)}] \times \\ & \{\hat{r}_0[2J_0^2(\hat{r}_0) + J_1^2(\hat{r}_0)] - 4J_0(\hat{r}_0)J_1(\hat{r}_0)\}\,, \end{aligned} \tag{5.21}$$

where $\hat{r}_0$ is in turn determined by $H_\phi^{\rm exc}$ alone. In Section 5.3, this single-variable dependence for the scaled minimum enstrophy is examined in detail from the experimental data.

t	$n_{\max}$	N_L	P_θ	H_ϕ	Z_2	Z_3	Z_4	S
20μs	+4.1%	+1.2%	+1.5%	+3.4%	+22%	+45%	+68%	-0.082
5ms	3.05×10^6	1.77×10^7	0.861	0.896	0.510	0.396	0.373	0.087
50ms	-1.0%	-0.1%	-0.3%	-1.0%	-1.8%	-3.3%	-4.8%	0.104

Table 5.1: Measured ideal 2D invariants at various times. Values at 5 ms are absolute; other values (except for S) are expressed as % changes from $t = 5$ ms.

5.3 Measurements of Meta-Equilibrium State

The long-lasting meta-equilibrium state resulting from the relaxation of 2D turbulence has been described briefly in Chapter 4, where the main topic was the dynamical process of the relaxation. In this section, I discuss the meta-equilibrium state in detail, and make quantitative comparisons with the theoretical predictions. Since the meta-equilibrium state is essentially stationary for over 10^4 bulk rotations, one only needs to consider its properties at a particular time after equilibration. Here, I take measurements at $t = 5$ ms for the $l = 1$ sequence to characterize the meta-equilibrium, and at $t = 50$ ms to verify that the meta-equilibrium is indeed stationary. The measurements at $t = 20$ μs characterize the initial condition.

5.3.1 Changes of Ideal 2D Invariants

I first consider the variations in the ideal 2D invariants between the initial and meta-equilibrium state. The evolution dominated by the $l = 1$ instability, discussed in Chapter 4, is used as an example. Radial density profiles of the initial and meta-equilibrium state are plotted in Figure 5.2 as cross and square symbols. The large-scale convective transport caused by the turbulent $\mathbf{E} \times \mathbf{B}$ drift dynamics is apparent.

Table 5.1 lists the ideal 2D invariants defined in Section 3.2, as calculated from the measured density profiles at $t = 20$ μs, 5 ms and 50 ms. For normalizations, the characteristic density n_0 and potential ϕ_0 are calculated using the measured N_L at $t = 5$ ms. Between $t = 20$ μs and $t = 5$ ms, N_L, P_θ, and H_ϕ drop by 4% or less,

probably due to systematic errors such as changes in column end shape. In addition, the peak density $n_{\max}$, which is a local ideal invariant, experiences a 4% drop after being transported from $r \simeq 0.4$ to the column center. In contrast, Z_2, Z_3, and Z_4 fall by more than 20%, and S increases by more than a factor of 2 while changing its sign from negative to positive. Note that since the entropy S has a logarithmic density dependence, its numerical value can be offset by an arbitrary constant, so its percentage change is meaningless. These results confirm that the experimental system is 2D-like and that the main dissipation in these columns occurs at fine scales, and is quite weak. Furthermore, all the ideal invariants (except S) remain essentially constant between $t = 5$ ms and 50 ms, providing added evidence for the longevity of the meta-equilibrium state in this system. The increase in S is mainly caused by the slight change of density profile near the column edge, where the logarithmic integrand contributes the most to the integral.

These integrals are calculated from the radial profiles of the mean density $< n(r,t) >$, so they do not include corrections due to shot-to-shot fluctuations. However, this does not cause any significant changes to the ideal invariants of the initial and meta-equilibrium states listed in Table 5.1. At $t = 20\ \mu$s, the perturbation is dominated by a single unstable $l = 1$ diocotron mode varying as $\tilde{n}^{(1u)}(r)\exp(i\theta)$, where $n^{(1u)}(r) \simeq \sqrt{2} < \tilde{n}(r) >_{\rm rms}$ is the mode eigenfunction. By carrying out the 2D r-θ integrals, it can be shown that the calculated N_L and P_θ do not change, since they depend linearly on density. Z_m and S change by insignificant amounts: for example, the enstrophy Z_2 is increased by

$$\pi \int dr\, r [\frac{< \tilde{n}(r) >_{\rm rms}}{n_0}]^2 ,$$

which is less than 1% for the given initial condition. The electrostatic energy H_ϕ is decreased by the negative energy of the diocotron mode, which is calculated to be less than 0.5% of the energy of the axisymmetric profile for $< \tilde{n}(r) >_{\rm rms} / < n(r) > \sim 5\%$

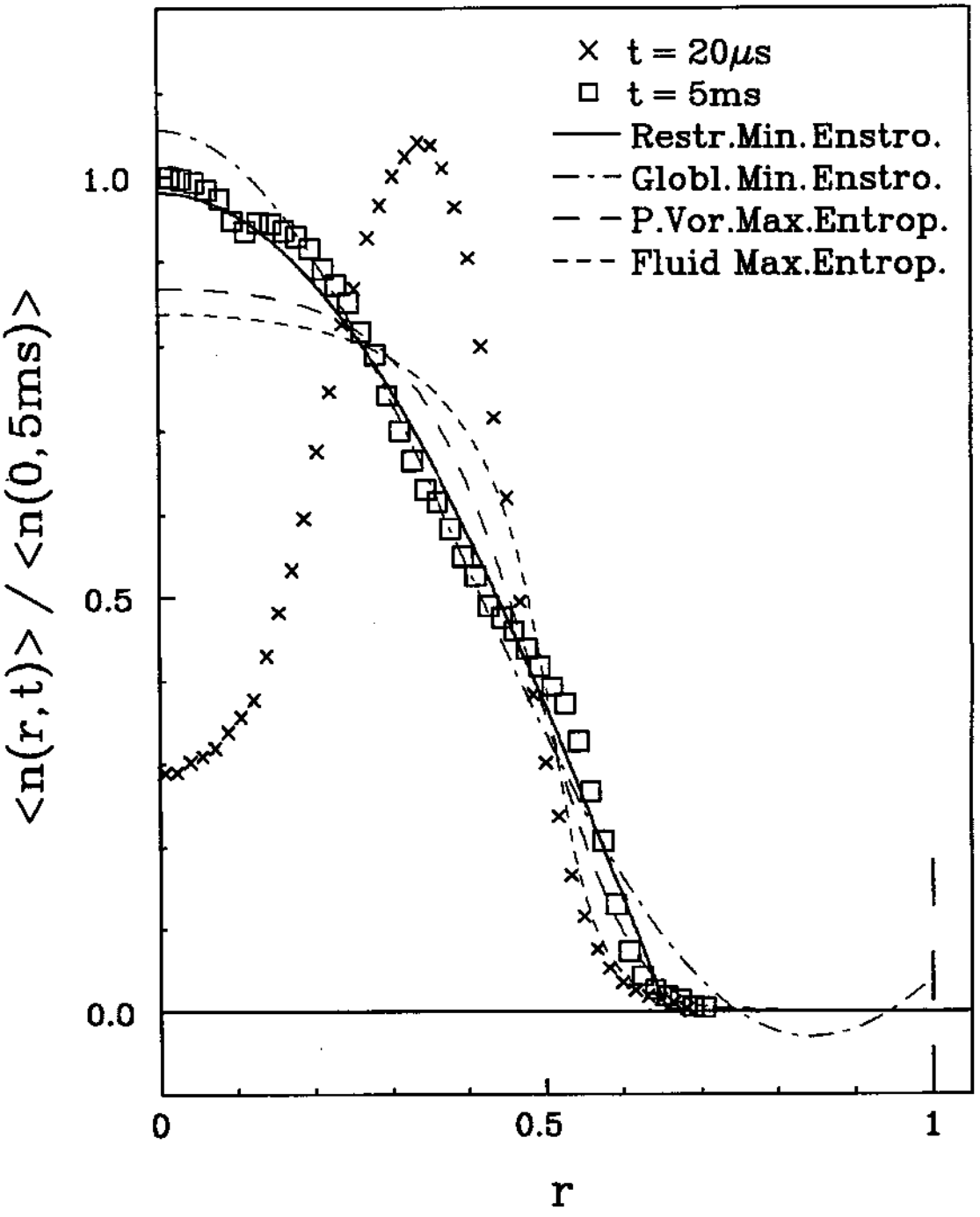

Figure 5.2: Measured radial density profiles of the initial and meta-equilibrium state, and theoretical predictions from the 4 models discussed.

by using the formula of Briggs *et al.* [9]. Finally, the peak density $n_{\max}$ (at $r = r_{\max}$) does not deviate much from the true value, for the reason that the measured fluctuation level is small at $r_{\max}$ (see Figure 4.3).

The measured fluctuations of the meta-equilibrium state are shown to be caused by the shot-to-shot variations in the axisymmetric radial density profile, as discussed in detail later in this section. Following the same kind of reasoning, one can show that the ideal invariants of the meta-equilibrium state listed in Table 5.1 are essentially unaffected by the profile variations, since the changes go like $[<\tilde{n}>_{\rm rms} / <n>]^2$ and the measured variation level is quite small ($\sim 2\%$). Take enstrophy Z_2 as an example; for shot i,

$$\begin{aligned} \Delta Z_2 \equiv Z_{2i} - Z_2 &= 2\pi \int dr\, r[\frac{<n(r)>}{n_0}][\frac{\tilde{n}_i(r)}{n_0}] + \pi \int dr\, r[\frac{\tilde{n}_i(r)}{n_0}]^2 \\ &\simeq \pi \int dr\, r[\frac{\tilde{n}_i(r)}{n_0}]^2 , \end{aligned} \tag{5.22}$$

where it is assumed that the varying component $\tilde{n}_i(r)$ (for shot i) is not correlated to the mean density $<n(r)>$ over radius, so that the first integral vanishes. The enstrophy difference therefore represents the integrated square density deviation between the two distributions. Note that the result expressed in Equation (5.22) can be applied to any two radial profiles provided that their differences are randomly distributed in radius. Fundamentally, the conclusions based on Table 5.1 are solid for the reason that many other initial and meta-equilibrium states display essentially the same changes even when the initial asymmetries are quite small.

5.3.2 Meta-Equilibrium Radial Profiles

The detailed meta-equilibrium density profile $<n(r)>$ is of special interest, since the various theories discussed earlier give definitive predictions that can be compared with the experimental data. Figure 5.2 shows the measured initial and meta-equilibrium radial density profiles compared to the four theoretical models.

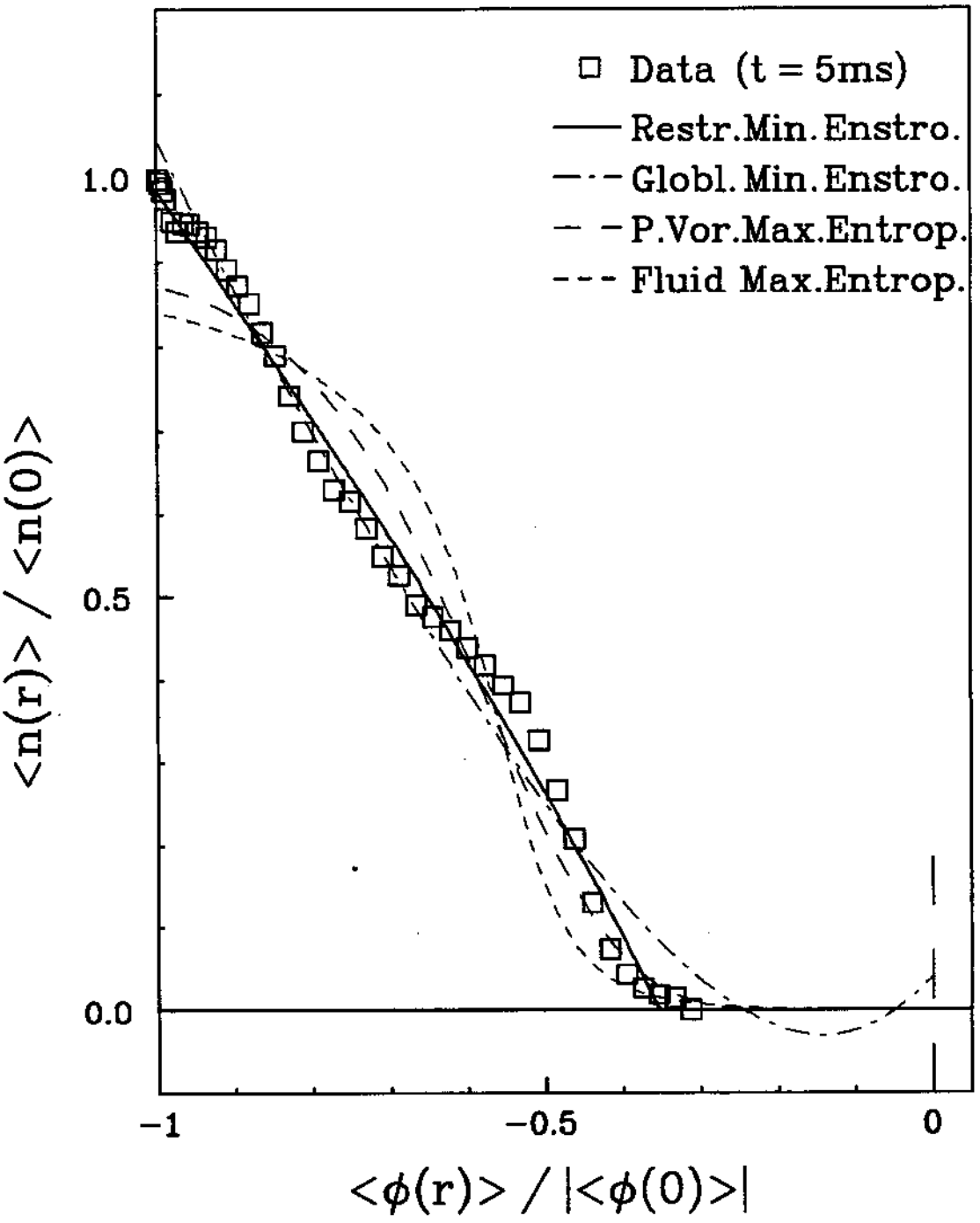

Figure 5.3: Meta-equilibrium density versus potential, and theoretical predictions from the 4 models discussed.

Here, the model profiles are calculated using the robust invariants obtained from the measured $< n(r) >$, with no adjustable parameters. The point vortex maximum entropy and continuous fluid maximum entropy predictions are plotted as long and short dashed curves respectively. These two profiles are both relatively flat near the column center, apparently due to the assumption of thorough ergodic mixing of the fluid elements. These profiles deviate significantly from the experimental data. The global minimum enstrophy prediction is plotted as the dot-dashed curve. This profile shows reasonable agreement with the data inside the column, but fails by going negative near the wall, where the measured density is essentially zero. Finally, the prediction from the restricted minimum enstrophy model is shown as the solid curve. This profile shows close overall agreement with the experimentally measured meta-equilibrium density data, typically within 5% for all radii. Note that the predicted central density and cut-off radius both agree closely with the experimental data, even though they are only determined by the integral invariants of (N_L, P_θ, H_ϕ).

A one-to-one correspondence exists between the theoretically predicted density n_{eq} and potential ϕ_{eq}, even though analytically, the relation is not generally explicit. Figure 5.3 shows the comparison of the measured n–ϕ dependence with the predictions of the four theoretical models. Here again, the data is best described by the restricted minimum enstrophy model, as expected from the $< n(r) >$ comparisons. Note that n–ϕ relation from the restricted minimum enstrophy vortex is approximately linear (solid curve). This is because parameter β for this column is quite small, making the r^2 contribution in Equation (5.13) negligible compared to the $J_0(\beta^{\frac{1}{2}} r)$ term.

I have experimentally measured the relaxed meta-equilibrium states resulting from initially hollow columns of various diameters, "hollowness" depths, and axial lengths in various magnetic fields. For example, two such meta-equilibrium states are

shown in Figure 5.4: Frame (a) is near the point where $\beta = 0$ with a parabolic density profile; Frame (b) is for the case of $H_\phi^{\rm exc}$ near its upper limit in Equation (5.18). Both curves show excellent agreement with the experimental data, typifying the correspondence between the measured meta-equilibrium columns and the restricted minimum enstrophy vortices.

The measured meta-equilibrium profiles give scaled enstrophy $\hat{Z}_2$ versus $H_\phi^{\rm exc}$, plotted as circles in Figure 5.5. The functional dependence from the restricted minimum enstrophy model is shown as the solid curve, with the vertical dashed line being the $H_\phi^{\rm exc}$ limit expressed in Equation (5.18). Here, the specific evolution of Figure 5.2 is shown as the solid symbols: the scaled enstrophy varies from $\hat{Z}_2 = 1.084$ at $t = 20\,\mu$s to $\hat{Z}_2 = 0.892$ at $t = 5\,$ms, with the restricted minimum enstrophy prediction being $\hat{Z}_2^{\rm min} = 0.890$. For comparison, the point vortex maximum entropy profile would have $\hat{Z}_2 = 0.900$, deviating from the data four times more than the restricted minimum enstrophy profile of Equation (5.11). Similarly, the measured enstrophy of the meta-equilibrium state is close to the prediction of the restricted minimum enstrophy theory for each initial conditions, typically within 1–2% of the enstrophy available for dissipation for each given (N_L, P_θ, H_ϕ). This reflects the fact that the measured $<n(r)>$ profiles generally agree well with Equation (5.11), comparable or better than the profile shown in Figure 5.2. In addition, as shown in Figure 5.5, the experimentally measured $\hat{Z}_2$ appears to be continuous across the theoretical upper limit of $H_\phi^{\rm exc}$. As $H_\phi^{\rm exc}$ further decreases, $\hat{Z}_2^{\rm min}$ rises again, with $\hat{Z}_2^{\rm min}(H_\phi^{\rm exc} = 0) = 1$.

These experimental evidences strongly support the selective decay hypothesis. Of course, only a limited region of parameter space has been explored and compared to theory. Nonetheless, the experiments clearly show that selective decay has predictive validity for these types of initial conditions.

Some other unstable initial conditions, such as 2 merging vortices [32, 60],

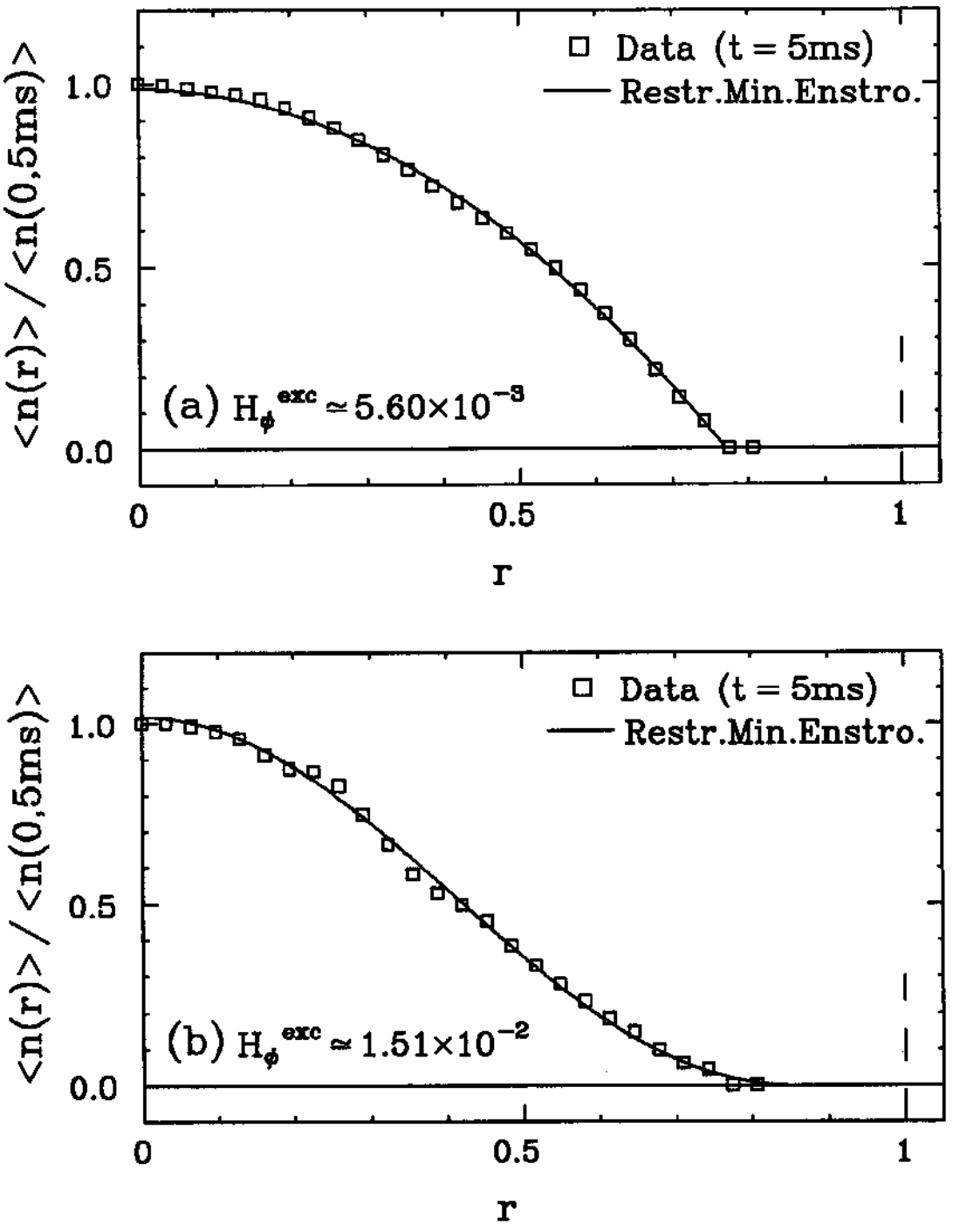

Figure 5.4: Radial profiles of two meta-equilibrium states near the limits. (a) Column having H_ϕ^{exc} near $\beta = 0$; (b) column having H_ϕ^{exc} near the upper limit.

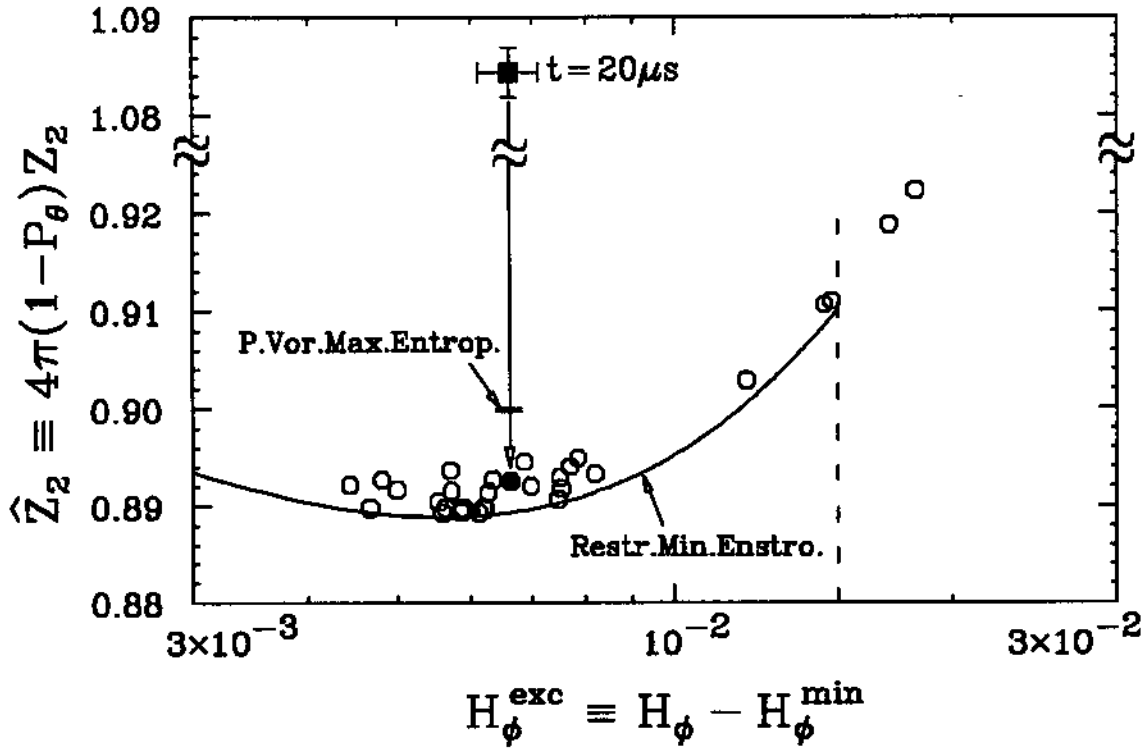

Figure 5.5: The scaled enstrophy $\hat{Z}_2$ of the meta-equilibrium state versus excess energy $H_\phi^{\rm exc}$, from measurements (circles) and from the restricted minimum enstrophy model (curve).

have $H_\phi^{\rm exc}$ a lot higher than the range specified by Equation (5.18), and result in measured meta-equilibrium profiles not describable by Equation (5.11). Further theoretical work is needed to understand the general minimum enstrophy states, and further experiments are necessary to establish under what circumstances unstable initial conditions *do* relax to these states.

5.3.3 Shot-to-Shot Variations of the Profiles

The measured meta-equilibrium states exhibit higher shot-to-shot fluctuation levels than their initial states, as shown in Figure 5.6(a). This data applies to the evolution of Figure 5.2 (the $l = 1$ sequence). The variation level at $t = 5$ ms ($\sim 1.6\%$

at $r = 0$) is typically 3–5 times greater than that of the initial state. Note that the initial shot-to-shot variation level must be measured using the phase-locked ensemble described in Section 3.4. The cause of this noise "amplification" is probably the instability processes resulting in the onset of turbulence, where two very close initial conditions deviate exponentially in time as the turbulence develops.

The spatial structure of these fluctuations can be investigated by measuring correlation functions. Consider the spatial correlations between a fixed collector (C0, C2, C2$^-$) and the radially scanning mobile collector Cr, as described in Section 2.2. Figure 5.6(b) shows $C_{0r}(r)$ at $t = 5$ ms to be highly axisymmetric, with a radial correlation length of about 0.5 cm. Figure 5.6(c) shows $C_{2r}(r)$ and $C_{2-r}(r)$ to have essentially identical axisymmetric shapes even though the fixed collectors C2 and C2$^-$ are azimuthally separated by 90°. It is clear that there are essentially no angular variations left after the column relaxes to the meta-equilibrium state, i.e., two-point correlations between collectors at $r = 0.36$ (such as C2, C2$^-$) are all above 90%, indicating that any remaining θ-variations and instrumental noise are less than 0.2% of the mean density at that radius. The measured fluctuations simply reflect the shot-to-shot variations of the meta-equilibrium radial profiles. Alternatively speaking, the data demonstrate that each particular column relaxes to a stationary axisymmetric profile, but their profiles varying slightly ($\sim 2\%$) from one shot to another. This then appears as shot-to-shot "noise", and persists until 3D processes cause the profiles to decay (see Figure 4.2).

5.3.4 Significance of the Experimental Results

The maximum entropy models fail apparently because during the evolution, there are regions which are not thoroughly mixed with the rest of the column. For example, the region of peak density $n_{\max}$ is evidently unmixed as it is transported, as shown in Table 5.1. Once the monotonically decreasing mean density profile is

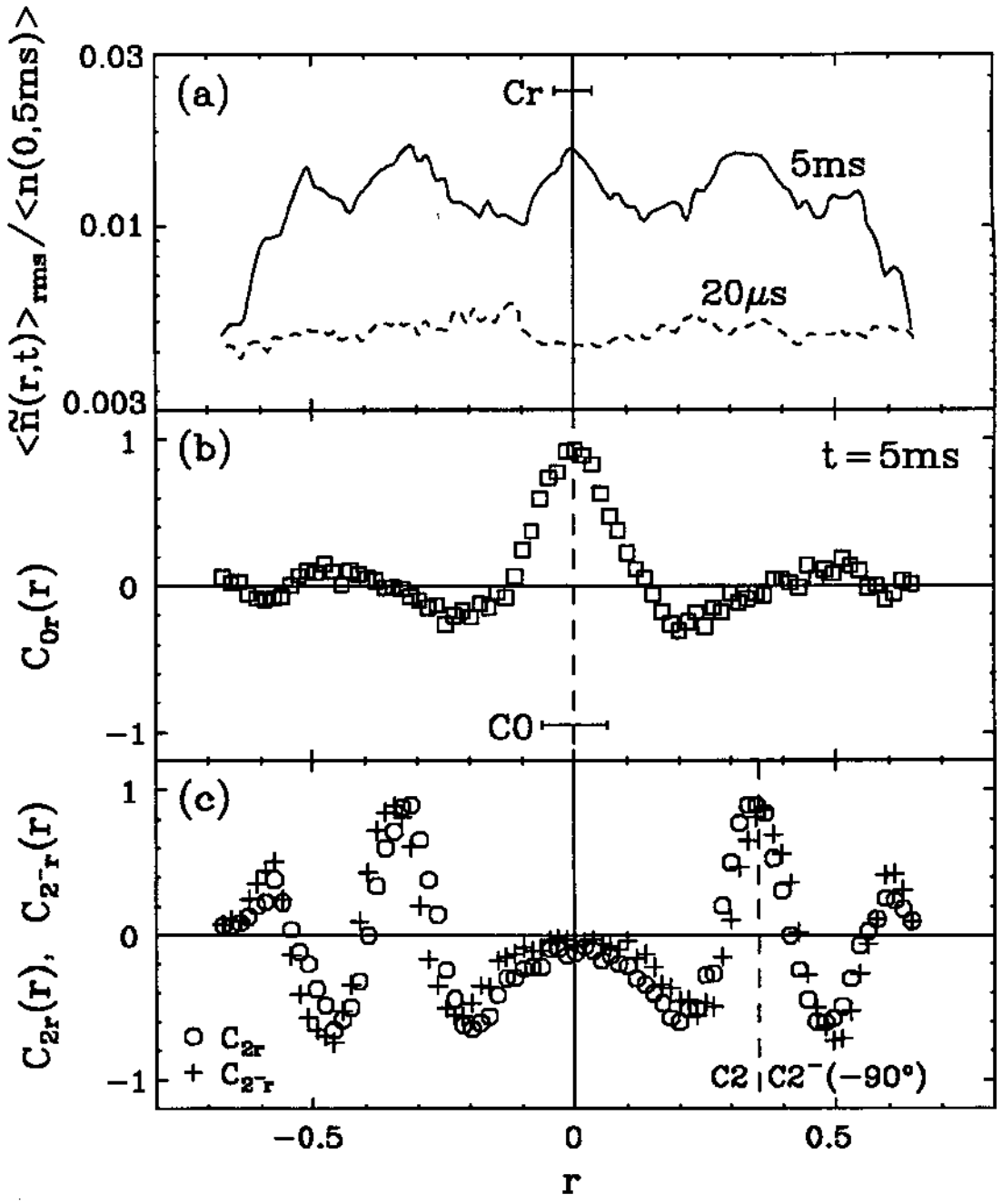

Figure 5.6: Shot-to-shot variations of the meta-equilibrium radial profiles at $t = 5$ ms. (a)Variation level measured on Cr versus r, compared to that of the initial state ($t = 20$ μs); (b)correlation function $C_{0r}(r)$, with the dashed line being the location of C0; (c)correlation function $C_{2r}(r)$ (circles) and $C_{2-r}(r)$ (pluses), where C2 and C2$^-$ are separated by 90° azimuthally.

established, the large-scale density rearrangement is greatly diminished, since there are no further global instabilities. As a result, the system does not equilibrate to the most probable state.

It is tempting to suggest that these experiments may model the emergence of coherent vortices in a region of non-zero circulation within a larger field of decaying 2D turbulence [56, 43, 3, 7]. In this case, the internal shape of the emerging vortices may be determined by the local conserved integrals through selective decay. Of course, the cylindrical walls give complete isolation of the columns considered here, whereas in a turbulent flow other regions can perturb any given vortex, with merger of like-signed vortices being perhaps the most extreme example of the external perturbation.

5.4 Decay of Meta-Equilibrium State

The meta-equilibrium state lasts more than 10^4 column rotations, or about 100 ms, as shown in Figure 4.2. It then decays due to non-ideal 2D $\mathbf{E} \times \mathbf{B}$ or 3D processes, such as "viscous" microscopic particle transport and external asymmetry induced anomalous transport [22, 25]. On this longer time scale, the radial profile changes slowly, characterized by the broadening of the column radius (P_θ and H_θ both decrease), and the decline of the central density [16]. Eventually, the column touches the cylinder wall, and electrons are lost.

Another point of view of this process can be seen through the evolution of the correlation functions of the shot-to-shot variations. Figure 5.7 shows the long-term evolution of function $C_{0r}(r)$. Between $t = 5$ ms and 10 ms, there is little change in the profile of $C_{0r}(r)$, reflecting the longevity of the meta-equilibrium state. By $t = 0.5$ s, the first zero of the correlation function (radial correlation length) has increased, as the measured variation level decreases by a factor of two (Figure 4.2). At $t = 2$ s,

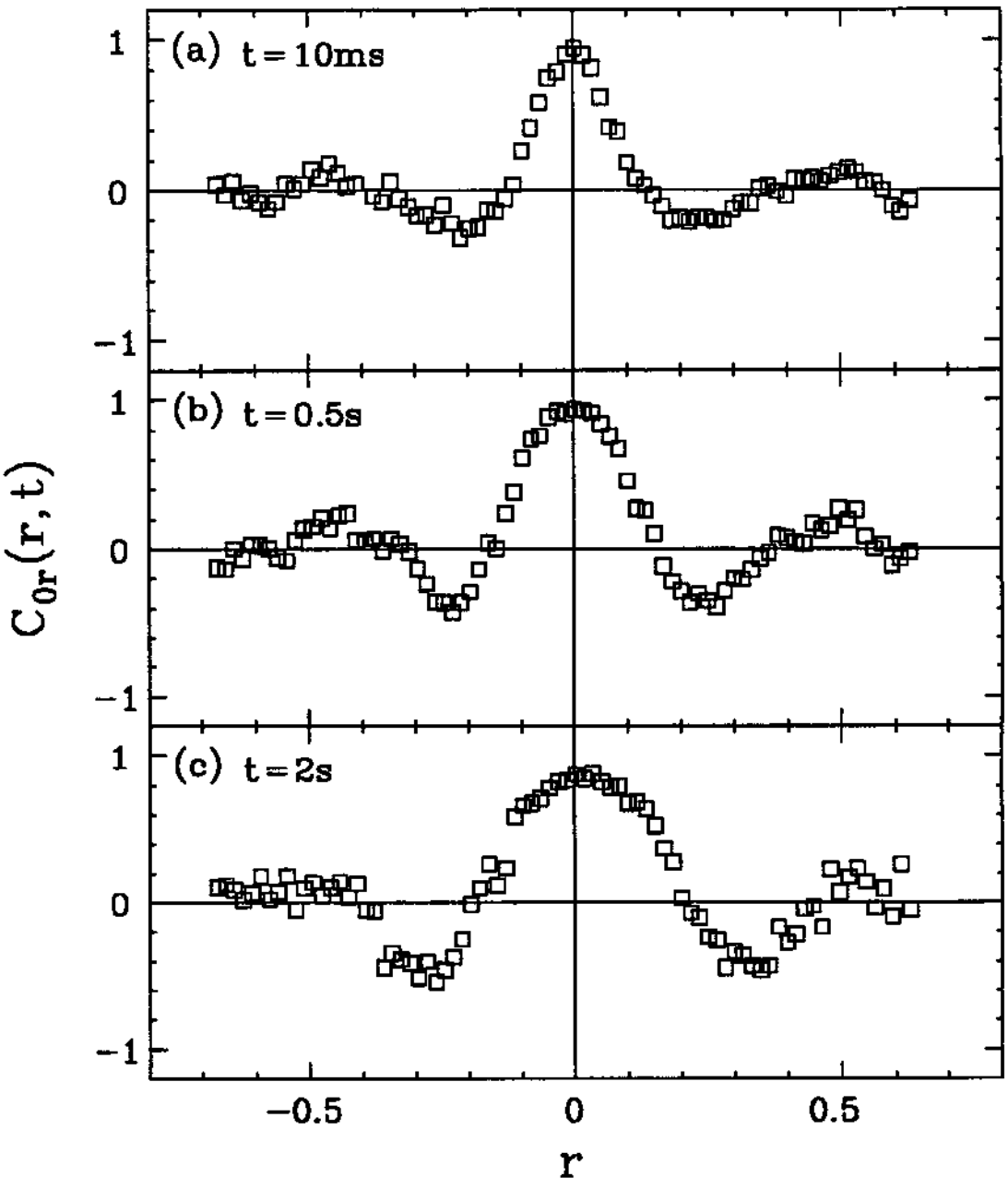

Figure 5.7: Long-term changes of the correlation function $C_{0r}(r,t)$ showing the decay of the meta-equilibrium state. (a)$C_{0r}(r, 10\,\mathrm{ms})$; (b)$C_{0r}(r, 0.5\,\mathrm{s})$; (c)$C_{0r}(r, 2\,\mathrm{s})$.

the central density has dropped by about 20%, and the radial correlation length is about twice as large as that of the meta-equilibrium state. This observation suggests that the effect of these non-ideal "viscous" processes acts preferrentially on the small spatial scales: relatively short wavelength "ripples" are smoothed out first, leaving out the longer ones, which eventually vanish together with the whole column.

Appendix A

Calibration of Collector Effective Cross Sections

In this appendix, I describe the calibration procedure for the effective collector cross sections as briefly mentioned in Section 2.2. The problem arises because the endplate and the mobile collector both have certain thickness, and therefore are susceptible to the collimator hole loss/mobile collector gain effect as first discussed by Fine [27].

When a column is dumped, electrons must first go through collimator holes on the endplate (thickness=0.318 cm) in order to be collected by the fixed collectors; since the electrons are executing gyromotion as they pass through the collimator holes, some of the electrons that should have been collected if the endplate were infinitely thin, are lost to the endplate. Consequently, the effective cross section of the fixed collectors are smaller than the area of the collimator holes. Similarly, the effective cross section of the mobile collector (thickness $\simeq$ 0.30 cm) is larger than the area of its facing surface.

Let's estimate the number of gyro-orbits an electron executes while it passes through a collimator hole. The parallel kinetic energy of the electron at the endplate is about 100 eV due to the +90 V bias applied to the endplate; therefore, it takes 0.54 ns to travel through the hole. Consider $B_z \simeq 500$ G with gyrofrequency

$w_c/2\pi \simeq 1.4$ GHz; within 0.54ns, the electron makes about 3/4 of one orbit. Assuming that all the electrons that come into contact with the endplate are absorbed, 75% of the electrons in a circular strip $2R_L$ wide and $2\pi R_{C0}$ long are lost [27], where R_L is the electron gyroradius and R_{C0} is the radius of the collimator holes. Consequently, the effective collector cross section is approximately

$$A_{C0} \simeq \pi R_{C0}^2 (1 - 0.75 \times \frac{4R_L}{R_{C0}}) . \tag{A.1}$$

Analogously, the effect cross section of the mobile collector Cr is *increased*, and estimated to be

$$A_{Cr} \simeq \pi R_{Cr}^2 (1 + 0.70 \times \frac{4R_L}{R_{C0}}) . \tag{A.2}$$

Experimentally, I only assume that the effective cross section of the fixed collectors and that of the mobile collector follow the relation

$$\frac{A_{C0} - \pi R_{C0}^2}{A_{Cr} - \pi R_{Cr}^2} \simeq -\frac{R_{C0}}{R_{Cr}} . \tag{A.3}$$

In other words, the orbit fractions for C0 and Cr, which are 0.75 and 0.70 respectively from the theoretical estimates, are assumed to be approximately equal, and are determined from the calibration measurements.

Stable columns with highly reproducible flat radial profiles are trapped and then dumped. First, I measure the charge Q_0 collected on the central fixed collector C0. Next, the mobile collector Cr is placed at the cylinder center and the charge Q_r it collects is then obtained. Since the two collectors are measuring the same physical density, the ratio of Q_0 and Q_r must satisfy

$$\frac{Q_0}{Q_r} = \frac{A_{C0}}{A_{Cr}} . \tag{A.4}$$

From Equations (A.3) and (A.4), the effective collector cross sections A_{C0} and A_{Cr} can be solved.

Normally, for columns with electron perpendicular temperature $T_\perp \simeq 1$ eV, the experimentally determined orbit fraction is about unity, resulting in corrections to the cross sections to be $\lesssim 10\%$. As an independent verification on this calibration procedure, one can check the agreement between the number of electrons per unit length N_L measured at the axial midpoint of a column, and that calculated from the integral $\int d^2\mathbf{x}\, n(\mathbf{x})$. Typically, the agreement is better than 5%, which is approximately the accuracy of the absolute density measurement. In the main text of this thesis, these two definitions of N_L are used interchangeably.

Appendix B

Linear Decomposition of 2D Incompressible Flows

In general, the kinematics of a 2D incompressible flow can be linearly decomposed into two parts: one that induces vorticity, called the pure rotational component, and the other that causes kinematic distortion, called the pure straining component.

Let's assume that one is in the reference frame (x', y') where the fluid is stationary at the origin O. In this frame, the 2D velocity field $\mathbf{v}(x', y')$ can be written as

$$\mathbf{v}(x', y') = \hat{\mathbf{z}} \times \nabla' \Psi(x', y') \,, \tag{B.1}$$

where Ψ is the 2D stream function. If the velocity of this flow is regular (differentiable) near the origin and is slow-varying spatially, $\Psi(x', y')$ can be approximated by its Taylor expansion around point O,

$$\Psi(x', y') \simeq \alpha_1 x'^2 + \alpha_2 y'^2 + \alpha_3 x' y' \,, \tag{B.2}$$

where $\Psi(0, 0)$ is set to zero, and the linear terms vanish because the fluid is stationary at the origin. Parameters $(\alpha_1, \alpha_2, \alpha_3)$ are the Taylor coefficients associated with the second derivatives of Ψ, i.e., the first derivatives of $\mathbf{v}(x', y')$.

Generally speaking, upon a proper rotation of the orientation of the Cartesian

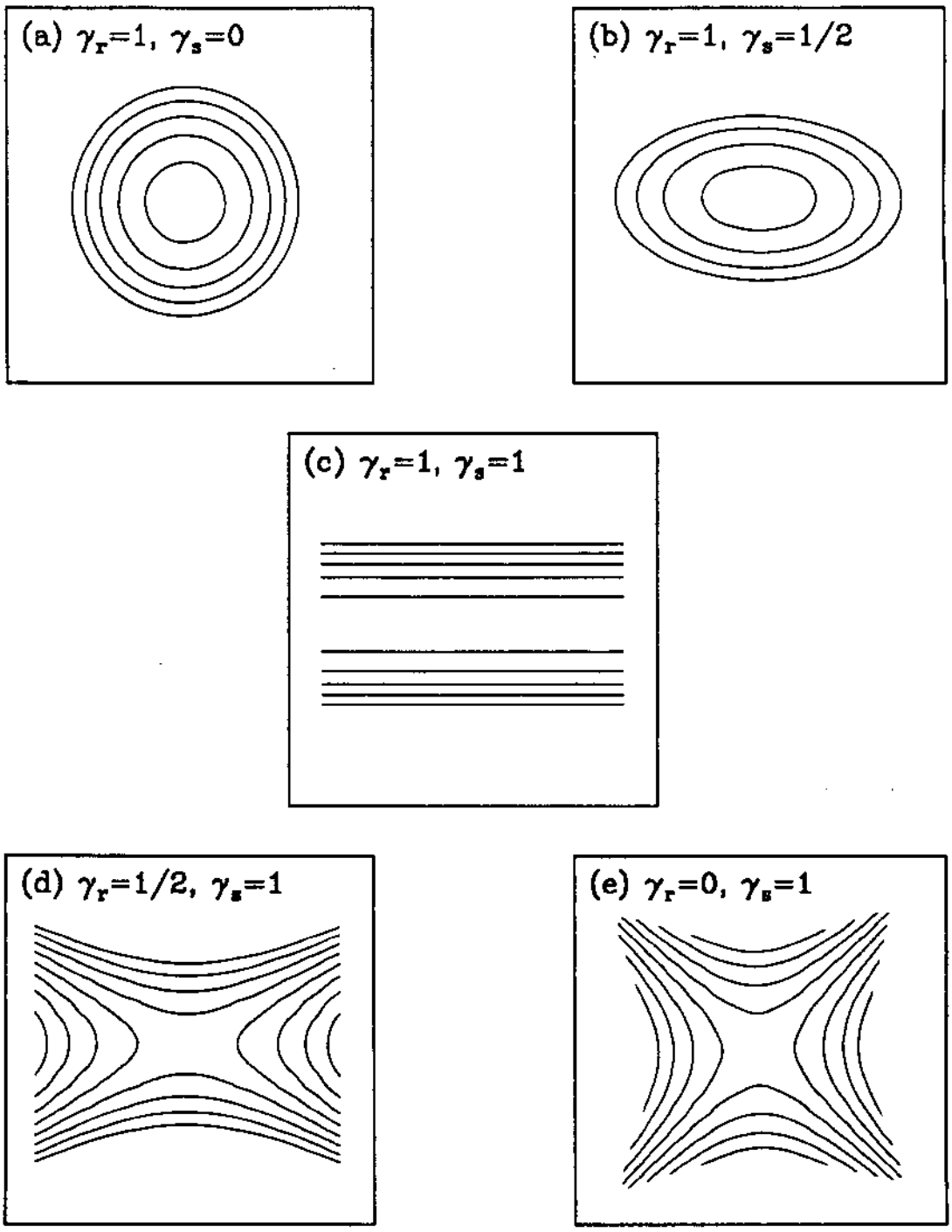

Figure B.1: 2D flow patterns near a fixed origin. Case (a)–(e) are discussed in the text.

coordinates from (x', y') to (x, y). Ψ can be rewritten as,

$$\Psi(x,y) \simeq \Psi^{(2)}(x,y) = \frac{\gamma_r}{2}(x^2+y^2) - \frac{\gamma_s}{2}(x^2-y^2)\,, \tag{B.3}$$

where the γ_r term is the pure rotational component and the γ_s term is the pure straining component. The coefficients γ_r and γ_s are

$$\begin{cases} \gamma_r = (a_1 + a_2) \\ \gamma_s = \sqrt{(a_1 - a_2)^2 + a_3^2}\,. \end{cases} \tag{B.4}$$

For a 2D incompressible flow, at each instant, contours of the stream function also describe its flow pattern at that time, with the velocity vector determined according to Equation (B.1). Shown in Figure B.1 are the contours of stream function $\Psi^{(2)}(x,y)$ for various values of γ_r and γ_s:

(a) $\gamma_r = 1$, $\gamma_s = 0$, pure rotation, circular closed flow;

(b) $\gamma_r = 1$, $\gamma_s = 1/2$, mixed rotation and strain, elliptical closed flow;

(c) $\gamma_r = 1$, $\gamma_s = 1$, equal rotation and strain, simple shearing open flow;

(d) $\gamma_r = 1/2$, $\gamma_s = 1$, mixed rotation and strain, asymmetric hyperbolic open flow;

(e) $\gamma_r = 0$, $\gamma_s = 1$, pure strain, symmetric hyperbolic open flow.

Note that $2\gamma_r$ is simply the local vorticity ζ at the origin.

As an example, this decomposition can be applied to a shearing rotational flow $\mathbf{v} = \omega(r)\, r\hat{\boldsymbol{\theta}}$. Let's consider the relative velocity $\mathbf{v}_R$ near a point $r = r_0$ in the rotating frame with angular velocity $\omega_0 \equiv \omega(r_0)$,

$$\mathbf{v}_R = [\omega(r) - \omega_0]\, r\hat{\boldsymbol{\theta}}\,. \tag{B.5}$$

By choosing a Cartesian coordinate system (x, y) centered at r_0 with x-axis in the θ direction, i.e., the direction of the rotational flow, one can express the relative

stream function $\Psi_R(x,y)$ as

$$\Psi_R \simeq \Psi_R^{(2)} = \gamma_R y^2 \,, \tag{B.6}$$

indicating that the relative 2D flow is a simple shear, with $\gamma_r = \gamma_s = \gamma_R$. Here, the shear-induced vorticity is

$$2\gamma_R = r_0 \frac{d\omega}{dr}|_{r_0} \quad . \tag{B.7}$$

Consequently, for monotonically decreasing $\omega(r)$ profiles, vorticity $2\gamma_R$ is normally negative.

Appendix C

Motion of Two Unbounded Point Vortices

In this appendix, I review the motion of two point vortices in 2D fluid open domains. This is an idealized description for two finite size vortices that are relatively well separated so that their shapes are approximately circular, and for cases where these vortices are far away from the boundary within which they are confined.

Under the point vortex idealization, only the total circulation Γ_1 and Γ_2 (for vortex 1 and 2 respectively) enter the dynamics. Let $\mathbf{r}_1$ and $\mathbf{r}_2$ be the vector coordinates of vortex 1 and 2, one can then define the position of the center of circulation

$$\mathbf{r}_\Gamma \equiv \frac{\Gamma_1 \mathbf{r}_1 + \Gamma_2 \mathbf{r}_2}{\Gamma_1 + \Gamma_2}\,, \tag{C.1}$$

with the relative displacement vector being $\mathbf{r}_r \equiv \mathbf{r}_2 - \mathbf{r}_1$.

From point vortex kinematics, motion of the two unbounded vortices is determined by

$$\begin{cases} \dfrac{d\mathbf{r}_1}{dt} = -\dfrac{\Gamma_2}{2\pi|\mathbf{r}_r|^2}\hat{\mathbf{z}} \times \mathbf{r}_r \\ \dfrac{d\mathbf{r}_2}{dt} = +\dfrac{\Gamma_1}{2\pi|\mathbf{r}_r|^2}\hat{\mathbf{z}} \times \mathbf{r}_r\,. \end{cases} \tag{C.2}$$

Therefore, the equations for $\mathbf{r}_\Gamma$ and $\mathbf{r}_r$ are

$$\frac{d\mathbf{r}_\Gamma}{dt} = 0; \quad \frac{d\mathbf{r}_r}{dt} = (\frac{\Gamma_1 + \Gamma_2}{2\pi|\mathbf{r}_r|^2})\hat{\mathbf{z}} \times \mathbf{r}_r\,. \tag{C.3}$$

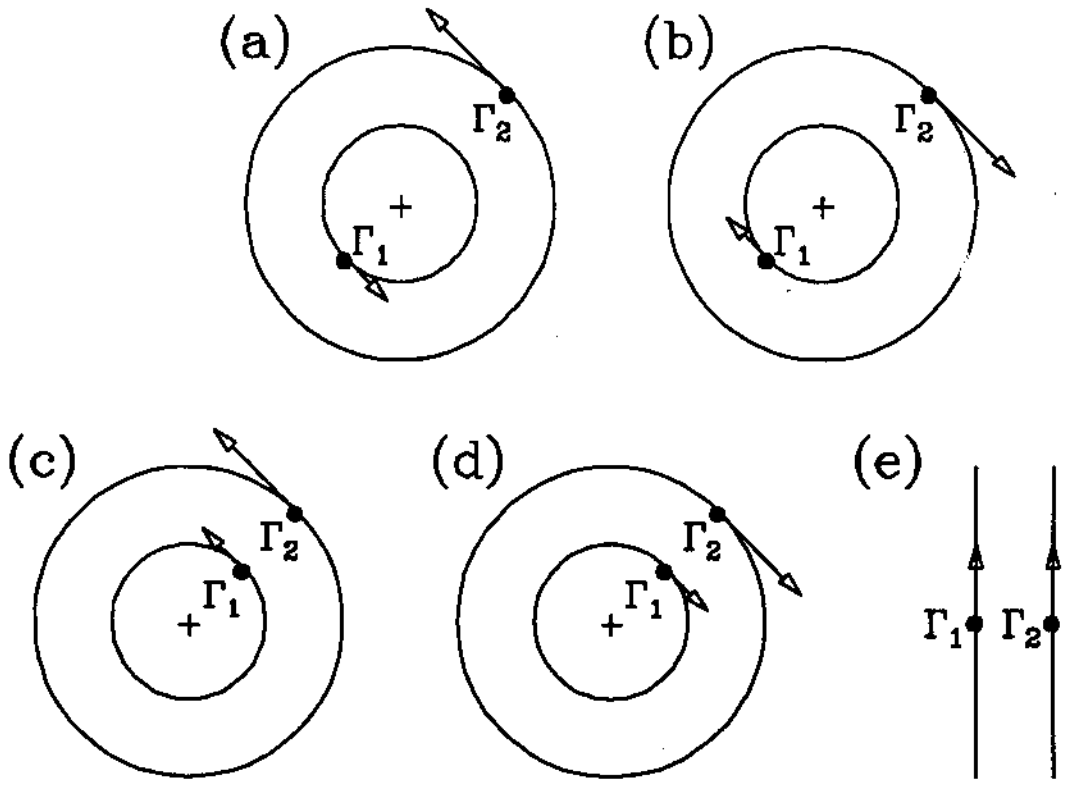

Figure C.1: Motion of two unbounded point vortices. Case (a)–(e) are discussed in the text.

Under this description, the relative distance $|\mathbf{r}_r|$ is obviously a constant, and the two vortices undergo rotational motion around the stationary center of circulation with angular velocity

$$\omega_r = \frac{\Gamma_1 + \Gamma_2}{2\pi |\mathbf{r}_r|^2} . \tag{C.4}$$

As shown in illustration Figure C.1, the motion of two unbounded point vortices described by Equation (C.3) can be classified into the following five cases:

(a) $\Gamma_1 > 0$, $\Gamma_2 > 0$, rotation in the counterclockwise direction, 180° out of phase;

(b) $\Gamma_1 < 0$, $\Gamma_2 < 0$, rotation in the clockwise direction, 180° out of phase;

(c) $\Gamma_1 > 0$, $\Gamma_2 < 0$, and $|\Gamma_1| > |\Gamma_2|$, rotation in the counterclockwise direction, in phase;

(d) $\Gamma_1 < 0$, $\Gamma_2 > 0$, and $|\Gamma_1| > |\Gamma_2|$, rotation in the clockwise direction, in phase;

(e) $\Gamma_1 > 0$, $\Gamma_2 < 0$, and $|\Gamma_1| = |\Gamma_1|$, translation in the $(\hat{\mathbf{z}} \times \hat{\mathbf{r}}_T)$ direction.

Since there exists a direct analogy between 2D fluid and $\mathbf{E} \times \mathbf{B}$ drift dynamics, motion of two unbounded, magnetized electron columns can also be approximately described by Equation (C.3), with $\Gamma = 4\pi e c N_L / B_z$.

Appendix D

Useful Mathematical Identities Involving Bessel Functions

Some useful mathematical identities involving Bessel functions are listed in this appendix, which are mainly used in Chapter 5 to calculate minimum enstrophy vortices.

Let $J_m(z)$ and $I_m(z)$ be the mth order ordinary and modified Bessel function (first kind) respectively, where the index $m = 0, \pm 1, \pm 2, \ldots$; the following equations are mathematically correct [1]:

(a) relation between J_m and I_m

$$I_m(z) = (-i)^m J_m(iz)\,; \tag{D.1}$$

(b) power series expansion

$$J_m(z) = (\frac{z}{2})^m \sum_{k=0}^{\infty} \frac{(-1)^k z^{2k}}{4^k k!(m+k)!}\,; \tag{D.2}$$

(c) integral representation

$$J_m(z) = \frac{(-i)^m}{\pi} \int_0^{\pi} d\theta\, \cos(m\theta) \exp(iz\cos\theta)\,; \tag{D.3}$$

(d) recurrence relations

$$\frac{dJ_m(z)}{dz} = -J_{m+1}(z) + \frac{m}{z} J_m(z)\,, \tag{D.4}$$

$$\frac{dJ_m(z)}{dz} = J_{m-1}(z) - \frac{m}{z}J_m(z)\,, \tag{D.5}$$

in particular,

$$\frac{dJ_0}{dz} = -J_1\,; \tag{D.6}$$

(e) general definite integrals (for $m \geq 0$)

$$\int_0^z dz'\,(z')^m J_{m-1}(z') = z^m J_m(z)\,, \tag{D.7}$$

$$\int_0^z dz'\,(z')^{-m} J_{m+1}(z') = \frac{1}{2^m m!} - z^{-m}J_m(z)\,, \tag{D.8}$$

in particular,

$$\int_0^z dz'\,z' J_0(z') = zJ_1(z)\,, \tag{D.9}$$

$$\int_0^z dz'\,J_1(z') = 1 - J_0(z)\,; \tag{D.10}$$

(f) special definite integrals

$$\int_0^z dz'\,z'^3 J_0(z') = z^3 J_1(z) - 2z^2 J_2(z)\,, \tag{D.11}$$

$$\int_0^z dz'\,z' J_0^2(z') = \frac{z^2}{2}\left[\,J_0^2(z) + J_1^2(z)\,\right]. \tag{D.12}$$

All the definite integrals can be proven by using the recurrence relations.

In addition to the identities listed above, numerical values of the roots of ordinary Bessel functions are also often used. The real roots of $J_0(z)$ are

$$j_{0,1} = 2.4048 \quad j_{0,2} = 5.5201 \quad j_{0,3} = 8.6537 \quad \ldots\,;$$

and for $J_1(z)$, the nontrivial roots are

$$j_{1,1} = 3.8317 \quad j_{1,2} = 7.0156 \quad j_{1,3} = 10.173 \quad \ldots\,.$$

Since $dJ_0(z)/dz = -J_1(z)$, the roots of $J_1(z)$ also correspond to the extremum points of function $J_0(z)$.

Appendix E

Symbols and Notations

This appendix compiles lists of commonly used symbols and notations in this and other related works [60]. Whenever necessary, definition of a symbol or equation number where it is first introduced is given. All equations are in the cgs convention; in addition, as described in Chapter 3, notation <> represents the ensemble-average, and variables with $\sim$ sign on top are the fluctuating components.

********** **Fundamental Quantities** **********

$-e$		Electron charge
m_e		Electron mass
c		Speed of light in vacuum
k_B		Boltzmann constant
R_w	3.048cm	Cylinder wall radius
t		Evolution hold time
$\mathbf{x}$		Spatial coordinate vector
$\mathbf{k}$		Wavenumber vector
$\mathbf{r}$	$\mathbf{x}/R_w$	Normalized cylindrical coordinate
$\mathbf{B}$	$B_z\hat{\mathbf{z}}$	Background axial magnetic field
ϕ		Electrostatic space charge potential
$\mathbf{E}$	$-\nabla\phi$	Electric field
T,$T_\parallel$,$T_\perp$		Electron temperature, parallel and perpendicular to the magnetic field
$n(r,\theta)$		z-averaged (2D) electron density
$\mathbf{v}(r,\theta)$		Fluid perpendicular (2D) velocity

********** **Times and Frequencies** **********

ω_c	$eB_z/(m_e c)$	Electron gyrofrequency
γ_b	$\sqrt{\frac{k_B T_\parallel}{m_e}}/(2L_p)$	Average electron axial bounce frequency
ω_p	$\sqrt{4\pi n e^2/m_e}$	Electron plasma frequency
ω	Eq. (3.11)	Guiding-center $\mathbf{E} \times \mathbf{B}$ drift angular velocity
τ_m	Eq. (2.3)	Electron column lifetime
τ_{ee}		Electron-electron particle collision time
τ_e	Eq. (4.8)	e-folding decay time of density fluctuations
γ_e	τ_e^{-1}	Fluctuation decay rate
γ_g		Global fluctuation decay rate
χ_l	Eq. (4.5)	Passive tracer fluctuation decay rate

********** **Lengths** **********

L_c	3.2cm→113cm	Confinement cylinder length
R_L	$\sqrt{\frac{2k_B T_\perp}{m_e}}/\omega_c$	Average electron gyroradius
λ_D	$\sqrt{k_B T/4\pi n e^2}$	Debye length
R_p	0.5cm→2.5cm	Electron column radius
L_p	3cm→110cm	Electron column axial length
R_C	0.10cm, 0.20cm	Radius of charge collectors
A_C	$\sim \pi R_C^2$	Calibrated cross section of charge collectors

********** **Dimensionless Quantities** **********

g_c	Eq. (3.17)	Collector coarse-graining attenuation factor
S_k		Skewness of the density fluctuations
K_u		Kurtosis of the density fluctuations
C_{ij}		Normalized zero-time correlation function of the density fluctuations between collector Ci and Cj
σ	$r_v \frac{d\omega}{dr}\|_{r_v} / \tilde{\zeta}_v$	Scaled shear rate of background rotation
λ_{eq}	a/b	Aspect ratio of equilibrated elliptical vortices

********** **Integrals** **********

N_L	$R_w^2 \int d^2\mathbf{r}\, n$	Number of electrons per unit length
N_e	$N_L L_p$	Total number of electrons
$\mathcal{P}_\theta$	$\frac{eB_z R_w^4}{2c}\int d^2\mathbf{r}(1-r^2)n$	Magnetic angular momentum per unit length
P_θ	$\mathcal{P}_\theta/(\frac{eB_z R_w^2 N_L}{2c})$	Dimensionless angular momentum
$\mathcal{H}_\phi$	$-\frac{eR_w^2}{2}\int d^2\mathbf{r}\,\phi\, n$	Electrostatic energy per unit length
H_ϕ	$\mathcal{H}_\phi/(e^2 N_L^2)$	Dimensionless energy
$H_\phi^{\min}$	$[\frac{1}{2} - \ln 2(1-P_\theta)]/2$	Minimum energy for constant N_L and P_θ
H_ϕ^{exc}	$H_\phi - H_\phi^{\min}$	Excess energy
$\mathcal{Z}_m$	$\frac{R_w^2}{m}\int d^2\mathbf{r}\, n^m$	mth moment of density, $m = 2, 3, 4, \ldots$
Z_m	$\mathcal{Z}_m/[\frac{N_L^m}{R_w^{2(m-1)}}]$	Dimensionless mth moment of density
Z_2		Dimensionless enstrophy

********** **2D Fluid Dynamics Quantities** **********

P_{m}	Eq. (3.2)	Fluid pressure field
ρ_{m}	Eq. (3.2)	Fluid specific mass
ν_{m}	Eq. (3.2)	Kinematic molecular viscosity
$\Psi(r,\theta)$	Eq. (3.3)	2D stream function
$\zeta(r,\theta)$	Eq. (3.3)	2D scalar vorticity
Γ	$\int d^2\mathbf{x}\,\zeta$	Circulation per unit mass
$\mathcal{A}_z$	$\frac{1}{2}\int d^2\mathbf{x}\,(1-\lvert\mathbf{x}\rvert^2)\zeta$	Angular impulse per unit mass
$\mathcal{E}$	$\frac{1}{2}\int d^2\mathbf{x}\,\lvert\mathbf{v}\rvert^2$	Kinetic energy per unit mass
Ω	$\frac{1}{2}\int d^2\mathbf{x}\,\zeta^2$	Enstrophy

********** **Miscellaneous** **********

l		Azimuthal mode number
$\rho(n')$		Density probability distribution function (PDF)
$-V_c$	~ -150V	Electric confinement voltage (generally on confinement gates)

References

[1] M. Abramowitz and I. A. Stegun. *Handbook of Mathematical Functions.* Dover Publications, seventh edition, 1972.

[2] L. Armi and P. Flament. Cautionary remarks on the spectral interpretation of turbulent flows. *J. Geophys. Res.*, 90:11779, 1985.

[3] A. Babiano, C. Basdevant, B. Legras, and R. Sadourny. Vorticity and passive-scalar dynamics in two-dimensional turbulence. *J. Fluid Mech.*, 183:379, 1987.

[4] G. K. Batchelor. *The Theory of Homogeneous Turbulence.* Cambridge University Press, 1953.

[5] G. K. Batchelor. Computation of the energy spectrum in homogeneous two-dimensional turbulence. *Phys. Fluids Suppl. II*, 12:233, 1969.

[6] R. Benzi, S. Patarnello, and P. Santangelo. Self-similar coherent structures in two-dimensional decaying turbulence. *J. Phys. A*, 21:1221, 1988.

[7] M. E. Brachet, M. Meneguzzi, H. Politano, and P. L. Sulem. The dynamics of freely decaying two-dimensional turbulence. *J. Fluid Mech.*, 194:333, 1988.

[8] F. P. Bretherton and D. B. Haidvogel. Two-dimensional turbulence above topography. *J. Fluid Mech.*, 78:129, 1976.

[9] R. J. Briggs, J. D. Daugherty, and R. H. Levy. Role of Landau damping in crossed-field electron beams and inviscid shear flow. *Phys. Fluids*, 13:421, 1970.

[10] G. F. Carnevale and J. S. Frederiksen. Nonlinear stability and statistical mechanics of flow over topography. *J. Fluid Mech.*, 175:157, 1987.

[11] G. F. Carnevale, J. C. McWilliams, Y. Pomeau, J. B. Weiss, and W. R. Young. Evolution of vortex statistics in two-dimensional turbulence. *Phys. Rev. Lett.*, 66:2735, 1991.

[12] F. F. Chen. *Introduction to Plasma Physics and Controlled Fusion*, volume 1. Plenum Press, second edition, 1984.

[13] Y. Couder. Two-dimensional grid turbulence in a thin liquid film. *J. Phys. Lett.*, 45:L–353, 1984.

[14] R. C. Davidson. *Theory of Non-Neutral Plasmas.* W. A. Benjamin, 1974.

[15] R. C. Davidson. *Physics of Nonneutral Plasmas.* Addison-Wesley, 1990.

[16] J. S. deGrassie. *Equilibrium, Waves and Transport in the Pure Electron Plasma.* PhD thesis, University of California at San Diego, 1977.

[17] J. S. deGrassie and J. H. Malmberg. Waves and transport in the pure electron plasma. *Phys. Fluids*, 23:63, 1980.

[18] C. F. Driscoll. Observation of a $l = 1$ diocotron mode on a hollow electron column. *Phys. Rev. Lett.*, 64:645, 1990.

[19] C. F. Driscoll and K. S. Fine. Experiments on vortex dynamics in pure electron plasma. *Phys. Fluids B*, 2:1359, 1990.

[20] C. F. Driscoll, K. S. Fine, and J. H. Malmberg. Reduction of radial losses in a pure electron plasma. *Phys. Fluids*, 29:2015, 1986.

[21] C. F. Driscoll and J. H. Malmberg. Length-dependent containment of a pure electron plasma. *Phys. Rev. Lett.*, 50:167, 1983.

[22] C. F. Driscoll, J. H. Malmberg, and K. S. Fine. Observation of transport to thermal equilibrium in pure electron plasmas. *Phys. Rev. Lett.*, 60:1290, 1988.

[23] C. F. Driscoll, J. H. Malmberg, K. S. Fine, R. A. Smith, X.-P. Huang, and R. W. Gould. Growth and decay of turbulent vortex structures in pure electron plasmas. In *Plasma Physics and Controlled Nuclear Fusion Research 1988*, page 507. IAEA, Vienna, 1989.

[24] D. H. E. Dubin, 1993. private communication.

[25] D. H. E. Dubin and T. M. O'Neil. Two-dimensional guiding-center transport of a pure electron plasma. *Phys. Rev. Lett.*, 60:1286, 1988.

[26] T. H. Dupree. Coarse-grain entropy in two-dimensional turbulence. *Phys. Fluids B*, 4:3101, 1992.

[27] K. S. Fine. *Experiments with the $l = 1$ Diocotron Mode.* PhD thesis, University of California at San Diego, 1988.

[28] K. S. Fine. Simple model of a nonlinear diocotron mode. *Phys. Fluids B*, 4:1, 1992.

[29] K. S. Fine, 1993. private communication.

[30] K. S. Fine, C. F. Driscoll, and X.-P. Huang. Observations of two-dimensional turbulence with a one-shot density diagnostic. *Bull. Am. Phys. Soc.*, 38:1971, 1993.

[31] K. S. Fine, C. F. Driscoll, and J. H. Malmberg. Measurements of a nonlinear diocotron mode in pure electron plasmas. *Phys. Rev. Lett.*, 63:2232, 1989.

[32] K. S. Fine, C. F. Driscoll, J. H. Malmberg, and T. B. Mitchell. Measurements of symmetric vortex merger. *Phys. Rev. Lett.*, 67:588, 1991.

[33] U. Frisch and S. A. Orszag. Turbulence: Challenges for theory and experiment. *Physics Today*, 43:24, 1990.

[34] R. W. Gould and M. A. LaPointe. Cyclotron resonance in a pure electron plasma column. *Phys. Rev. Lett.*, 67:3685, 1991.

[35] A. Hasegawa. Self-organization processes in continuous media. *Adv. Phys.*, 34:1, 1985.

[36] E. J. Hopfinger and G. J. F. van Heijst. Vortices in rotating fluids. *Ann. Rev. Fluid Mech.*, 25:241, 1993.

[37] A. W. Hyatt. *Measurement of the Anisotropic Temperature Relaxation Rate in a Magnetized Pure Electron Plasma.* PhD thesis, University of California at San Diego, 1988.

[38] S. Kida. Motion of an elliptic vortex in a uniform shear flow. *J. Phys. Soc. Japan*, 50:3517, 1981.

[39] R. H. Kraichnan. Inertial ranges in two-dimensional turbulence. *Phys. Fluids*, 10:1417, 1967.

[40] R. H. Kraichnan. Statistical dynamics of two-dimensional flow. *J. Fluid Mech.*, 67:155, 1975.

[41] R. H. Kraichnan and D. Montgomery. Two-dimensional turbulence. *Rep. Prog. Phys.*, 43:547, 1980.

[42] N. A. Krall and A. W. Trivelpiece. *Principles of Plasma Physics.* San Francisco Press, Inc., 1986.

[43] C. E. Leith. Minimum enstrophy vortices. *Phys. Fluids*, 27:1388, 1984.

[44] R. H. Levy. Diocotron instability in a cylindrical geometry. *Phys. Fluids*, 8:1288, 1965.

[45] R. H. Levy. Two new results in cylindrical diocotron theory. *Phys. Fluids*, 11:920, 1968.

[46] C. C. Lin. *The Theory of Hydrodynamic Stability.* Cambridge University Press, 1965.

[47] J. L. Lumley. Some comments on turbulence. *Phys. Fluids A*, 4:203, 1992.

[48] D. Lynden-Bell. Statistical mechanics of violent relaxation in stellar systems. *Mon. Not. R. Astro. Soc.*, 136:101, 1967.

[49] J. H. Malmberg and J. S. deGrassie. Properties of a nonneutral plasma. *Phys. Rev. Lett.*, 35:577, 1975.

[50] J. H. Malmberg and C. F. Driscoll. Long-time containment of a pure electron plasma. *Phys. Rev. Lett.*, 44:654, 1980.

[51] J. H. Malmberg, C. F. Driscoll, B. R. Beck, D. L. Eggleston, J. Fajans, K. S. Fine, X.-P. Huang, and A. W. Hyatt. Experiments with pure electron plasmas. In C. W. Roberson and C. F. Driscoll, editors, *Non-Neutral Plasma Physics*, page 28. American Institute of Physics, 1988.

[52] P. S. Marcus. Numerical simulation of Jupiter's Great Red Spot. *Nature*, 331:693, 1988.

[53] P. S. Marcus. Vortex dynamics in a shearing zonal flow. *J. Fluid Mech.*, 215:393, 1990.

[54] W. H. Matthaeus and D. Montgomery. Selective decay hypothesis at high mechanical and magnetic Reynolds Numbers. *Ann. N.Y. Acad. Sci.*, 357:203, 1980.

[55] W. H. Matthaeus, W. T. Stribling, D. Martinez, S. Oughton, and D. Montgomery. Selective decay and coherent vortices in two-dimensional incompressible turbulence. *Phys. Rev. Lett.*, 66:2731, 1991.

[56] J. C. McWilliams. The emergence of isolated coherent vortices in turbulent flow. *J. Fluid Mech.*, 146:21, 1984.

[57] J. C. McWilliams. A demonstration of the suppression of turbulent cascade by coherent vortices in two-dimensional turbulence. *Phys. Fluids A*, 2:547, 1990.

[58] J. Miller. Statistical mechanics of Euler Equations in two-dimensions. *Phys. Rev. Lett.*, 65:2137, 1990.

[59] J. Miller, P. B. Weichman, and M. C. Cross. Statistical mechanics, Euler's Equation, and Jupiter's Red Spot. *Phys. Rev. A*, 45:2328, 1992.

[60] T. B. Mitchell. *Experiments on Electron Vortices in a Malmberg-Penning Trap.* PhD thesis, University of California at San Diego, 1993.

[61] D. Montgomery, W. H. Matthaeus, W. T. Stribling, D. Martinez, and S. Oughton. Relaxation in two dimensions and the "sinh-Poisson" equation. *Phys. Fluids A*, 4:3, 1992.

[62] D. Montgomery and L. Phillips. MHD turbulence – relaxation processes and variational-principles. *Physica D*, 37:215, 1989.

[63] J. D. Moody, 1993. private communication.

[64] J. D. Moody and J. H. Malmberg. Free expansion of a pure electron plasma column. *Phys. Rev. Lett.*, 69:3639, 1992.

[65] D. W. Moore and P. G. Saffman. Structure of a line vortex in an imposed strain. In J. H. Olsen, A. Goldberg, and M. Rogers, editors, *Aircraft Wake Turbulence*, page 339. Plenum, 1971.

[66] M. Nelkin. In what sense is turbulence an unsolved problem. *Science*, 255:566, 1992.

[67] J. Notte, A. J. Peurrung, J. Fajans, R. Chu, and J. S. Wurtele. Asymmetric stable equilibria of non-neutral plasmas. *Phys. Rev. Lett.*, 69:3056, 1992.

[68] T. M. O'Neil. A confinement theorem for nonneutral plasmas. *Phys. Fluids*, 23:2216, 1980.

[69] T. M. O'Neil. Plasmas with a single sign of charge. In C. W. Roberson and C. F. Driscoll, editors, *Non-Neutral Plasma Physics*, page 1. American Institute of Physics, 1988.

[70] L. Onsager. Statistical hydrodynamics. *Nuovo Cimento Suppl.*, 6:279, 1949.

[71] R. L. Panton. *Incompressible Flows.* John Wiley and Sons, 1984.

[72] J. Pedlosky. *Geophysical Fluid Dynamics.* Springer-Verlag, 1987.

[73] A. J. Peurrung. *Measurements of a Magnetized Pure Electron Plasma.* PhD thesis, University of California at Berkeley, 1992.

[74] A. J. Peurrung and J. Fajans. A limitation to the analogy between pure electron plasmas 2D inviscid fluids, 1993. Submitted to *Phys. Rev. Lett.*

[75] S. A. Prasad and T. M. O'Neil. Finite length thermal equilibria of a pure electron plasma column. *Phys. Fluids*, 22:278, 1979.

[76] P. B. Rhines and W. R. Young. How rapidly is a passive scalar mixed within closed streamlines. *J. Fluid Mech.*, 133:133, 1983.

[77] C. W. Roberson and C. F. Driscoll, editors. *Non-Neutral Plasma Physics.* American Institute of Physics, 1988. See pages 1-111 for a better review of theories and experiments on non-neutral plasmas.

[78] R. Robert and J. Sommeria. Statistical equilibrium states for two-dimensional flows. *J. Fluid Mech.*, 229:291, 1991.

[79] R. Robert and J. Sommeria. Relaxation towards a statistical equilibrium state in two-dimensional perfect fluid dynamics. *Phys. Rev. Lett.*, 69:2776, 1992.

[80] G. B. Rosenthal. *Experimental Studies on an Annular Nonneutral Electron Plasma.* PhD thesis, University of California at Los Angeles, 1991.

[81] A. Roshko. Structure of turbulent shear flows: A new look. *AIAA J.*, 14:1349, 1976.

[82] P. G. Saffman. *Vortex Dynamics.* Cambridge University Press, 1992.

[83] P. G. Saffman and R. Szeto. Equilibrium shapes of a pair of equal uniform vortices. *Phys. Fluids*, 23:2339, 1980.

[84] P. Santangelo, R. Benzi, and B. Legras. The generation of vortices in high-resolution, two-dimensional decaying turbulence and the influence of initial conditions on the breaking of self-similarity. *Phys. Fluids A*, 1:1027, 1989.

[85] R. A. Smith. Maximization of vortex entropy as an organizing principle in intermittent, decaying, 2-dimensional turbulence. *Phys. Rev. A*, 43:1126, 1991.

[86] R. A. Smith. Effects of electrostatic confinement fields and finite gyroradius on an instability of hollow electron columns. *Phys. Fluids B*, 4:287, 1992.

[87] R. A. Smith, 1993. private communication.

[88] R. A. Smith and T. M. O'Neil. Nonaxisymmetric thermal equilibria of a cylindrically bounded guiding-center plasma or discrete vortex system. *Phys. Fluids B*, 2:2961, 1990.

[89] R. A. Smith and M. N. Rosenbluth. Algebraic instability of hollow electron columns and cylindrical vortices. *Phys. Rev. Lett.*, 64:649, 1990.

[90] J. Sommeria, S. D. Meyers, and H. L. Swinney. Laboratory simulation of Jupiter's Great Red Spot. *Nature*, 331:689, 1988.

[91] J. Sommeria, C. Staquet, and R. Robert. Final equilibrium state of a two-dimensional shear layer. *J. Fluid Mech.*, 223:661, 1991.

[92] C. M. Surko and R. E. Slusher. Waves and turbulence in a tokamak fusion plasma. *Science*, 221:817, 1983.

[93] P. Tabeling, S. Burkhart, O. Cardoso, and H. Willaime. Experimental study of freely decaying two-dimensional turbulence. *Phys. Rev. Lett.*, 67:3772, 1991.

[94] J. B. Taylor. Relaxation and magnetic reconnection in plasmas. *Rev. Mod. Phys.*, 58:741, 1986.

[95] H. Tennekes and J. L. Lumley. *A First Course in Turbulence.* MIT Press, 1972.

[96] H. F. Webster. Breakup of hollow electron beams. *J. Appl. Phys.*, 26:1386, 1955.

[97] D. J. Wineland, W. M. Itano, J. C. Bergquist, S. L. Gilbert, J. J. Bollinger, and F. Ascarrunz. Liquid and solid ion plasmas. In C. W. Roberson and C. F. Driscoll, editors, *Non-Neutral Plasma Physics*, page 93. American Institute of Physics, 1988.